Award Number: G12AP20081

Ground Motions and Tsunamis from Large Cascadia Subduction Earthquakes Based on the 2011 Tokoku, Japan Earthquake

FINAL REPORT

July 30, 2013

Paul Somerville,* Andreas Skarlatoudis and Wenwen Li

URS Group, Inc.

915 Wilshire Boulevard
Los Angeles, CA 90017

Tel: (213) 996-2200
Fax: (213) 996-2290

*Email: paul.somerville@urs.com

Research supported by the U.S. Geological Survey (USGS), Department of the Interior, under award number G12AP20081. The views and conclusions contained in this document are those of the authors and should not be interpreted as necessarily representing the official policies, either expressed or implied, of the U.S. Government.

Contents

GROUND MOTIONS AND TSUNAMIS FROM LARGE CASCADIA SUBDUCTION EARTHQUAKES BASED ON THE 2011 TOKOKU, JAPAN EARTHQUAKE 3

Summary 3

Earthquake Source Scaling Relations Of Subduction Earthquakes 3

Procedure For Broadband Strong Ground Motion Simulation 4

Ground Motion Models 6

The Mw 9.0 Tohoku, Japan Earthquake Of March 11, 2011 7

Crustal Structure Model 10

Comparison Of Recorded And Simulated Ground Motions - 2011 Tohoku Event 11

Ground Motion Maps of the 2011 Tohoku Earthquake 22

Earthquakes that Rupture the Entire Cascadia Subduction Zone 27

Crustal Structure 30

Ground Motion Attenuation 30

Ground Motion Maps 51

Propagation and Inundation Modeling of the 11 March 2011 Tohoku Tsunami 65

Tsunami Modeling of Mw 9.0 Cascadia Subduction Earthquake Scenarios 72

References 78

GROUND MOTIONS AND TSUNAMIS FROM LARGE CASCADIA SUBDUCTION EARTHQUAKES BASED ON THE 2011 TOKOKU, JAPAN EARTHQUAKE

Summary

The Mw 9.0 Tohoku-oki earthquake that occurred on March 11 2011 off the Pacific Coast of Japan is the largest known subduction earthquake to have occurred in Japan. The Tohoku earthquake produced a destructive tsunami causing widespread devastation in coastal areas including catastrophic damage at the Fukushima nuclear power plant, and extensive ground failure from liquefaction and slope instability. It is also the largest earthquake to have been well recorded on strong motion instruments.. The strong ground motion properties of this earthquake have been extensively studied by several scientists (Stewart et al., 2013, Skarlatoudis and Papazachos 2012 among others) revealing unique features of the rupture properties as well as of the propagation path and local site conditions.

It is important to gain insight into the nature of the ground motions and tsunami from this earthquake and use this knowledge to improve models of strong ground motion in western Oregon and Washington, particularly including the effects of long duration codas and long periods expected from plate-boundary earthquakes in Cascadia.

In this report, we first test our capability to simulate 44 broadband strong motion recordings of the Mw 9.0 Tohoku-oki earthquake by demonstrating that our simulations reproduce the amplitudes of the recorded ground motions without systematic bias. We use simulations to study the attenuation properties of the ground motions caused by the earthquake, and we simulate the strong ground motions and tsunami to validate our simulation procedures against the recordings.

Based on this test using the Mw 9.0 Tohoku-oki earthquake, we then applied the ground motion and tsunami simulation procedures to estimate the ground motion and tsunami characteristics of earthquakes that rupture the entire Cascadia subduction zone. We produced several different slip models and selected ones that could produce extreme and moderate ground motions and tsunami inundation in order to study their variability and sensitivity to the individual characteristics of the slip model. We compare the simulated ground motions with those predicted by other models, and make maps of the simulated ground motions for two site conditions, soft rock and deep soil. We provide equations for predicting the response spectra of the ground motions for these two site conditions.

Earthquake Source Scaling Relations Of Subduction Earthquakes

Somerville et al. (2002) developed scaling relations for the source parameters of subduction earthquakes, based on the rupture models of seven large subduction earthquakes. These models are analogous to those we developed for crustal earthquakes (Somerville et al., 1999). The subduction earthquakes used in these scaling relations include three earthquakes whose rupture models we

developed: 1923 Tokyo, Japan (Wald and Somerville, 1995); 1944 Tonankai, Japan (Ichinose et al., 2003); and 2001 Peru (Somerville et al., 2003). The rupture models portray the spatial and temporal distribution of slip on the fault plane, as inferred from strong motion recordings, teleseismic data, and in some cases geodetic and tsunami observations. The scaling relations describe the scaling with seismic moment of rupture area, rise time, asperity dimensions, and the corner periods of spatial wavenumber models of fault slip heterogeneity, which control the spatial distribution of slip and slip velocity.

We used the Somerville et al. (2002) scaling relations to characterize the spatial and temporal distribution of slip on the rupture plane of future large subduction earthquakes. The relation between seismic moment and rupture area for subduction earthquakes was found to be:

$$A = 5.2 \times 10^{-15} M_o^{2/3}$$

For a given seismic moment, the subduction earthquake rupture area is more than twice as large as that found for crustal earthquakes by Somerville et al. (1999):

$$A = 2.23 \times 10^{-15} M_o^{2/3}$$

Consequently, for a given seismic moment, subduction earthquakes have average slip that is less than half that of crustal earthquakes. Somerville et al. (2002) also measured the rise time of both subduction and crustal earthquakes based on the maximum slip velocity (Ishii et al., 2002). They found that the rise time for both subduction and crustal earthquakes is given by:

$$T_r = 1.8 \times 10^{-9} M_o^{1/3}$$

Since the slip in subduction earthquakes is less than half that in crustal earthquakes of the same seismic moment, a similar rise time implies that the slip velocity on the fault in subduction earthquakes is less than half that in crustal earthquakes. This causes the ground motions of subduction earthquakes to be weaker than those of crustal earthquakes having the same seismic moment.

Procedure For Broadband Strong Ground Motion Simulation

We use a hybrid broadband ground motion simulation approach, based on frequency-wavenumber Green's functions for long periods (> 3s) and on a partly stochastic ray theory method (Somerville et al., 1991) for shorter periods, to simulate broadband ground motions for large subduction earthquakes. We showed in earlier work that the short period simulation procedure successfully reproduces the recorded ground motions of the Mw 8.0 Valparaiso, Chile and Michoacan, Mexico earthquakes of 1985 (Somerville et al., 1991), the Mw 8.4 Arequipa, Peru of 2001 earthquake (Somerville et al., 2008) as well as of the Mw 8.8 Maule, Chile of 2010 earthquake (Somerville et al, 2013), and on that basis we applied it to simulate the ground motions of Mw 8.0 Cascadia earthquakes (Cohee et al., 1991). Specifically, we used the Caleta de Campos rock site recording of an aftershock of the 1985 Michoacan, Mexico earthquake as an empirical source function in the simulations, described in detail by Cohee et al. (1991).

In the hybrid broadband simulation procedure, the low frequency and high frequency components of the ground motions are computed separately and then combined using matched filters. The low frequency simulation methodology, used for periods longer than 0.3s, uses a deterministic representation of source and wave propagation effects (Graves and Pitarka, 2004) that is based on the approach described by Hartzell and Heaton (1983). The basic calculation is carried out using a 1D frequency-wavenumber integration algorithm.

The earthquake source is specified by a kinematic description of fault rupture, incorporating spatial heterogeneity in slip, rupture velocity and rise time. Following Hartzell and Heaton (1983), the fault is divided into a number of subfaults. The slip and rise time are constant across each individual subfault, although these parameters are allowed to vary from subfault to subfault. We use a slip velocity function that is constructed using two triangles as shown in Figure 1.

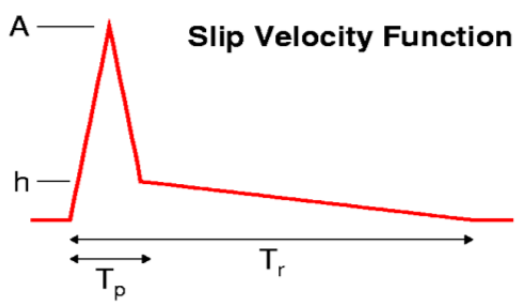

Figure 1. Slip velocity function used in the deterministic simulations [see equation (1)].

This functional form is based on results of dynamic rupture simulations (e.g., Guatteri et al., 2003). We constrain the parameters of this function as follows:

$$T_r = 1.83x10^{-9} \cdot M_0^{-1/3}$$
$$T_p = 0.2 \cdot T_r \qquad (1)$$
$$h = 0.2 \cdot A$$

where M_0 is the seismic moment, T_r is the rise time and A is normalized to give the desired final slip. The expression for T_r comes from the empirical analysis of Somerville et al. (1999). In general, T_r may vary across the fault; however, in practice we only allow a depth dependent scaling such that T_r increases by a factor of 2 if the rupture is between 0 and 5 km depth. This is consistent with observations of low slip velocity on shallow fault ruptures (Kagawa et al., 2004). The rupture initiation time (T_i) is determined using the expression:

$$T_i = \frac{R}{V_r} - \delta t$$
$$V_r = 0.8 \cdot V_s \qquad (2)$$

where R is the rupture path length from the hypocenter to a given point on the fault surface, V_r is the rupture velocity and is set at 80% of the local shear wave velocity (V_s), and δt is a timing perturbation that scales linearly with slip amplitude such that $\delta t = \delta t_0$ where the slip is at its maximum and δt=0 where the slip is at the average slip value. For these calculations, we set δt=0.1s. This scaling results in

faster rupture across portions of the fault having large slip as suggested by source inversions of past earthquakes (Hisada, 2001).

For scenario earthquakes, the slip distribution can be specified using randomized spatial fields, constrained to fit certain wave number properties (e.g., Somerville et al., 1999; Mai and Beroza, 2002). In the simulation of past earthquakes, we use smooth representations of the static slip distribution determined from finite-fault source inversions. Typically, these inversions will also include detailed information on the spatial variation of rupture initiation time and slip velocity function, either by solving for these parameters directly or by using multiple time windows. However, we do not include these in our simulations of scenario earthquakes, but rather rely on equations (1) and (2) to provide them. This is because the level of detailed resolution of these parameters provided by the source inversions will generally not be available a priori for future earthquakes. Furthermore, since the inversions determine these parameters by optimally fitting the selected observations, it is not clear that they will produce an optimal waveform fit at sites not used in the inversion.

The high frequency simulation methodology, used for periods shorter than 0.3s, is a stochastic approach that sums the response for each subfault using empirical source functions. The simulation procedure was originally developed by Somerville et al. (1991) following the concepts of Irikura (1978) and Hartzell (1978).

The crustal structure model used in the simulations has a median Vs_{30} (average shear wave velocity for the upper 30m) of 309 m/s and consequently the generated ground motion maps and all comparisons with the available GMPEs are presented for sites with this Vs_{30}. It should be noticed that in figures with comparisons of simulated and observed data we have used the amplification factors proposed by Boore et al. (2013; BSSA13) to scale the response spectra from the observed data to the median Vs_{30}. In all other cases the BSSA13 amplification factors were applied in the response spectra computed from the simulations.

Ground Motion Models

We compare the ground motion estimates obtained in this report with three ground motion models for subduction earthquakes. Those three models are Atkinson and Boore (2003), Zhao et al. (2006) and Abrahamson et al. (2012). The Atkinson and Boore (2003) and Abrahamson et al. (2012) were derived from a worldwide set of strong motion recordings of subduction earthquakes and the Zhao et al. (2006) model was derived from strong motion recordings from earthquakes in Japan. We compare our results for sites with Vs_{30} = 309 m/s with the relations of Atkinson and Boore (2003) and Abrahamson et al. (2012) derived for the specific Vs_{30} and with the SC II relations of Zhao et al. (2006). In this report, we also fit a simple ground motion model to the simulations. The ground motion model has the form:

$$\ln(Sa) = C_1 + C_2 \times R_{cld}$$

where C_1 and C_2 are the regression coefficients and R_{cld} is the closest distance from the rupture.

The Mw 9.0 Tohoku, Japan Earthquake Of March 11, 2011

The main purpose of this section is to examine whether the simulation procedures for ground motion and tsunami wavefields are able to reproduce the basic characteristics and features of this earthquake. The earthquake and fault parameters from the 2011 Tohoku earthquake, as published by USGS, are listed in Table 1.

Table 1. Earthquake information and fault model adopted for the Tohoku earthquake.

Earthquake Parameters / Fault Model	
Origin Time	05:46:24 UTC
Location	38.297^o N, 142.372^o W
Depth	30 km
Mw	9.0
Strike, dip	193, 10

Several rupture models have been proposed for this earthquake, estimated using strong motion data (Kurahashi and Irikura, 2011), tsunami data (Fujii et al., 2011; Hayashi et al., 2011; Satake et al. 2012), geodetic data (Yue and Lay, 2011) and combinations of all the previous (Koketsu et al., 2011; Yoshida et al., 2011;Yokota et al., 2011). In the present study we selected to use the rupture model that Kurahashi and Irikura (2011) estimated which contains five strong motion generating areas (SMGAs) with different sizes superimposed upon the larger rupture area of the earthquake, shown in Figures 2 and 3. The characteristics as well as the location of each SMGA are listed in Table 2. The total rupture area of the earthquake was about 480 km along strike and 150 km down dip, significantly smaller than previous Mw ~ 9 megathrust earthquakes, which resulted in a high stress drop of 4.8 MPa (Koketsu et al., 2011).

Table 2. Source parameters of SMGAs (source: Kurahashi and Irikura, 2011).

	L (km)	W (km)	M_0 (Nm)	Stress Drop (MPa)	Delay time from origin time (s)
SMGA 1	62.40	41.60	2.31E+21	41.3	15.64
SMGA 2	41.60	41.60	7.05E+20	23.6	66.42
SMGA 3	93.60	52.00	4.34E+21	29.5	68.41
SMGA 4	38.50	38.50	3.83E+20	16.4	109.71
SMGA 5	33.60	33.60	3.99E+20	26.0	118.17

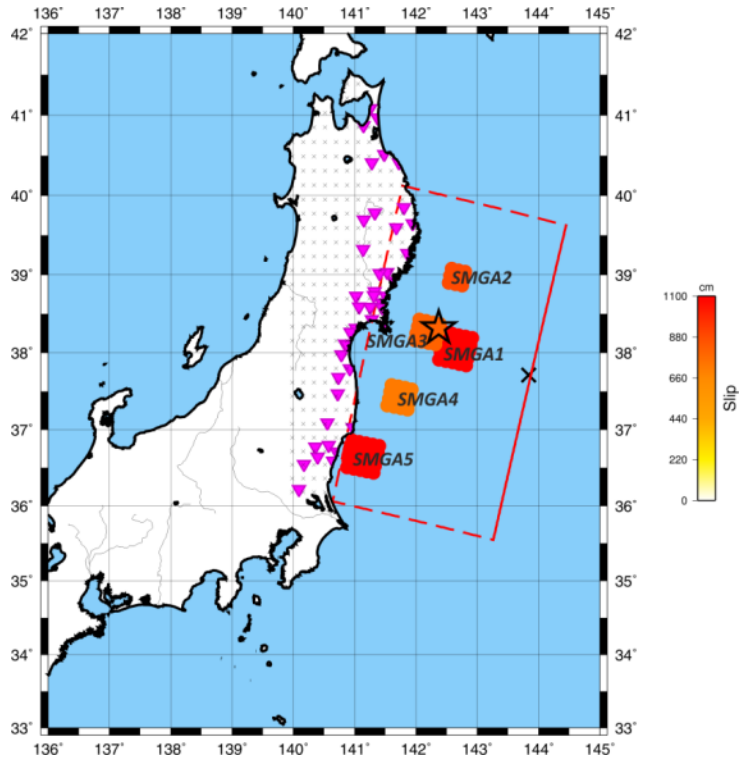

Figure 2. Selected rupture model of the 2011 Tohoku, Japan earthquake, locations of strong ground motion recording stations, and grid of stations used for simulations.

Figure 3 shows the final rupture model used for broadband simulations. The original rupture model from Kurahashi and Irikura (2011) was modified to take account of rupture times using the dependency of rupture velocity on slip described in the preceding section. The average slip in the final model was about 72 cm, while the maximum slip was 1108 cm.

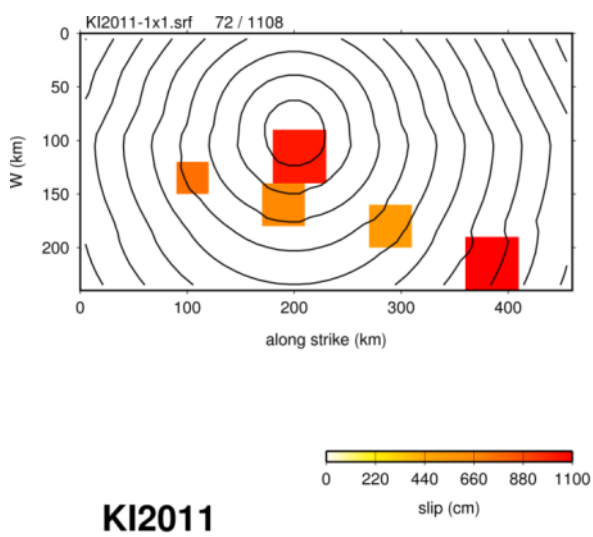

Figure 3. Rupture model of the 2011 Tohoku, Japan earthquake.

The Tohoku earthquake produced a very large number (approximately 2000) of high-quality strong motion recordings from a very dense network of accelerometers (K-net, Kik-net). In order to validate the results of our simulation technique we obtained the strong ground motion recordings from forty four stations, whose locations are shown in Figure 2 and listed, together with the site Vs_{30} in Table 3. The first twelve stations are part of the Kik-net and are installed in boreholes. The specific stations are included in the following comparisons because they were used in deriving the Kurahashi and Irikura (2011) rupture model. All the information listed in Table 3 is available from the National research Institute for Earth science and Disaster prevention of Japan (NIED, http://www.kyoshin.bosai.go.jp).

Table 3. Selected strong motion recordings of the 2011 Tohoku earthquake.

Station Name	Latitude	Longitude	Vs_{30} (m/s)
IWTH14	39.7435	141.9087	816.0
IWTH27	39.0307	141.532	670.0
MYGH03	38.9207	141.6377	934.0
MYGH04	38.786	141.3254	850.0
MYGH06	38.5907	141.071	593.0
MYGH08	38.1133	140.8441	203.0
MYGH12	38.6416	141.4428	748.0
FKSH14	37.0264	140.9702	251.0
FKSH19	37.4703	140.7227	338.0
IBRH13	36.7955	140.575	335.0
IBRH16	36.6405	140.3976	626.0
IBRH19	36.2137	140.0893	692.0
AOM008	41.0840	141.2552	366.2
AOM009	40.9665	141.3733	376.9
AOM010	40.8721	141.1416	240.1
AOM012	40.5138	141.4805	219.9
AOM013	40.4124	141.2800	310.8
FKS001	37.7949	140.9196	296.9
FKS004	37.6799	140.7346	292.0
FKS013	37.0900	140.5563	251.9
IBR001	36.7761	140.3569	208.4
IBR002	36.7061	140.7068	344.8
IBR003	36.5915	140.6453	292.2
IWT001	40.4099	141.7191	239.4
IWT005	39.6472	141.9464	407.5
IWT007	39.2701	141.8561	358.0
IWT009	39.0187	141.4031	579.6
IWT012	39.3209	141.1378	214.3
IWT016	39.5997	141.6789	439.7

Station Name	Latitude	Longitude	Vs_{30} (m/s)
IWT018	39.6953	141.1478	346.2
IWT019	39.8491	141.8034	305.2
IWT020	39.7841	141.3295	146.2
MYG002	38.7262	141.5109	469.2
MYG003	38.7348	141.3106	475.8
MYG004	38.7292	141.0217	430.0
MYG007	38.5876	141.2510	231.1
MYG008	38.5769	141.4514	245.2
MYG010	38.4282	141.2809	261.8
MYG011	38.3052	141.5044	143.7
MYG012	38.3175	141.0193	452.2
MYG013	38.2663	140.9293	272.5
MYG015	38.1049	140.8699	230.9
MYG017	37.9763	140.7818	134.3
TCG014	36.5450	140.1742	387.2

Crustal Structure Model

The crustal velocity model that we used is based on the 3D velocity model for Japan derived by Koketsu et al. (2008). The 1D models for the various sites studied were extracted from the 3D model and the final model listed in Table 4 is an average of all these models.

Table 4. Crustal structure model for Japan.

Thickness (km)	V_p (m/s)	V_s (m/s)	Density (Kgr/m^3)	Q_p	Q_s
0.002	1.7	0.45	2.00	45.0	22.5
0.004	1.8	0.65	2.10	65.0	32.5
0.006	1.8	0.85	2.10	85.0	42.5
0.008	1.9	0.95	2.10	95.0	47.5
0.01	2.0	1.15	2.20	115.0	57.5
0.07	2.4	1.20	2.20	120.0	60.0
0.10	2.6	1.30	2.40	130.0	65.0
0.16	3.0	1.40	2.45	140.0	70.0
0.10	3.6	2.00	2.55	200.0	100.0
0.44	4.2	2.40	2.60	240.0	120.0
5.90	5.5	3.20	2.65	320.0	160.0
10.20	6.1	3.40	2.75	340.0	170.0
14.63	6.5	3.80	3.00	380.0	190.0
16.00	7.8	4.50	3.30	450.0	225.0

Comparison Of Recorded And Simulated Ground Motions - 2011 Tohoku Event

As described in a preceding section we used the Kurahashi and Irikura (2011) rupture model of the 2011 Tohoku earthquake to simulate broadband ground motions at the forty four strong motion recording sites of Table 2, and at the grid of stations shown in Figure 2. We compared the recorded and simulated ground motions at the recording stations, and analyzed the ground motions simulated over the grid.

In Figure 4, we compare the recorded response spectra of the 2011 Tohoku earthquake with the predictions of Zhao et al. (2006) (Zhao06) and Abrahamson et al. (2012) (AGA12) ground motion models. The comparisons show that both models predict the recorded ground motions from this earthquake reasonably well, although there is a tendency to overpredict them, especially at the longer periods, and therefore can be used for validating the simulated results.

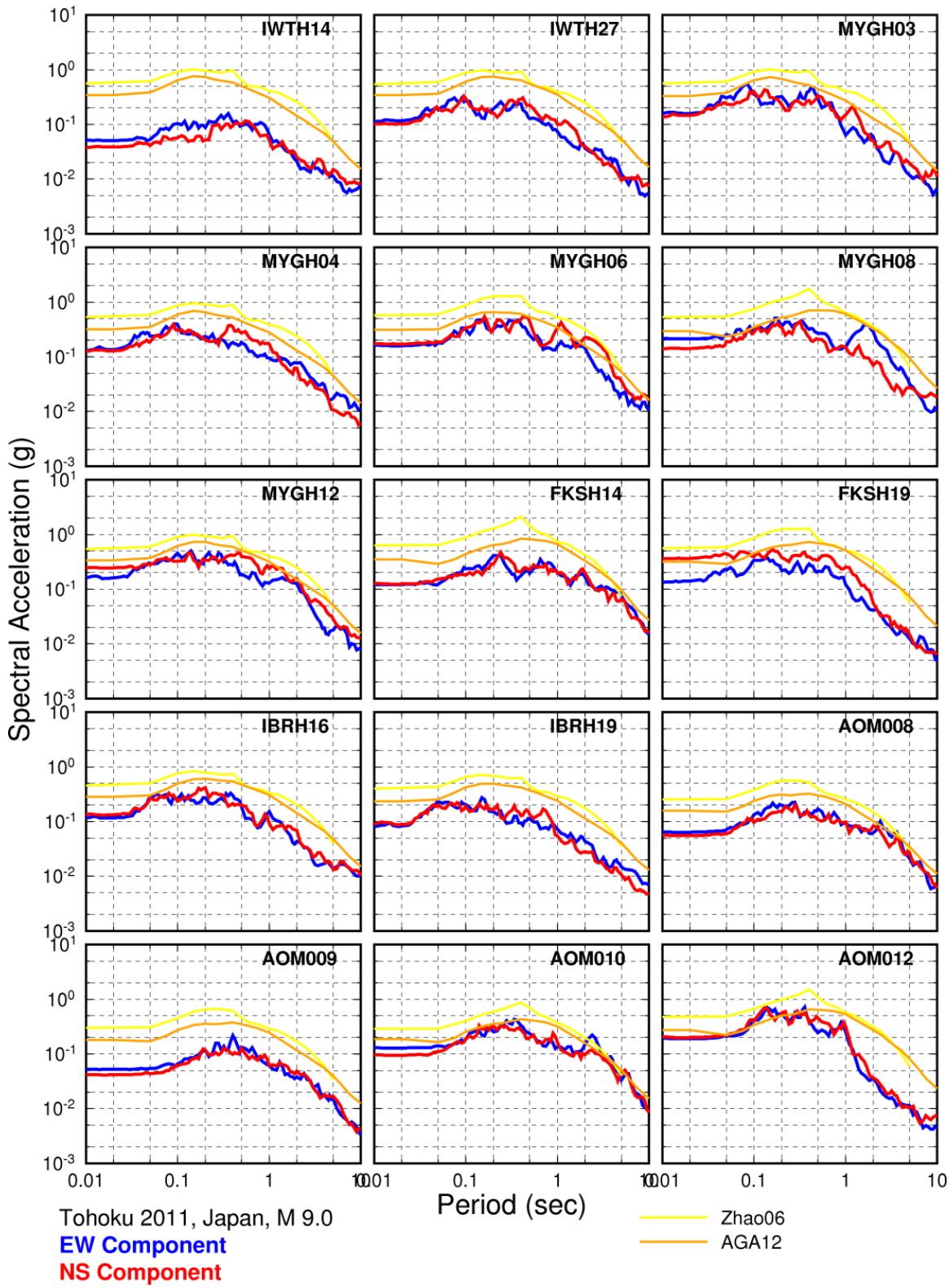

Figure 4. Comparison of the recorded response spectra of the 2010 Maule earthquake with the Zhao et al., 2006 ground motion prediction model.

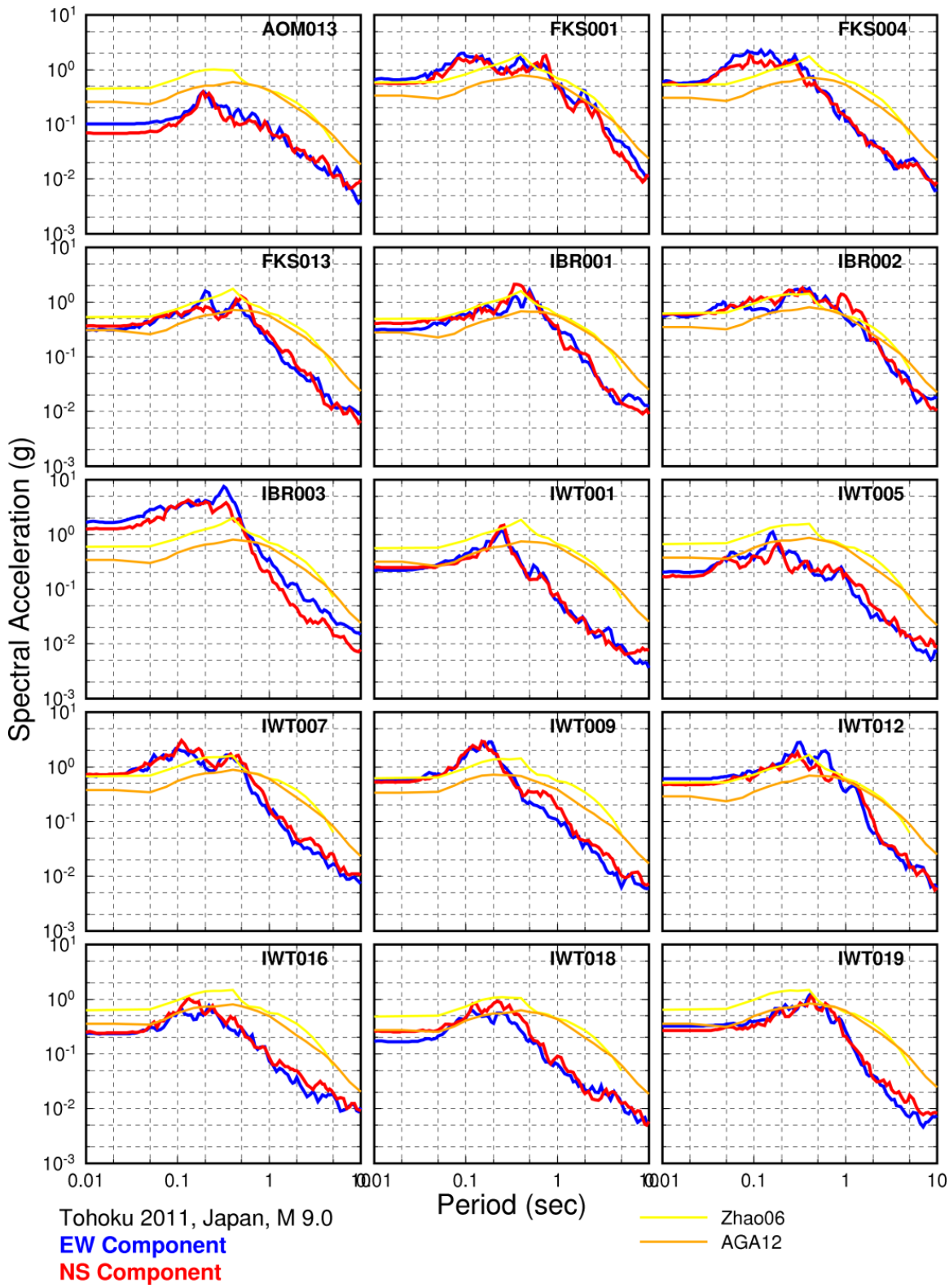

Figure 4. Continued

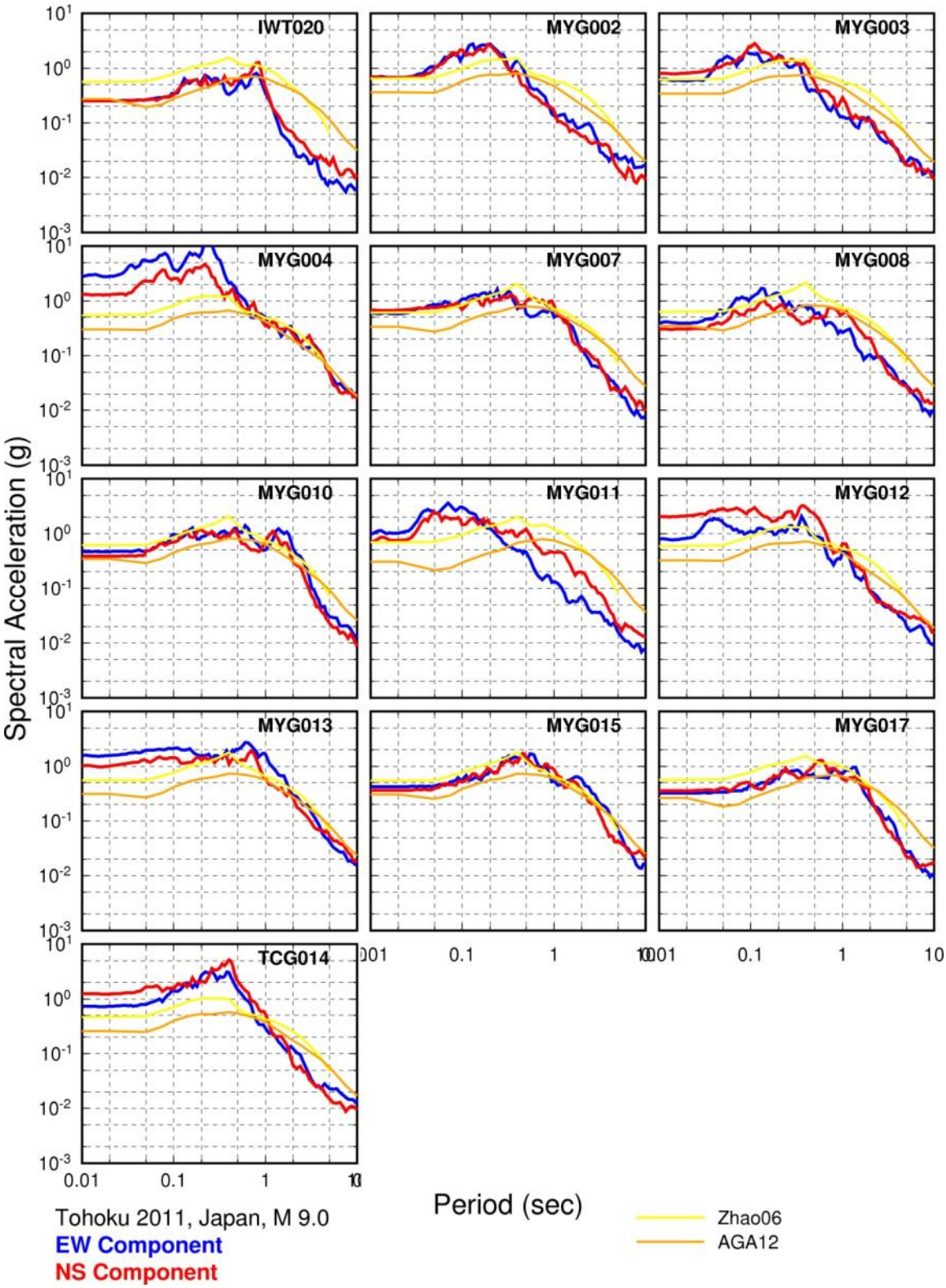

Figure 4. Continued

The comparisons of the simulated values with the empirical models are in close agreement for the majority of the stations studied, including the Kik-net borehole stations, and for the selected period range (0.01-10s). However, both empirical models tend to overestimate ground motions for longer periods for several of the examined stations.

The recorded and simulated response spectra at each station are compared in Figure 5. The response spectra from the recorded stations have been scaled to the median Vs_{30} of the simulations (Vs_{30}=309 m/s) using the BSSA13 amplification factors and are denoted as corrected, hereafter. The comparison shows that the simulations are, in general, in a good agreement with the corrected-data. The largest differences are observed at stations that recorded extreme peak amplitudes e.g. station MYG004, with a PGA at about 2.7g.

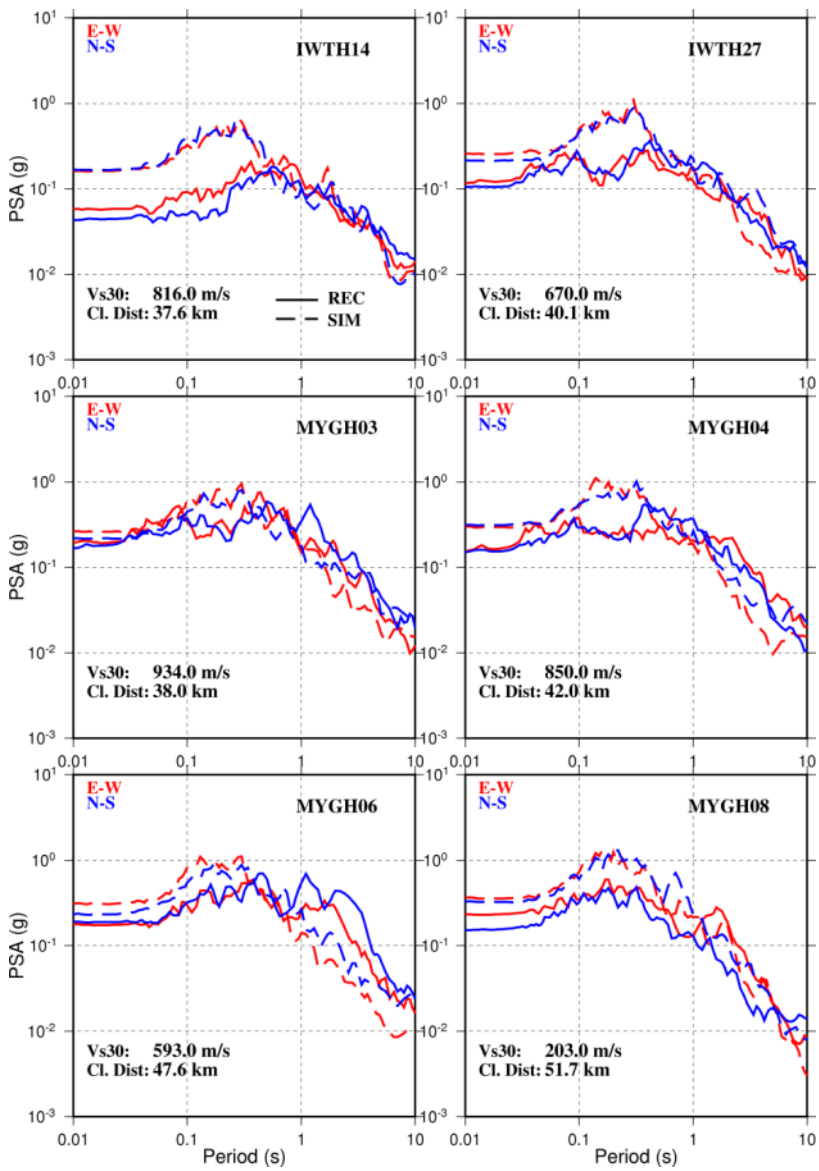

Figure 5. Comparison of the simulated and corrected-recorded response spectra of the 2011 Tohoku earthquake.

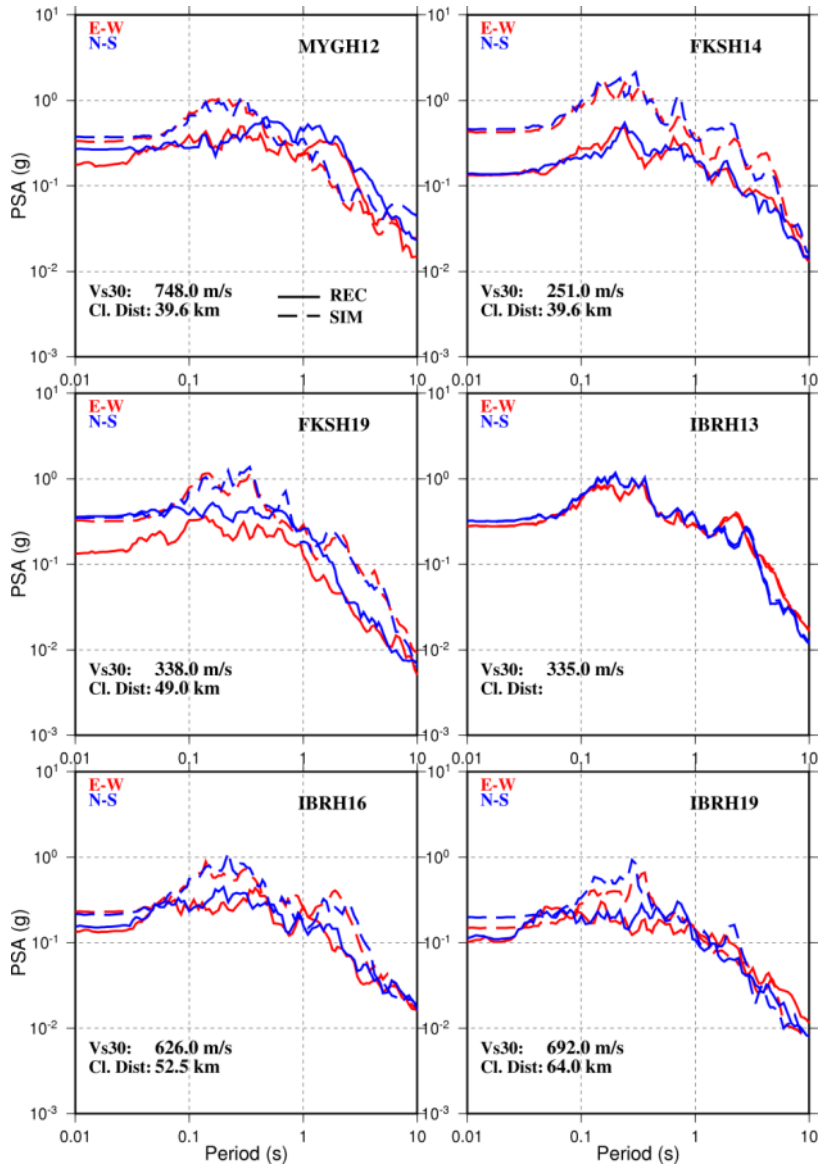

Figure 5. Continued.

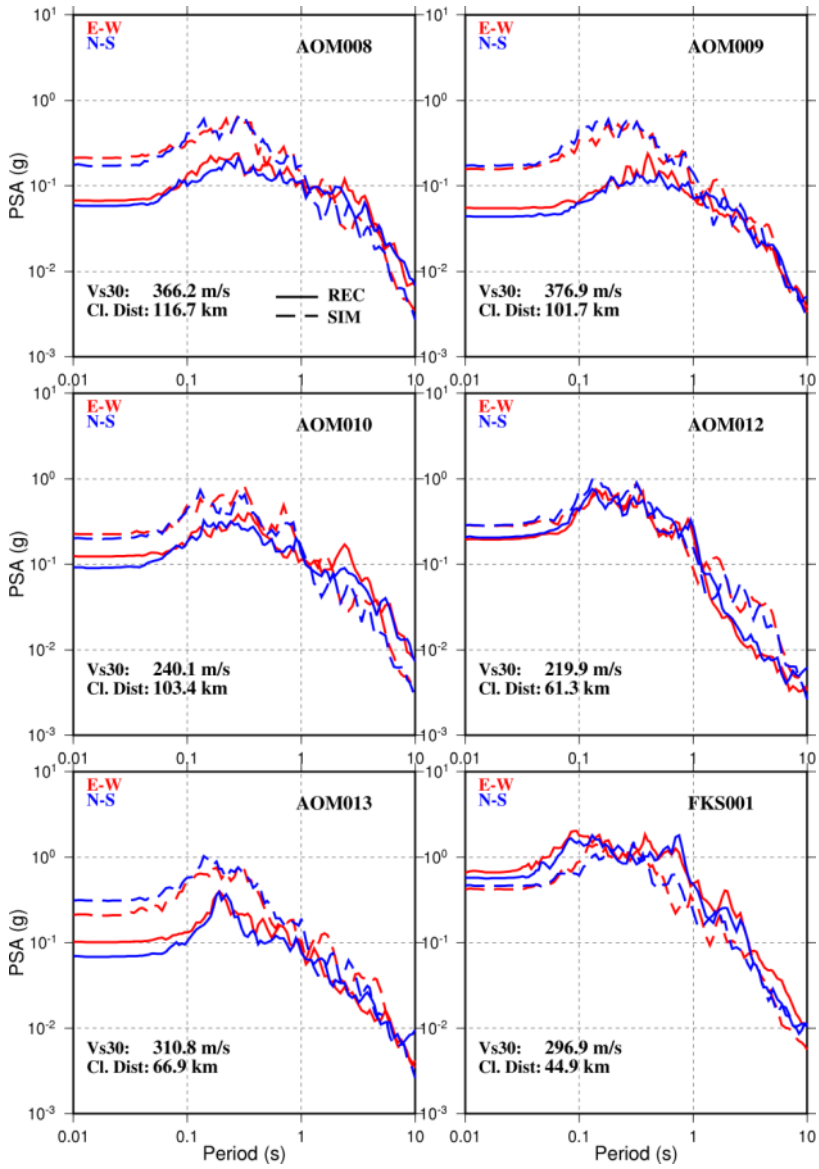

Figure 5. Continued.

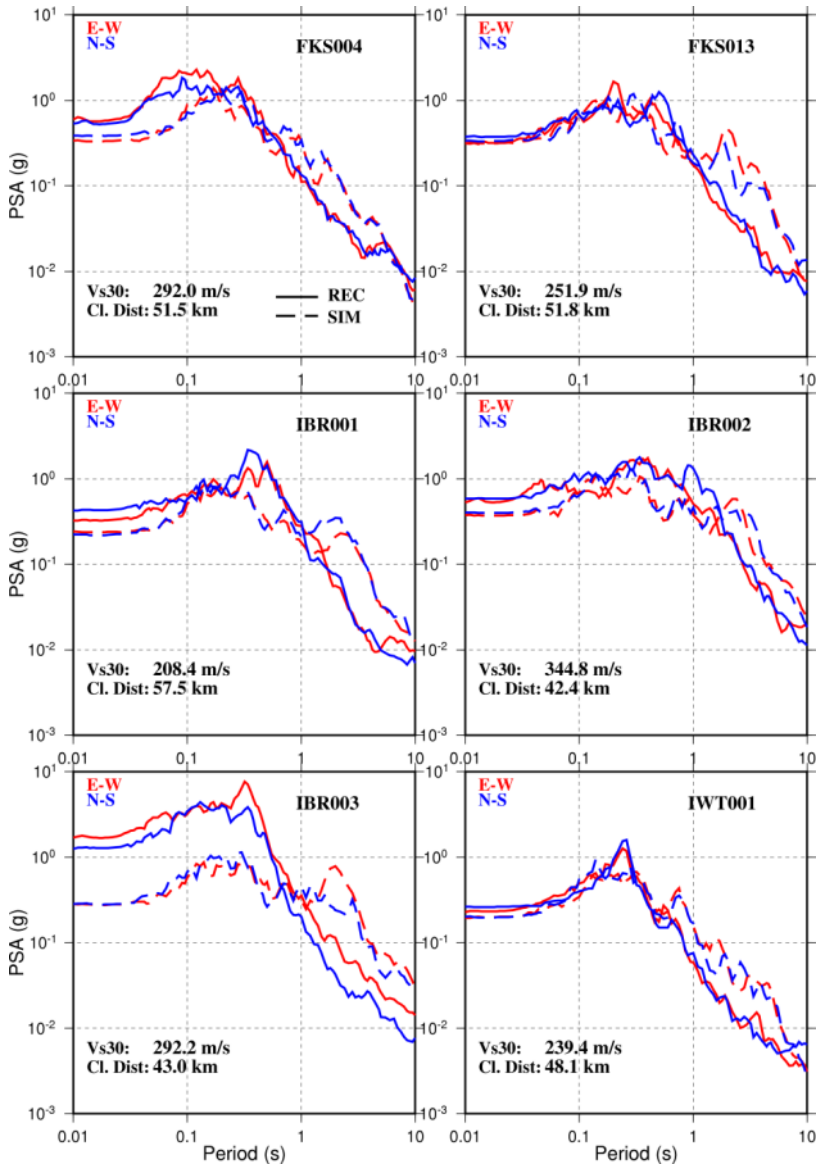

Figure 5. Continued.

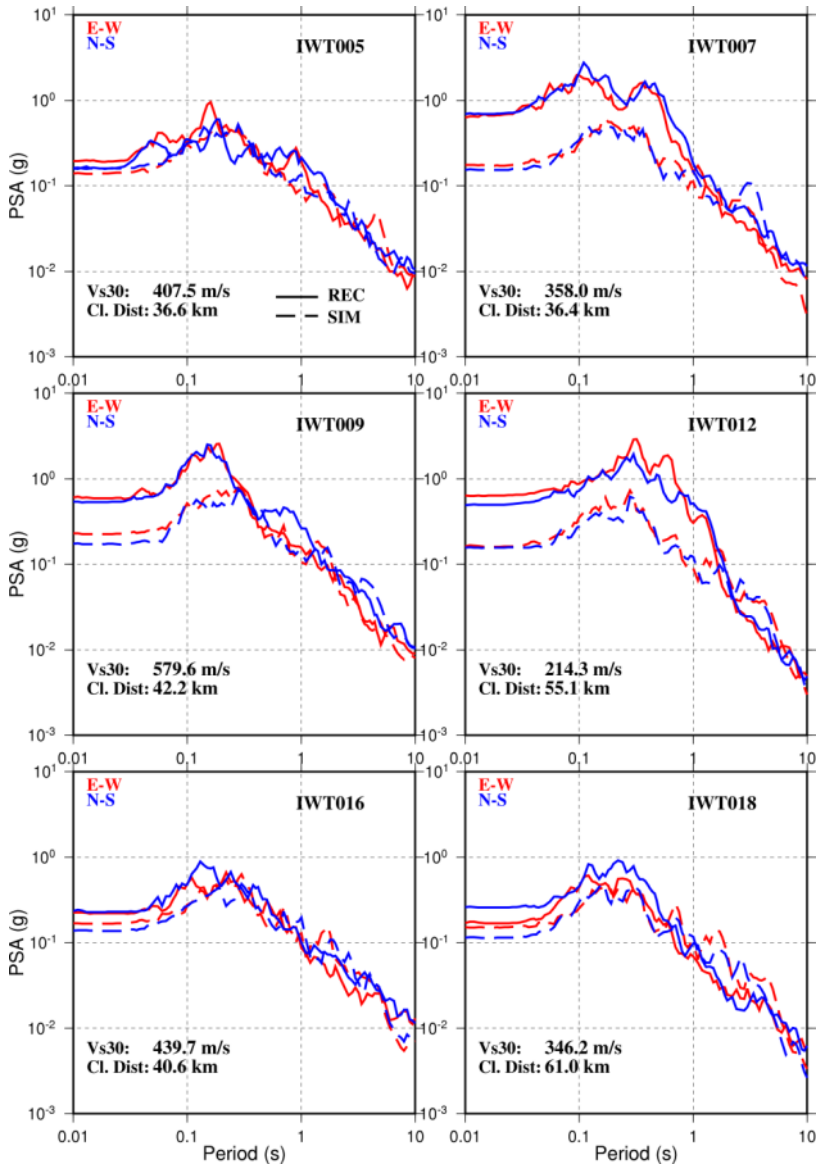

Figure 5. Continued.

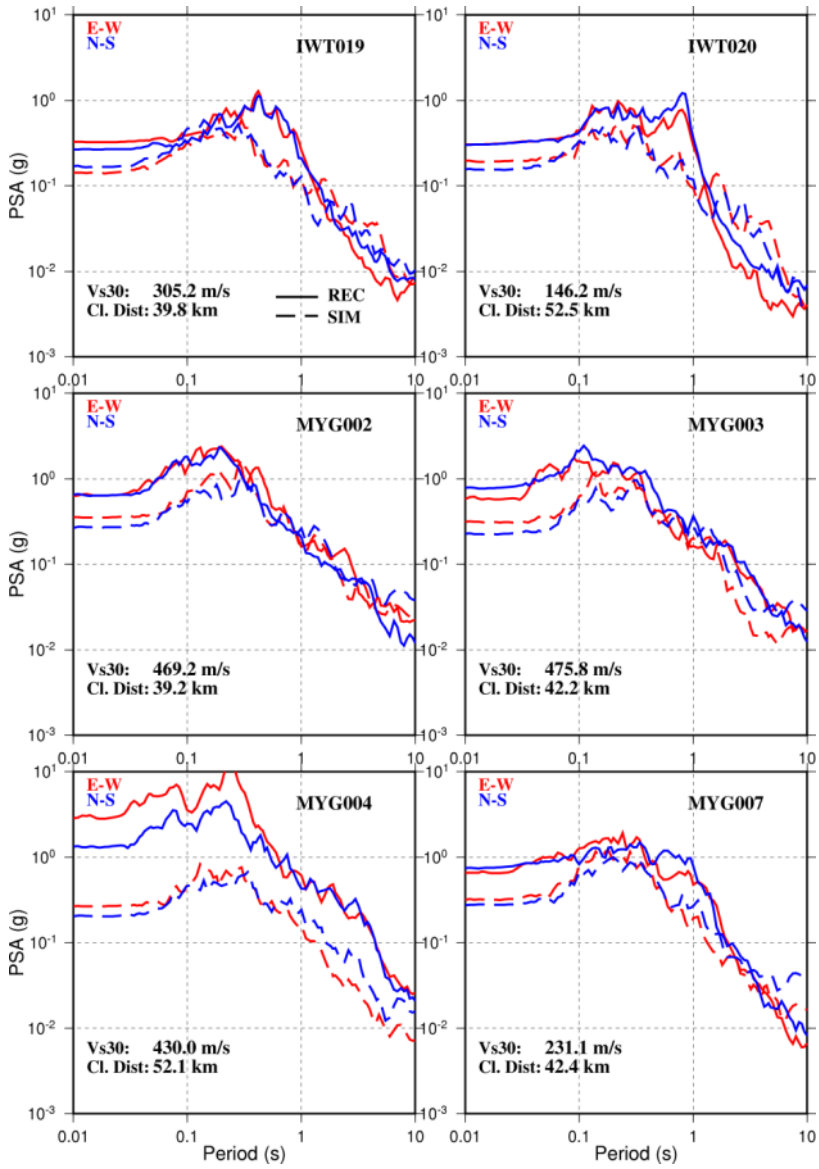

Figure 5. Continued.

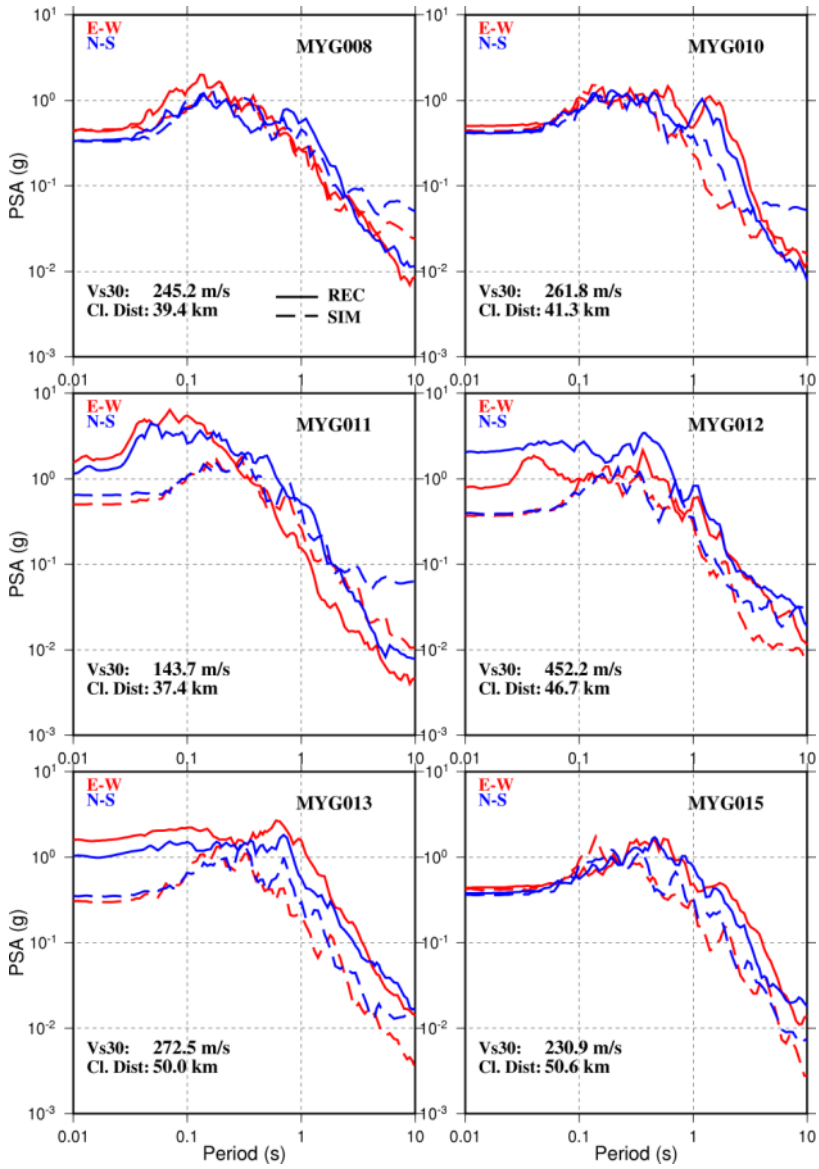

Figure 5. Continued.

Figure 6 shows the response spectral goodness of fit between the corrected-recorded data and simulations at all of the stations, following the procedure of Abrahamson et al. (1990). The grey shading shows the 90th percentile confidence interval in the median prediction. There is little systematic bias in the prediction of the ground motions, although there is some underprediction at a period of 0.5 seconds. The standard deviation of the prediction, shown by the green shading, is about a factor of 1.5 (0.4 natural log units).

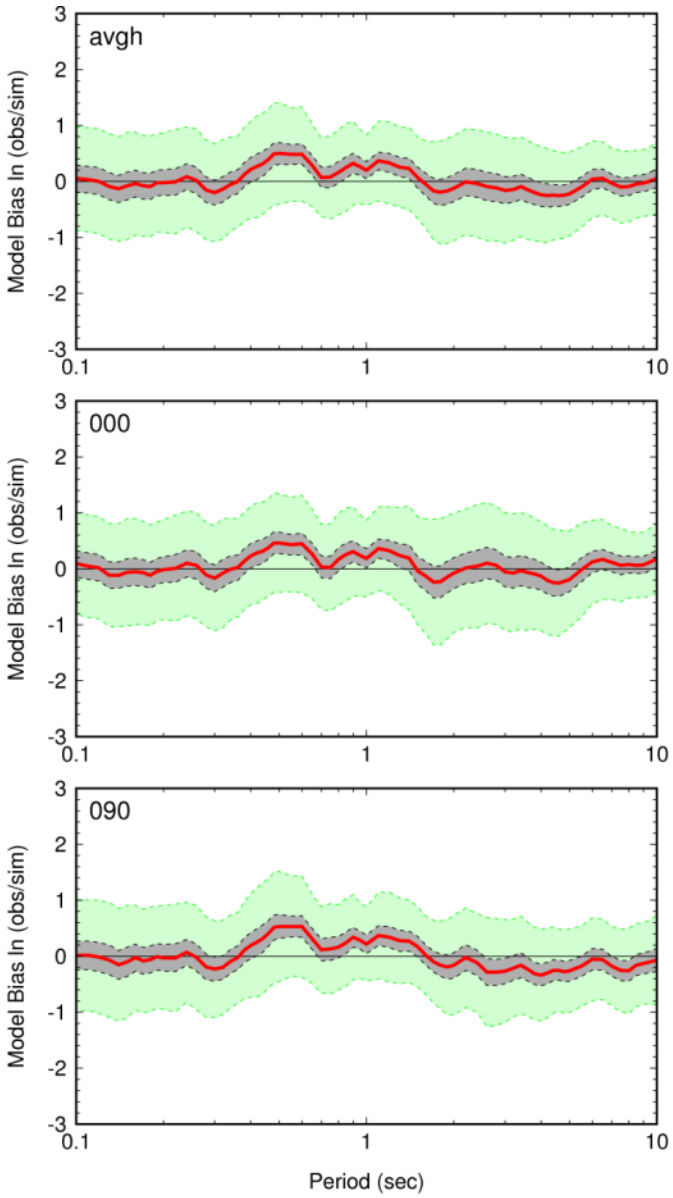

Figure 6. Goodness of fit of corrected-recorded and simulated response spectra of the 2011 Tohoku earthquake for average, North and East components. The red line shows the bias; the green zone shows the standard deviation, and the grey zone shows the 90% confidence interval of the mean.

Ground Motion Maps of the 2011 Tohoku Earthquake

The comparisons described above have demonstrated the performance of our strong motion simulation procedure in matching the recorded ground motions of the Mw 9.0 Tohoku-oki earthquake. This forms the basis for using the simulated ground motions from the grid of stations (shown in Figure 2) in order to examine the strong ground motion attenuation properties in the study area. The attenuation of ground motion is examined in Figures 7 through 11 for peak acceleration and for 0.2s, 0.5s, 1s and 2s

response spectral acceleration periods for the "as simulated" synthetics, i.e. median Vs_{30} of 309 m/s. The agreement between the simulations and ground motion models is quite close for shorter periods. However, at longer periods (2s and 5s) the simulations exhibit lower values than the ones predicted by the empirical models, mostly in closer distances. The closest agreement of the simulations with the different ground motion models is with the Zhao et al. (2006) and Abrahamson et al. (2012) models, while it is in poorer agreement with the Atkinson and Boore (2003) model.

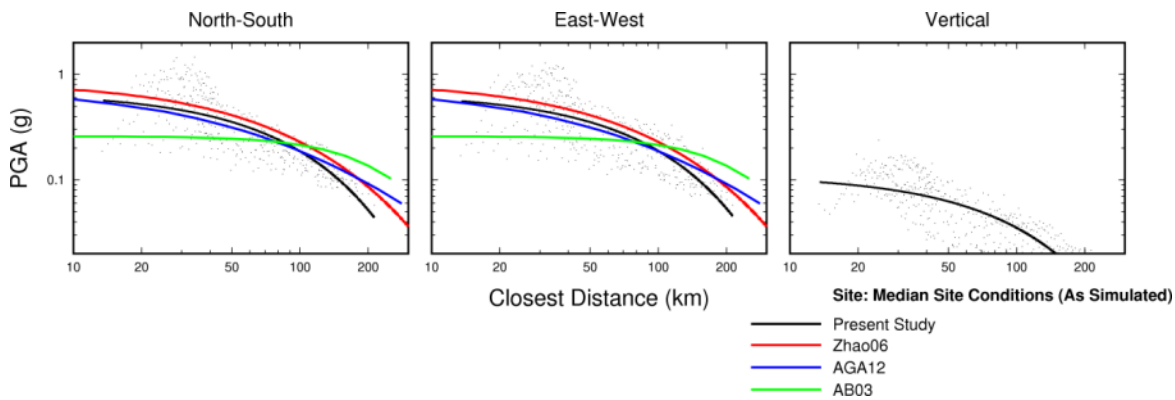

Figure 7. Comparison of simulated peak accelerations with for 2011 Tohoku earthquake with ground motion models.

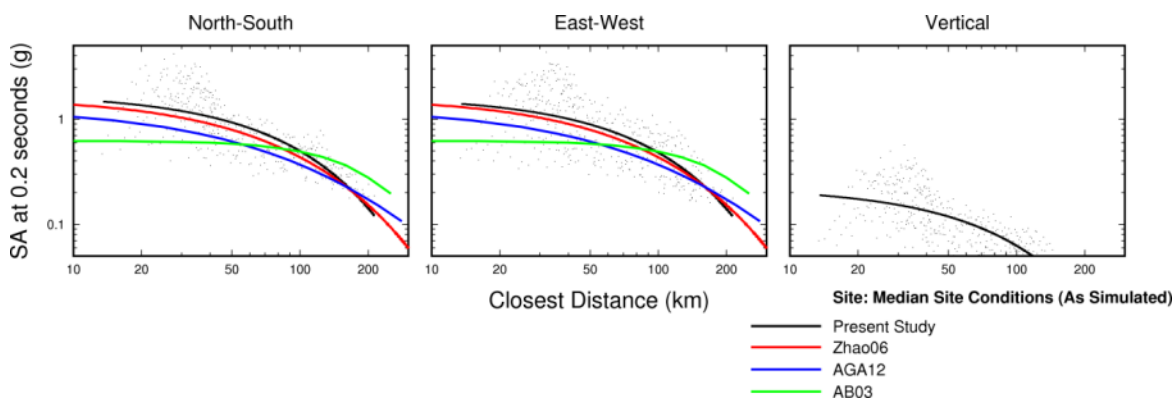

Figure 8. Comparison of simulated 0.2s spectral accelerations for the 2011 Tohoku earthquake with ground motion models.

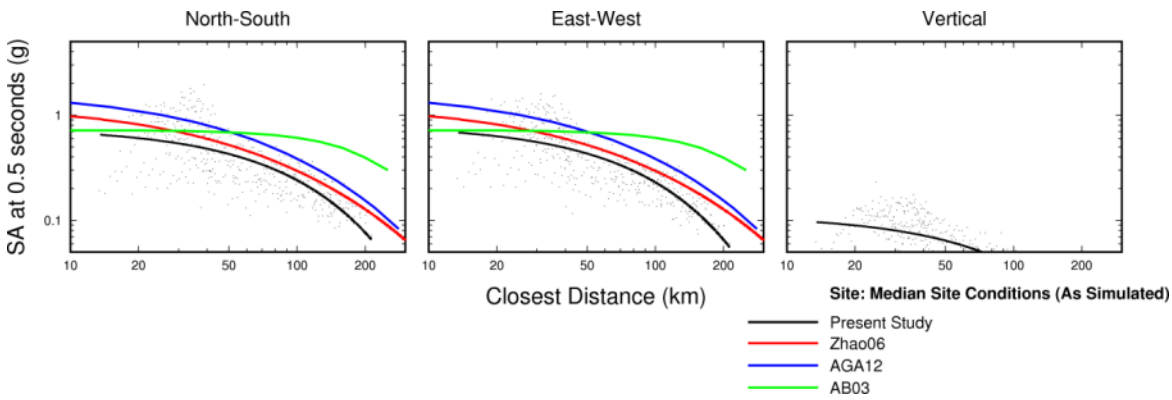

Figure 9. Comparison of simulated 0.5s spectral accelerations for the 2011 Tohoku earthquake with ground motion models.

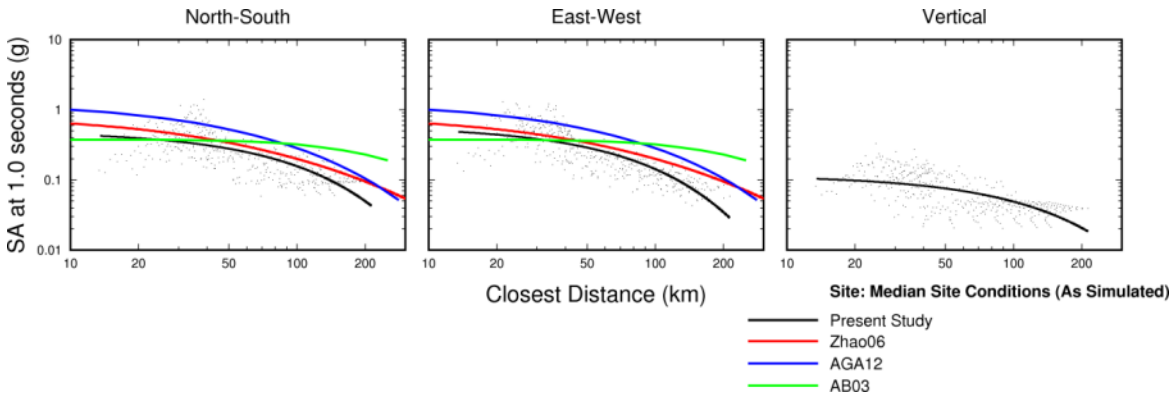

Figure 10. Comparison of simulated 1s spectral accelerations for the 2011 Tohoku earthquake with ground motion models.

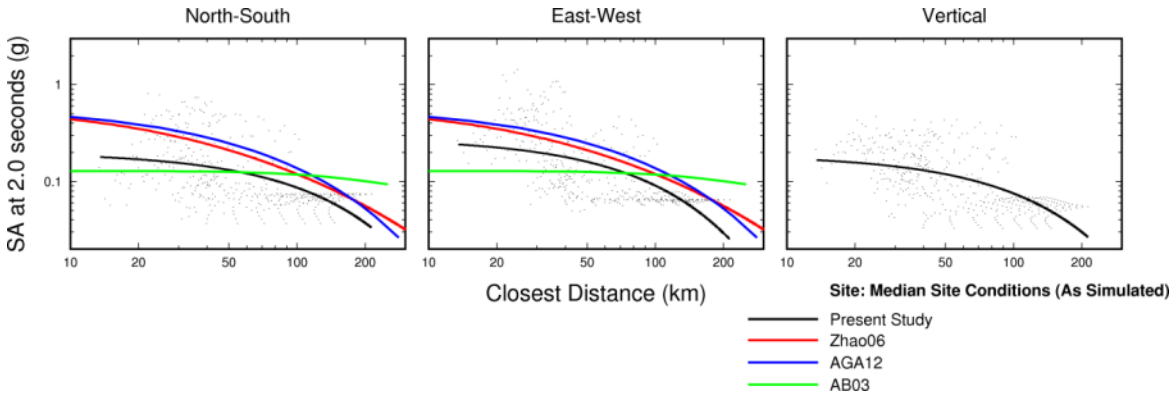

Figure 11. Comparison of simulated 2s spectral accelerations for the 2011 Tohoku earthquake with ground motion models.

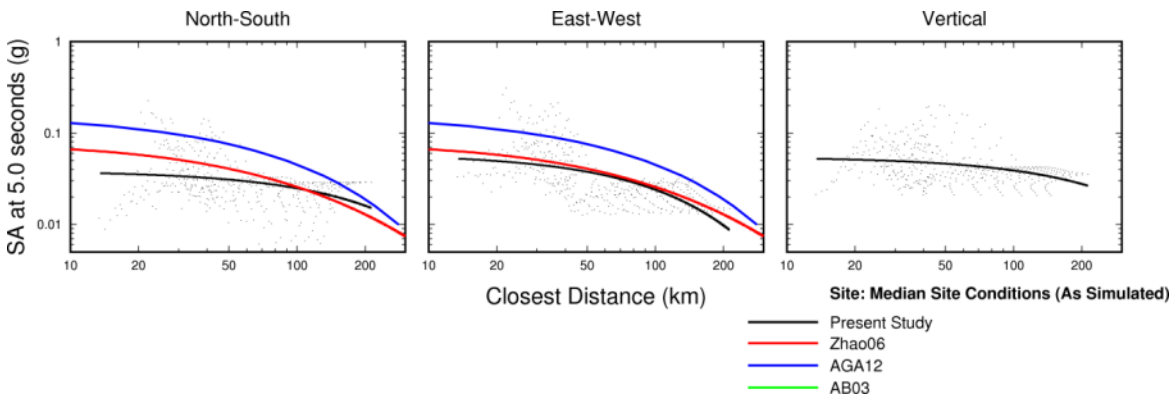

Figure 12. Comparison of simulated 5s spectral accelerations for the 2011 Tohoku earthquake with ground motion models.

The average horizontal response spectra of the simulations of the 2011 Tohoku earthquake are compared with three ground motion models in a suite of distance ranges in Figure 13 for a median Vs_{30} of 309 m/s. There is very good agreement with the Zhao et al. (2006) model for all periods and distance bins studied and good agreement with the other two models used (Abrahamson et al., 2012; Atkinson and Boore, 2003) which seem to estimate lower ground motions for shorter periods at short distances (up to 50 km).

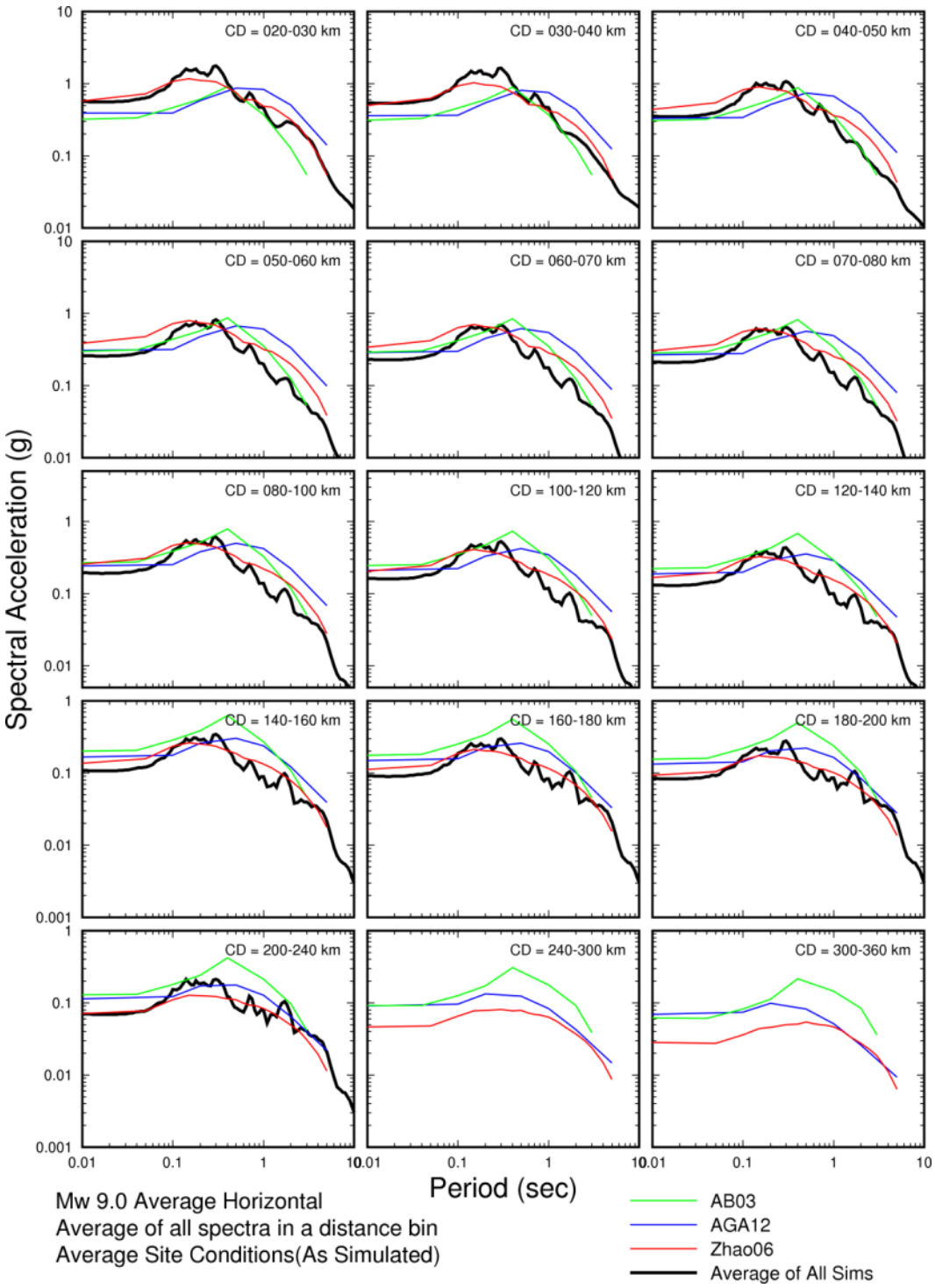

Figure 13. Comparison of average horizontal simulated response spectra for a suite of distance ranges for the 2011 Tohoku earthquake for a median Vs_{30} of 309 m/s with three ground motion models.

Earthquakes that Rupture the Entire Cascadia Subduction Zone

This section of the report describes the modeling of subduction earthquakes that rupture the entire Cascadia subduction zone. The geometry of the Cascadia earthquake source models used in this report was based on the source characterization of Petersen et al. (2008). In particular, we used their "base" model of the bottom of the seismogenic plate interface, shown in Figure 14, to which they gave a weight of 0.5. This model is based on the global observation that rupture usually extends down to depths of about 30 km. Petersen et al (2008) gave weights of 0.1, 0.2 and 0.2 to the alternative models "top," "middle," and "bottom" respectively, which are also shown in Figure 14. The sensitivity of the calculated seismic hazard to uncertainty in the model for the bottom of the seismogenic zone was analyzed by Petersen et al. (2002). This depth controls the eastern extent of the subduction source, and thus has a strong influence on ground motion levels in the urban regions of Washington and Oregon, which mainly lie to the east of the source.

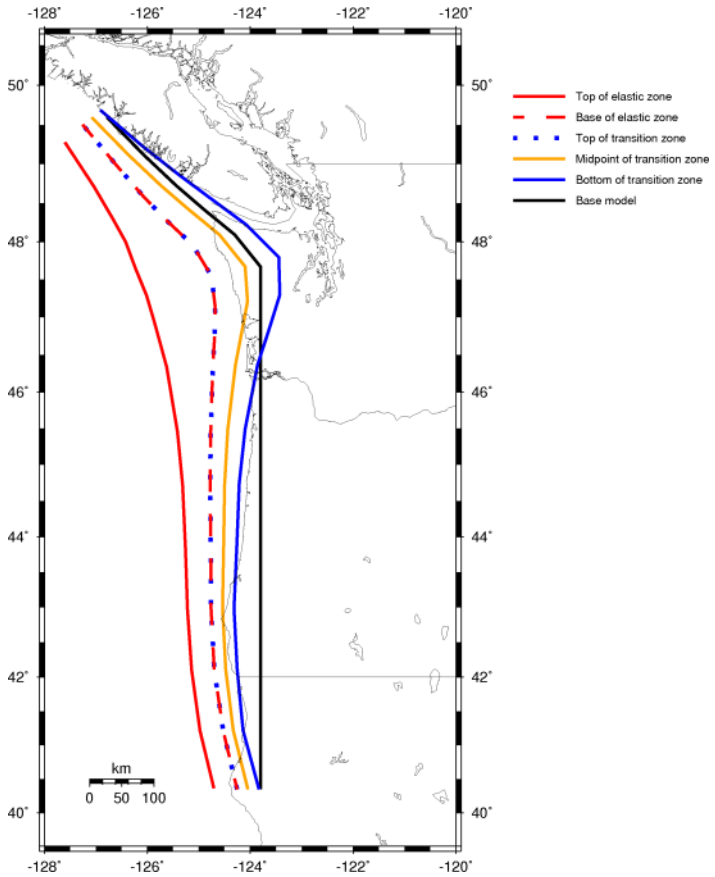

Figure 14. Alternative models of the downdip extent of the Cascadia subduction zone. Source: Petersen et al. (2008). This study used the base model based on global data, shown by the thick black line.

The fault geometry used to represent the base model is shown in Figure 15. The subduction interface was divided into three segments to accommodate the shallower dip at the bend in the subduction zone near the Olympic Peninsula. The shallower segment has a downdip width of 160 km

while the other segments have downdip widths of 120 km. The rupture area of the combined fault segments is 131,500 square km.

Petersen et al. (2008) assume that such earthquakes have magnitudes in the range of 8.8 to 9.2, with a weight of 0.6 given to magnitude 9.0, and weights of 0.2 given to magnitudes of 8.8 and 9.2. Based on the recent megathrust earthquakes that occurred worldwide, this assumption seems to be validated and accordingly, we perform simulations for an earthquake of magnitude Mw 9.0.

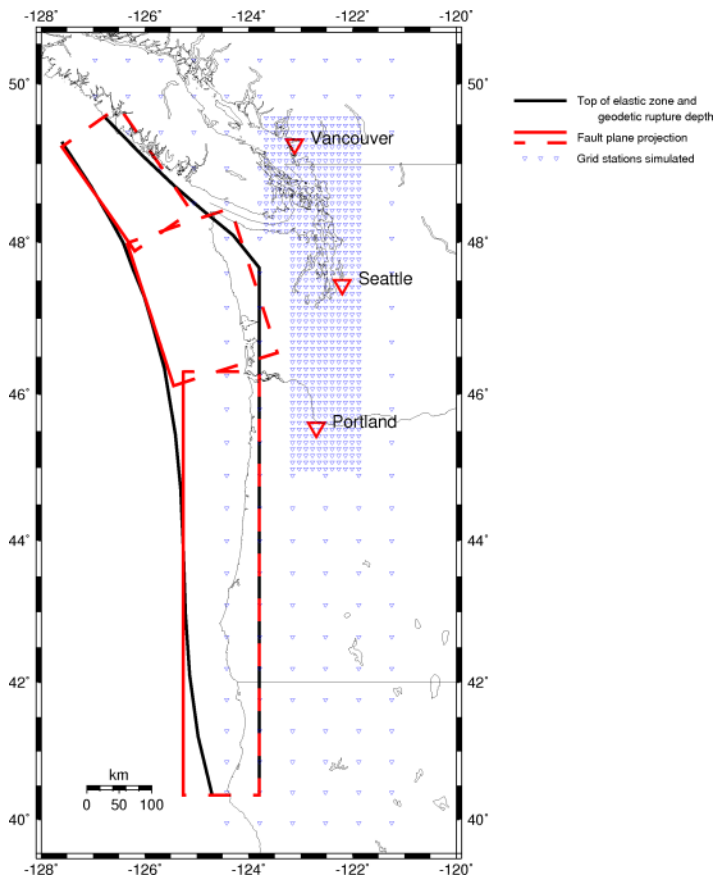

Figure 15. Modeled rupture geometry of the Cascadia subduction zone and the grid of stations used for strong motion simulation (blue triangles).

The relations between seismic moment and rupture area of subduction earthquakes derived by Somerville et al. (2002) from the rupture models of past earthquakes predict that the magnitude corresponding to a rupture area of 131,500 square km is Mw 8.7. So the source parameters of an earthquake with Mw 9.0, listed in Table 4, do not conform to the self-similar scaling relations of Somerville et al. (2002), but they are more consistent with the self-similar relations of Murotani et al. (2008).

Table 4. Source parameters of modeled M 9.0 earthquakes that rupture the whole Cascadia Subduction Zone.

Mw	Rupture Area (km^2)	Average Slip (cm)	Rise Time (s)	Slip Velocity (cm/s)
9.0	131,500	831	12.7	66.0

For the event listed in Table 4, we generated more than 100 different earthquake rupture models, for three different hypocentral locations, i.e. south, central and north, in order to study the variability and the sensitivity of the derived ground motions and tsunami inundation on the individual characteristics of each slip model used. We selected slip models 11, 27 and 87 for producing ground motion simulations. All three models have very similar average slip, although there are differences in the spatial distribution of slip, mostly down dip of the fault. For model 11 the slip is uniformly distributed along the fault, while for 27 and 87 the highest slip values are concentrated in the lower and upper parts of the fault, respectively. The rupture models of the Mw 9.0 event for the north hypocenter are shown in Figure 16.

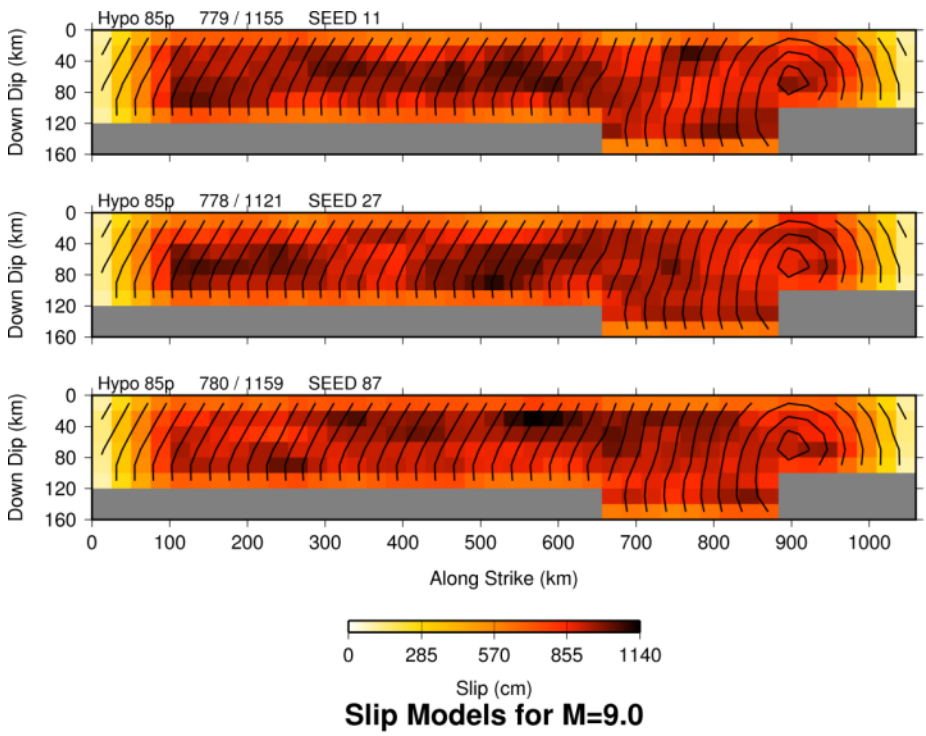

Figure 16. Rupture models of Mw 9.0 scenario earthquakes on the Cascadia subduction zone having northern hypocenters. The slip values of all models are the same for the different hypocenters (southern, central, and northern).

Crustal Structure

In previous studies in which we simulated the ground motions of Cascadia subduction earthquakes (e.g. Somerville et al., 2003; Somerville et al., 2013) we demonstrated the adequacy of Green's functions computed using a series of 1D approximations to a 2D seismic velocity model of the Cascadia subduction zone by comparing the 1D and 2D Green's functions (Cohee et al., 1991). The 2D model used a simple model of the subcrustal structure from the Lithoprobe transect (Clowes et al., 1987). Subsequent work by Brocher et al. (2003) and McNeill et al. (2004) indicates the presence of a serpentinized forearc upper mantle along the Cascadia margin. This forearc has significantly lower seismic velocities than those of Clowes et al. (1987) used in the ground motion study by Cohee et al. (1991).

McNeill et al. (2004) analyzed the effect of a serpentinized forearc upper mantle along the Cascadia margin on ground motions from megathrust earthquakes, and concluded that it has a relatively minor effect. It alters the distance range over which postcritically reflected S waves dominate by shifting the reflecting interface from the continental Moho to the oceanic Moho, but does not significantly affect the amplitudes. Accordingly, we conclude that it is not critical to use full 2D or 3D Green's functions in our simulations, and so we used Green's functions computed using a 1D approximation to the velocity model of the Cascadia subduction zone. We found that the velocity model we used for Peru is broadly compatible with the velocity model for Cascadia described McNeill et al. (2004). This velocity model, which has velocities that are considerably lower than those used by Cohee et al. (1991), is shown in Table 5.

Table 5. Crustal structure model for Cascadia.

Vp (km/s)	*Qp*	*Vs (km/s)*	*Qs*	*Density (Kgr/m^3)*	*Thickness (km)*
2.600	2000	1.500	900.0	2.000	0.20
5.300	2000	3.030	900.0	2.100	6.70
6.000	2000	3.370	900.0	2.500	4.60
6.500	2000	3.650	900.0	2.780	18.10
7.300	2000	4.100	900.0	3.180	15.80
8.100	2000	4.500	900.0	3.400	16.00
8.101	2000	4.501	900.0	3.401	100.00

Another important influence on the amplitude and durations on strong ground motions is the effect of sedimentary basins, such as the Puget Trough and the Portland and Tualatin basins. We have addressed basin response in these locations in other studies (Ichinose, 2003b; Pitarka et al., 2002), and recognize that this is an important issue to be addressed in future studies, but it lies beyond the scope of this report.

Ground Motion Attenuation

The attenuation of ground motion with distance derived from the strong motion simulations is shown in Figures 17-36. At first (Figures 17-28), the simulated ground motion values (the three different hypocentral locations are shown in different colors) and a simple model that is fit to those values

(shown by a solid black line) are compared with the three ground motion models for various spectral periods. The second set of Figures (29-36) compares the response spectra of the simulations of the Mw 9.0 Cascadia earthquakes with the three ground motion models in a suite of distance ranges. Both comparisons are presented for two sites conditions, NEHRP B/C boundary and NEHRP D, respectively.

From the first set of figures, it is clear that there are differences between the three ground motion models and our model, especially in the slopes of the attenuation curves. For close distances (R<50 km) there is fairly good agreement between the GMPEs and our model, which gradually improves with increasing periods. For larger distances, the three models underpredict the simulated ground motions, exhibiting stronger distance decay than our model, particularly at shorter periods, while for longer periods the results are in better agreement.

In most cases the Atkinson and Boore (2003) model underpredicts the simulated response spectra, especially at closer distances, in agreement with the comparisons presented in the previous response spectrum comparisons. The Zhao et al. (2006) and Abrahamson et al. (2012) models are in closer agreement with our results, particularly for distances < 200km.

In order to scale the synthetic response spectra to the two selected site conditions, we used the BSSA13 site amplification factors. The scaled synthetic response spectra capture the general characteristics of the empirical models, as shown previously. Although the BSSA13 site amplification factors are applicable to response spectra from horizontal components, we have also applied them to the vertical components, so the scaled vertical component response spectra values are only indicative.

From both sets of figures it can be seen that the differences among the various slip models used are very small, exhibiting practically identical ground motions for the whole period and distance range studied.

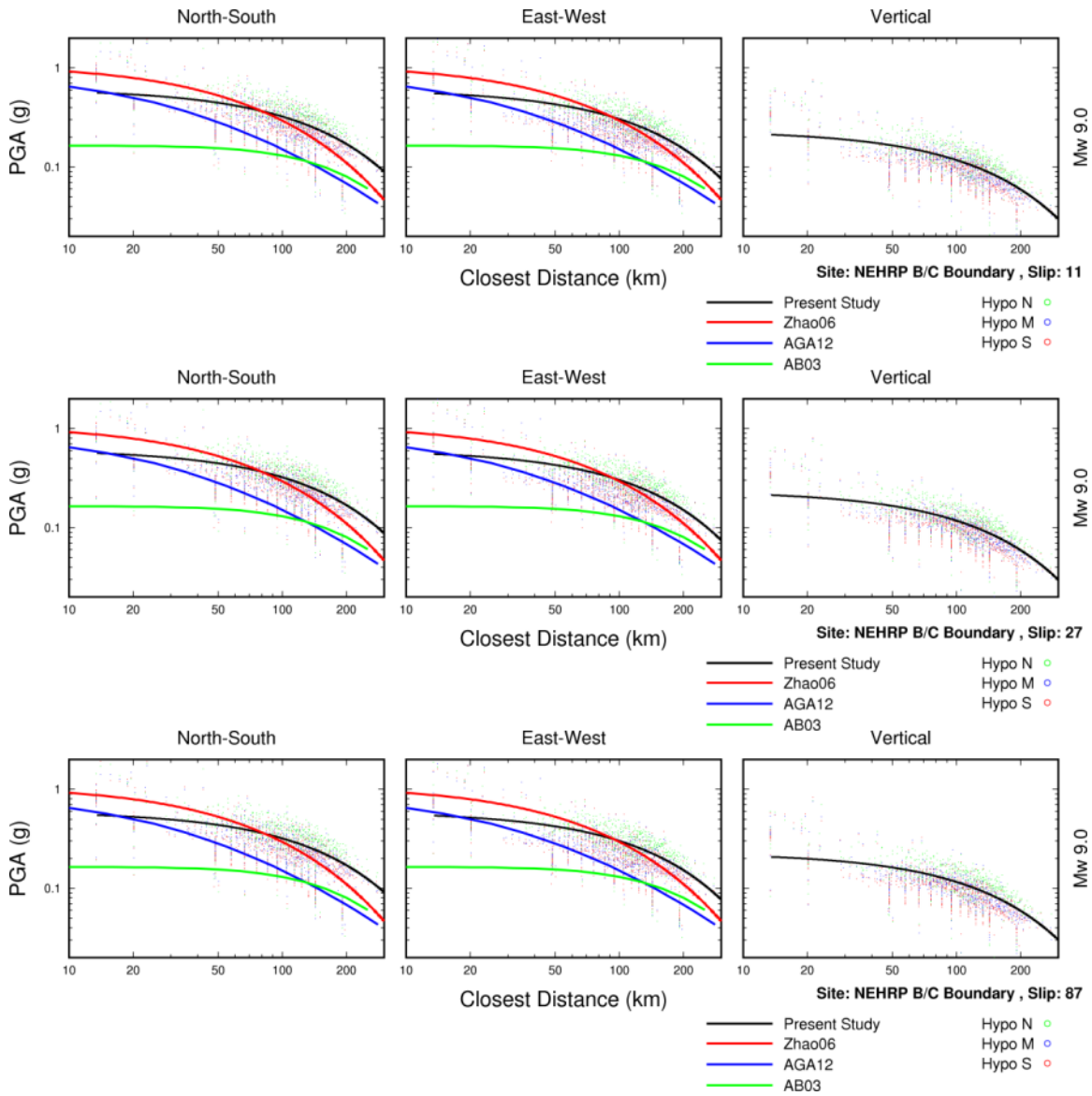

Figure 17. Comparison of simulated peak accelerations (points and black line), for various slip models for Mw 9.0 Cascadia earthquake with ground motion models for the NEHRP B/C site categories boundary.

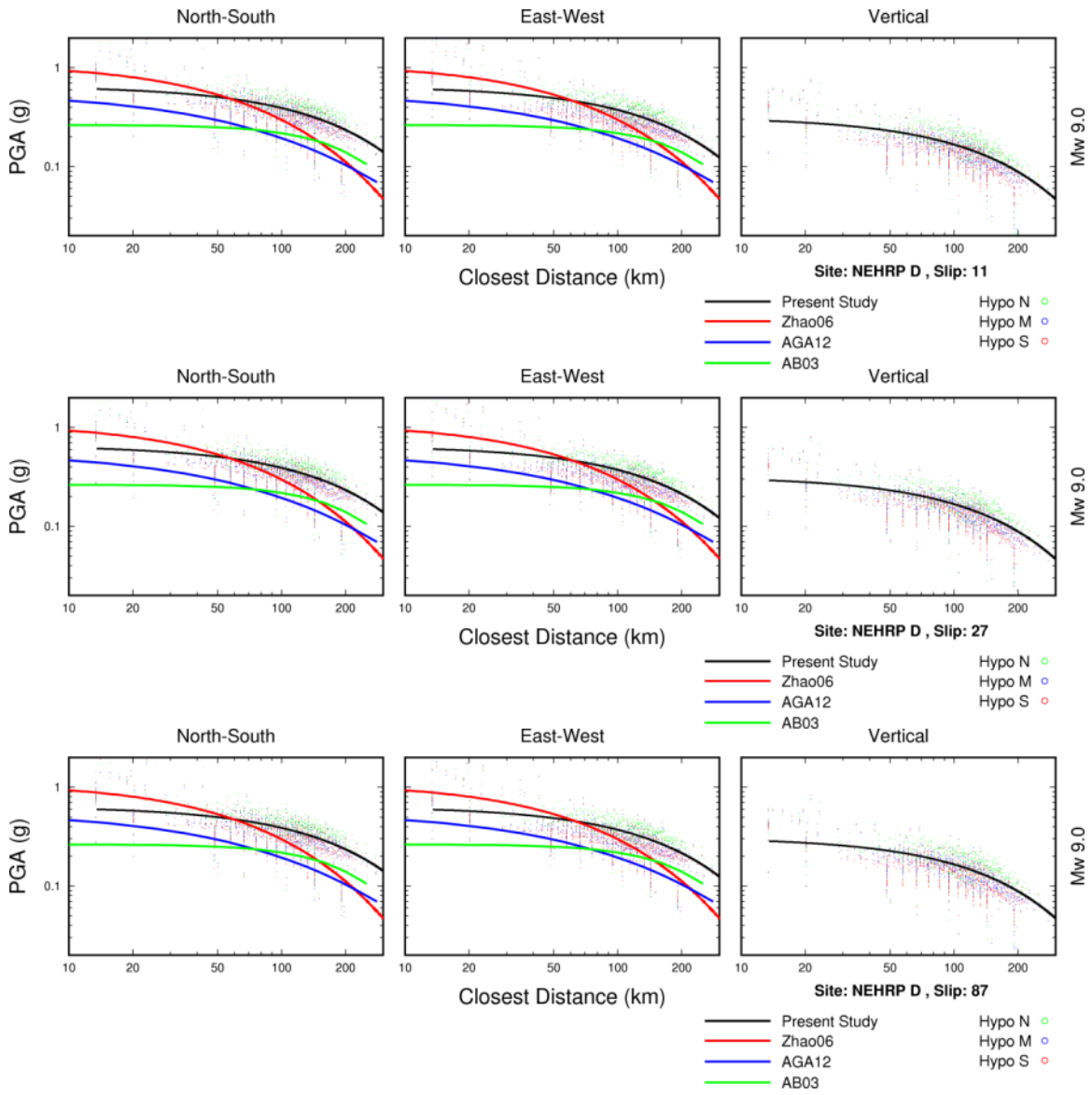

Figure 18. Comparison of simulated peak accelerations (points and black line), for various slip models for Mw 9.0 Cascadia earthquake with ground motion models for NEHRP D site category.

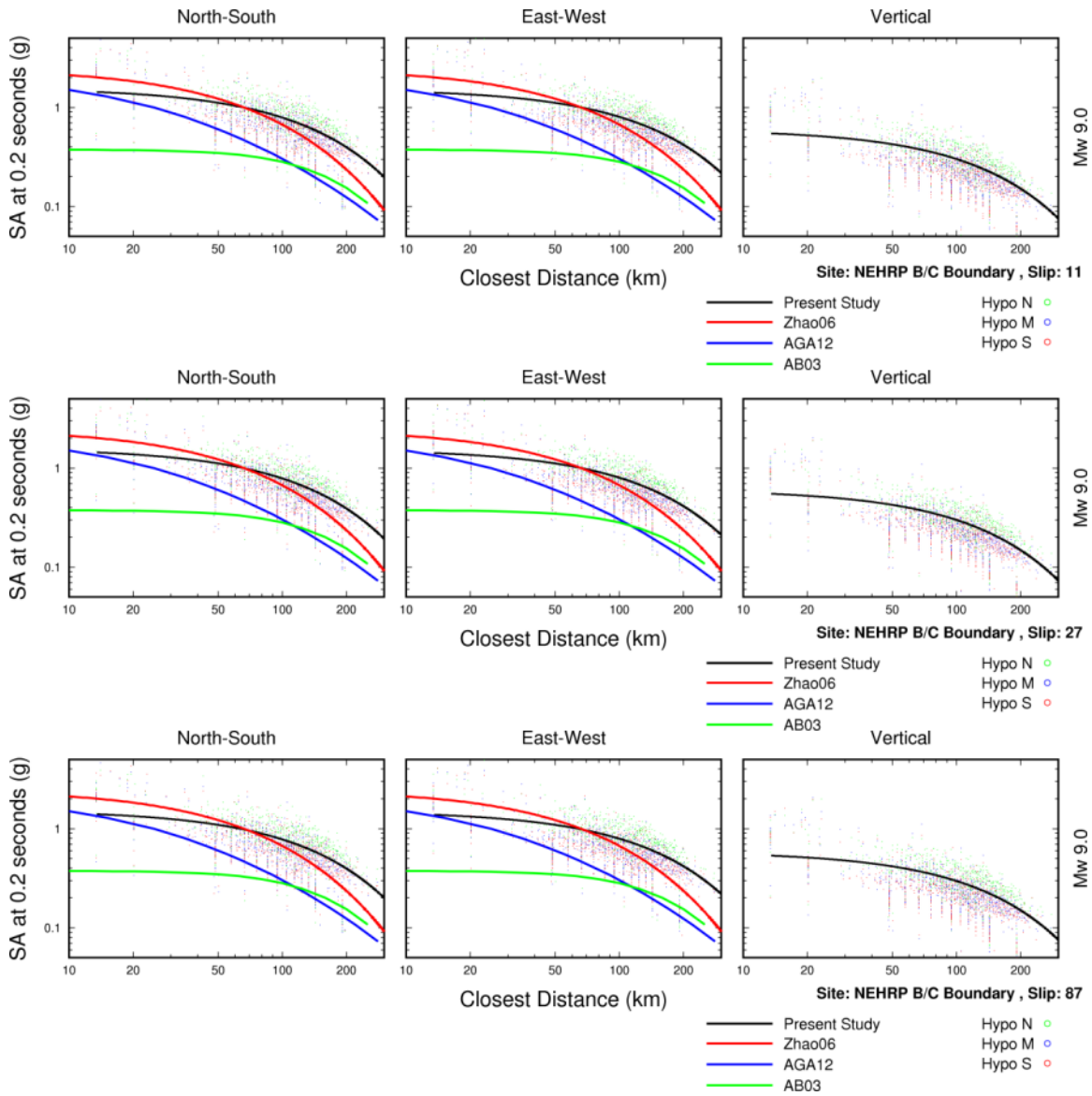

Figure 19. Comparison of simulated 0.2 sec spectral accelerations (points and black line), for various slip models for Mw 9.0 Cascadia earthquake with ground motion models for the NEHRP B/C site categories boundary.

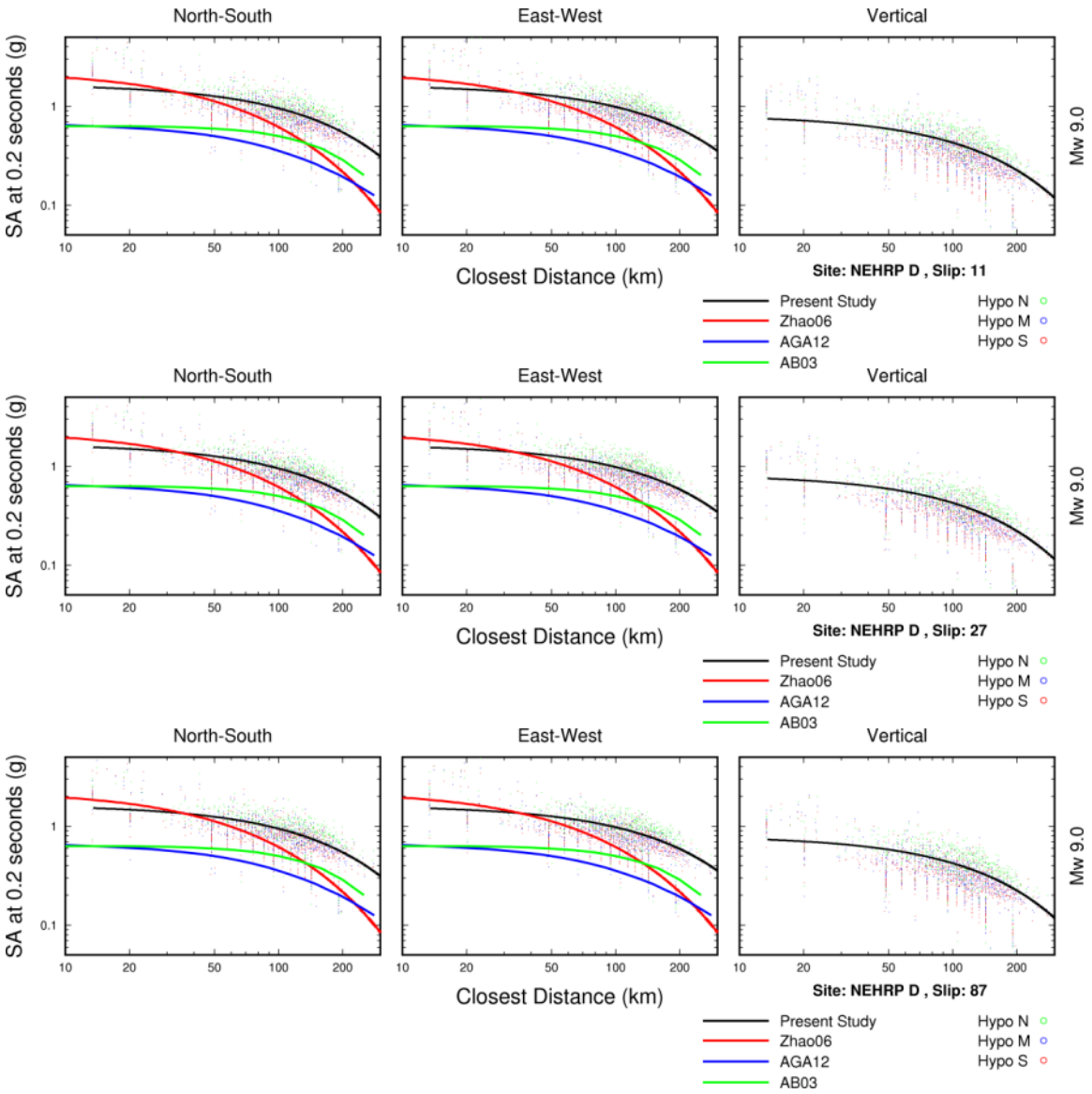

Figure 20. Comparison of simulated 0.2 sec spectral accelerations (points and black line), for various slip models for Mw 9.0 Cascadia earthquake with ground motion models for NEHRP D site category.

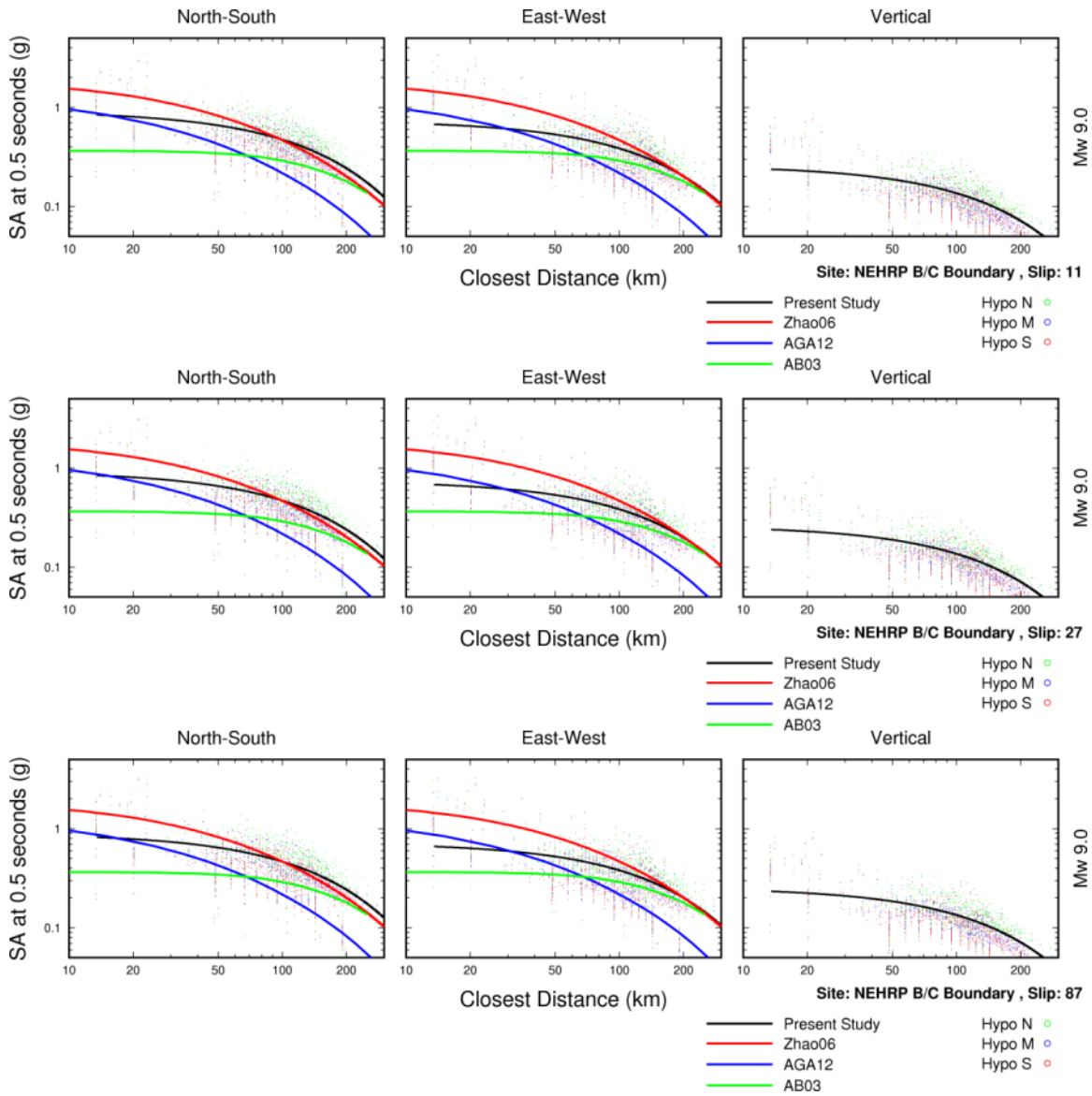

Figure 21. Comparison of simulated 0.5 sec spectral accelerations (points and black line), for various slip models for Mw 9.0 Cascadia earthquake with ground motion models for the NEHRP B/C site categories boundary.

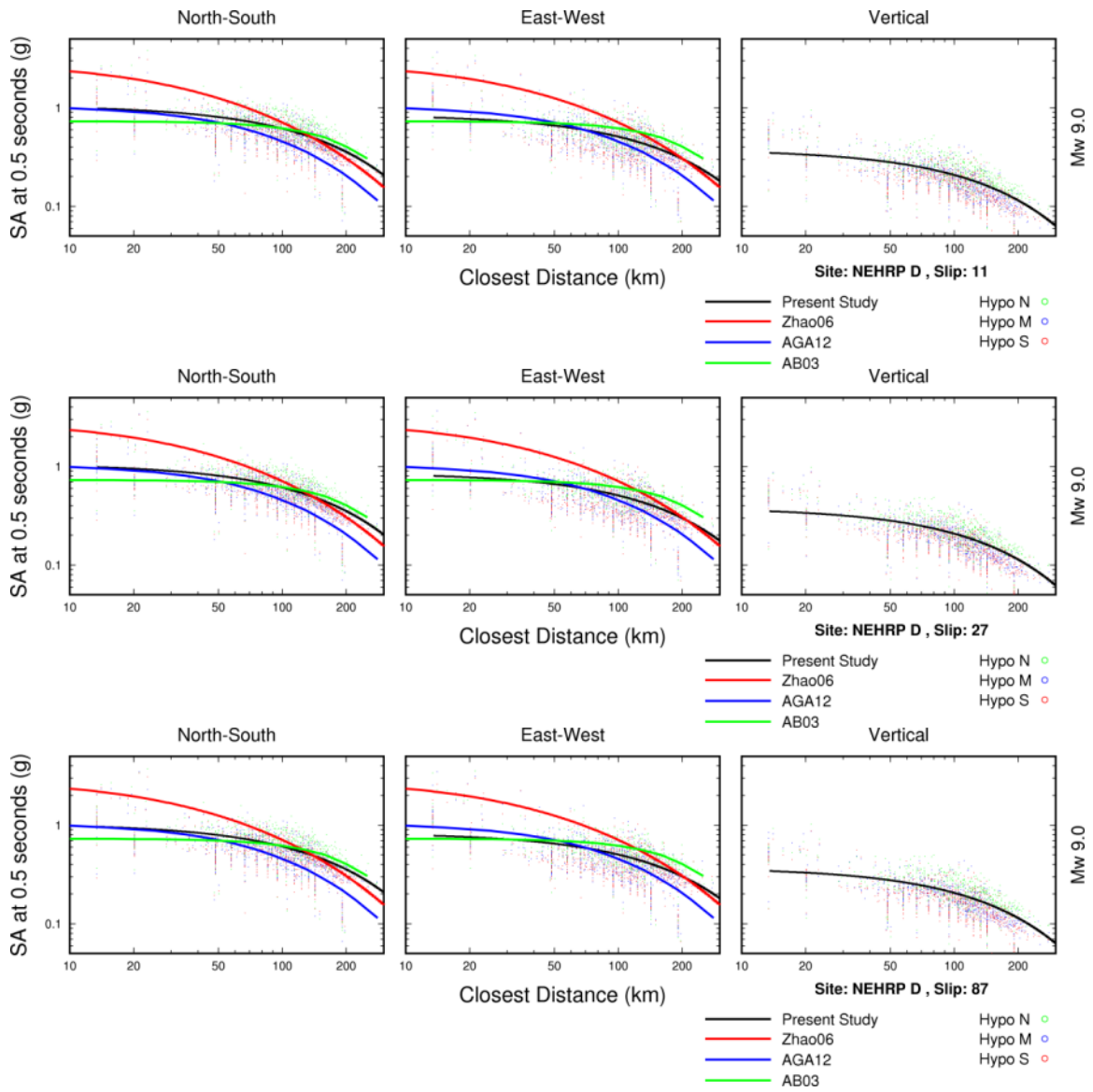

Figure 22. Comparison of simulated 0.5 sec spectral accelerations (points and black line), for various slip models for Mw 9.0 Cascadia earthquake with ground motion models for NEHRP D site category.

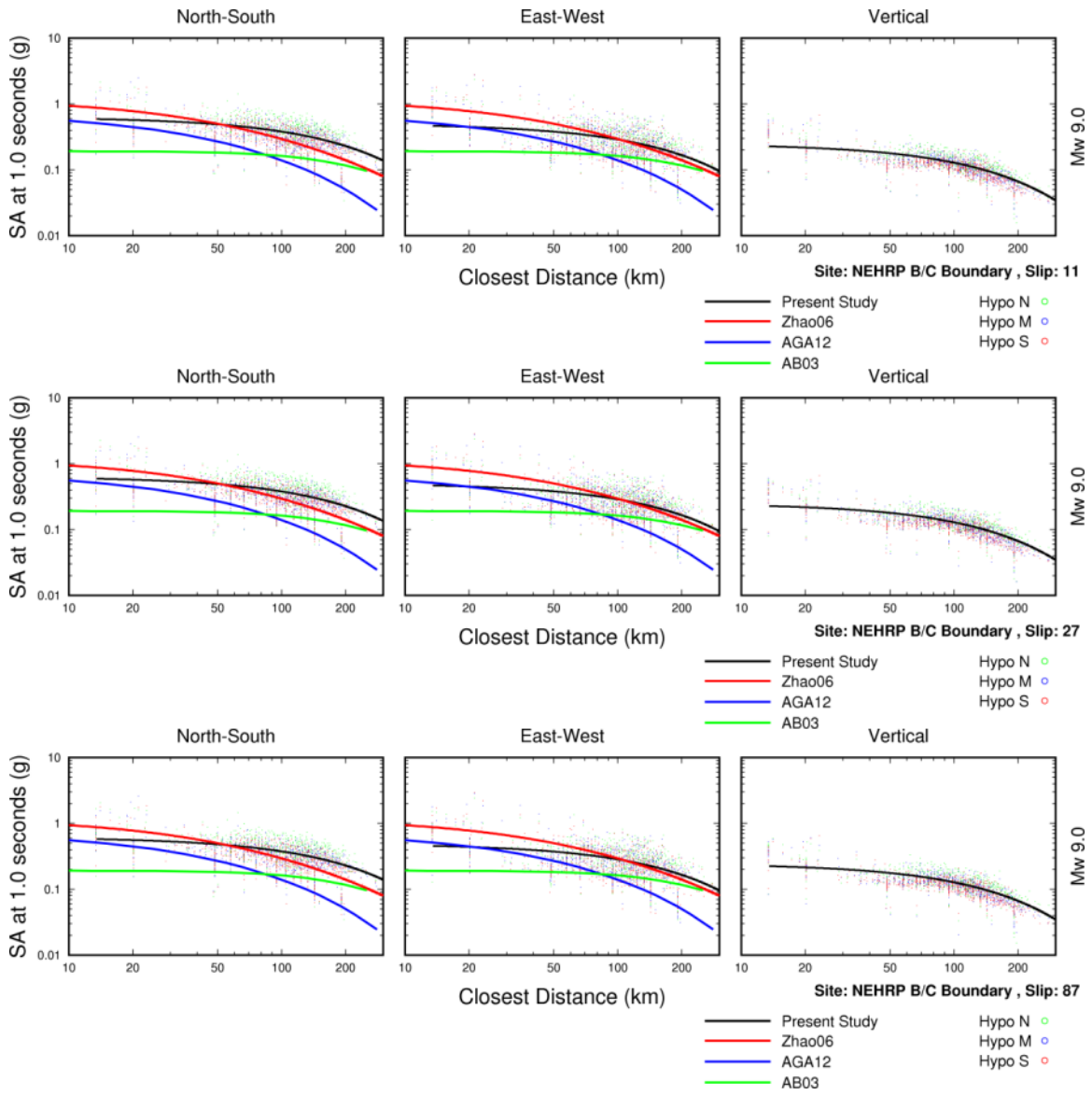

Figure 23. Comparison of simulated 1 sec spectral accelerations (points and black line), for various slip models for Mw 9.0 Cascadia earthquake with ground motion models for the NEHRP B/C site categories boundary.

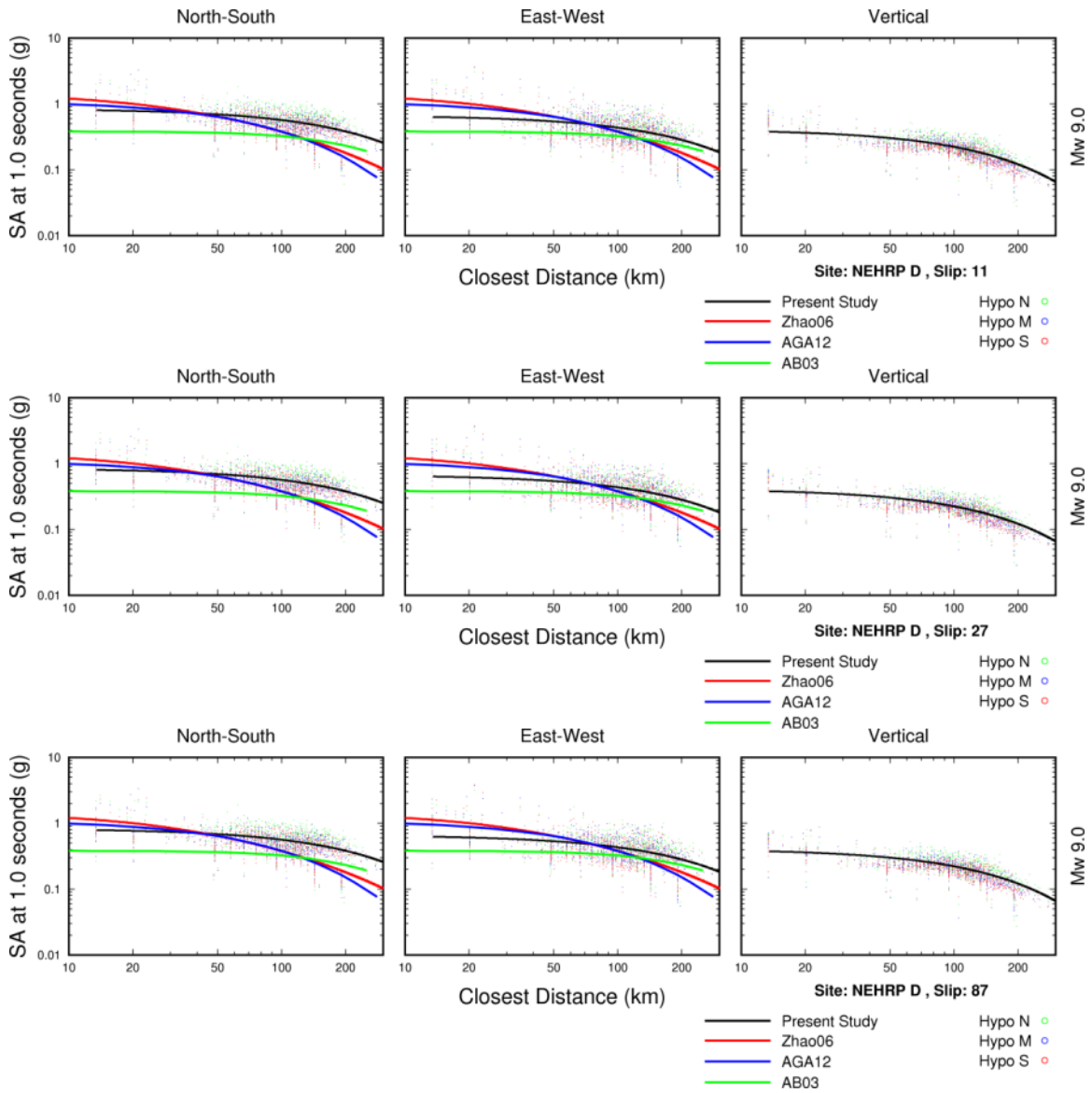

Figure 24. Comparison of simulated 1 sec spectral accelerations (points and black line), for various slip models for Mw 9.0 Cascadia earthquake with ground motion models for NEHRP D site category.

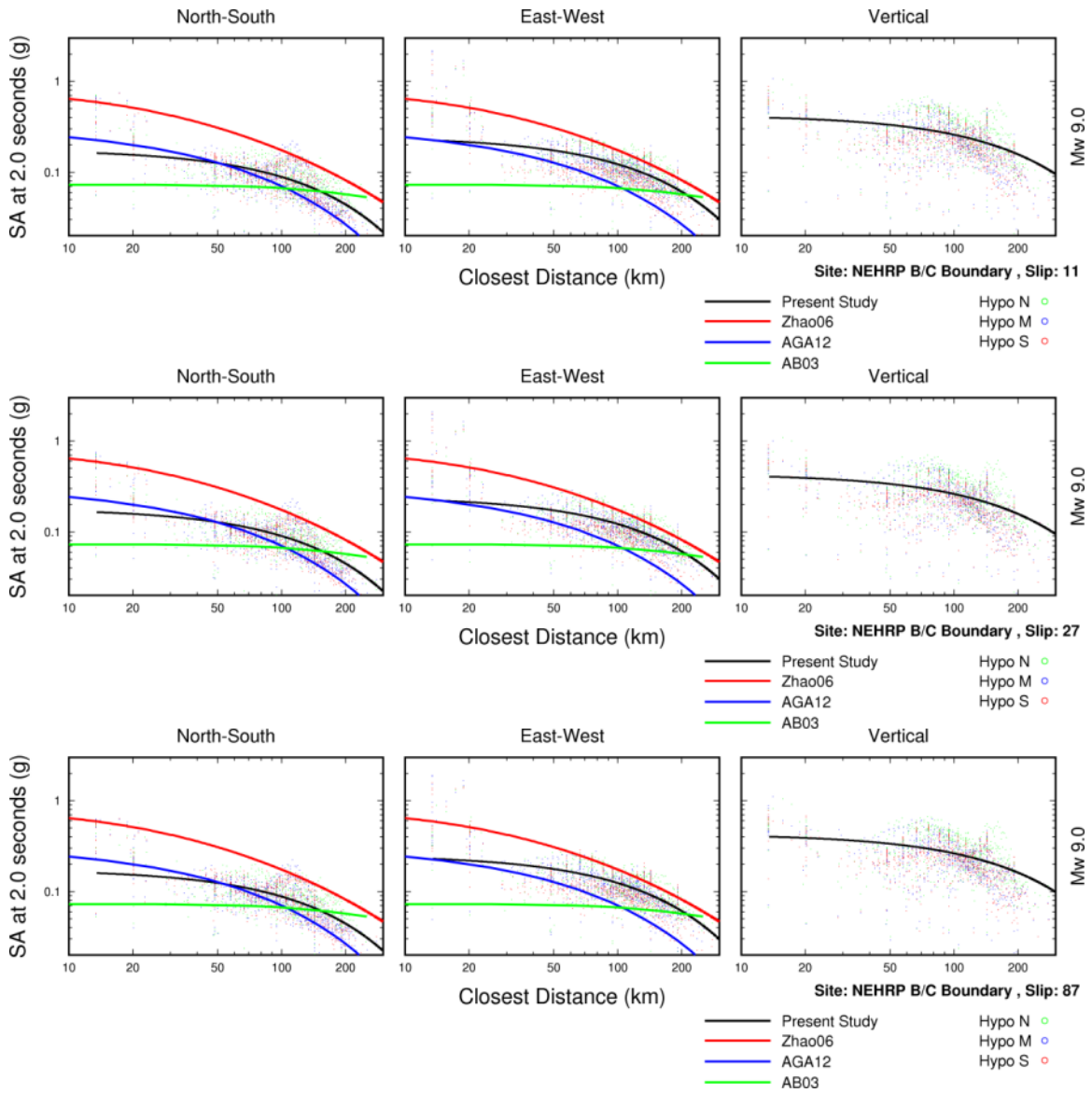

Figure 25. Comparison of simulated 2 sec spectral accelerations (points and black line), for various slip models for Mw 9.0 Cascadia earthquake with ground motion models for the NEHRP B/C site categories boundary.

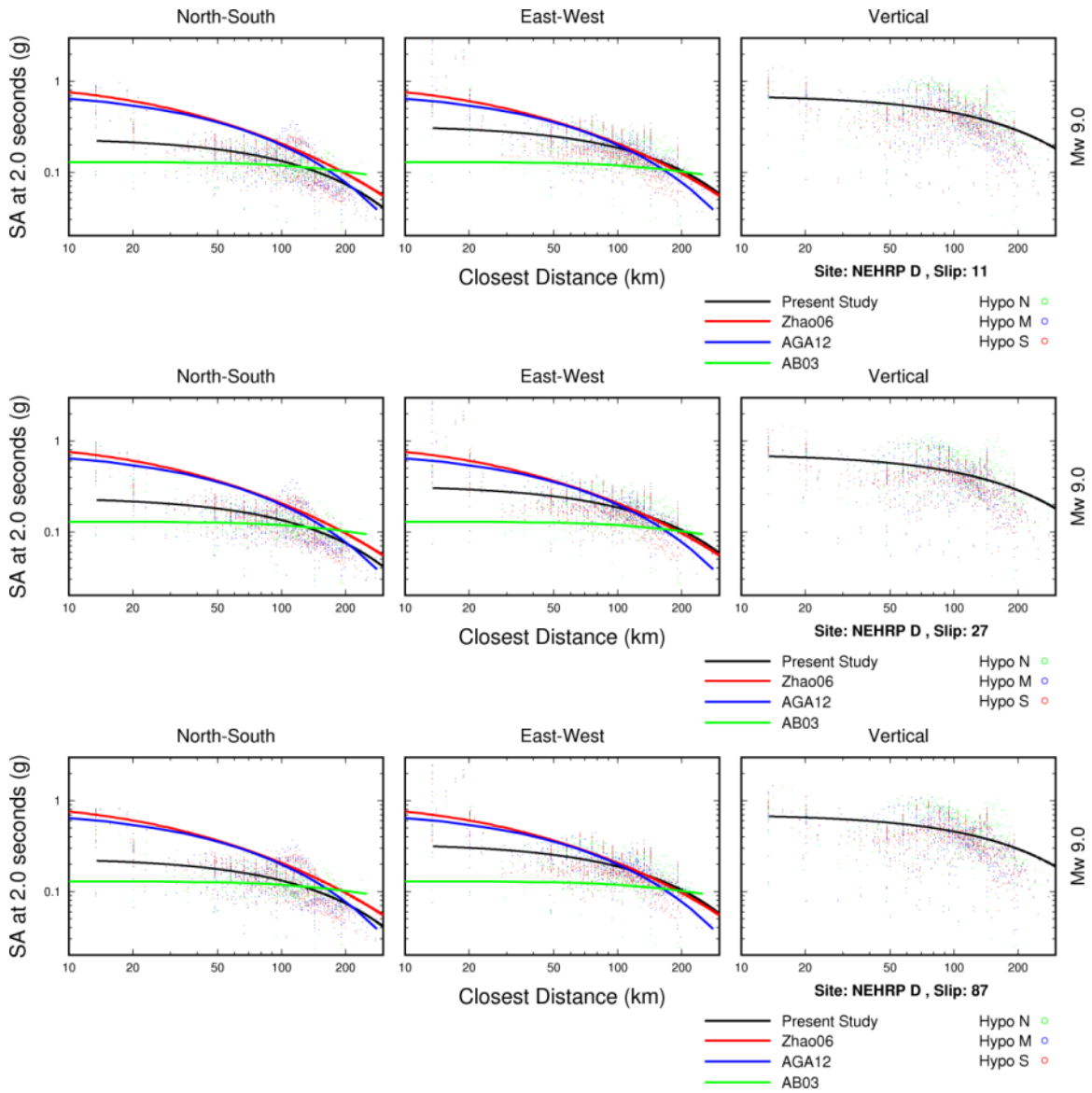

Figure 26. Comparison of simulated 2 sec spectral accelerations (points and black line), for various slip models for Mw 9.0 Cascadia earthquake with ground motion models for NEHRP D site category.

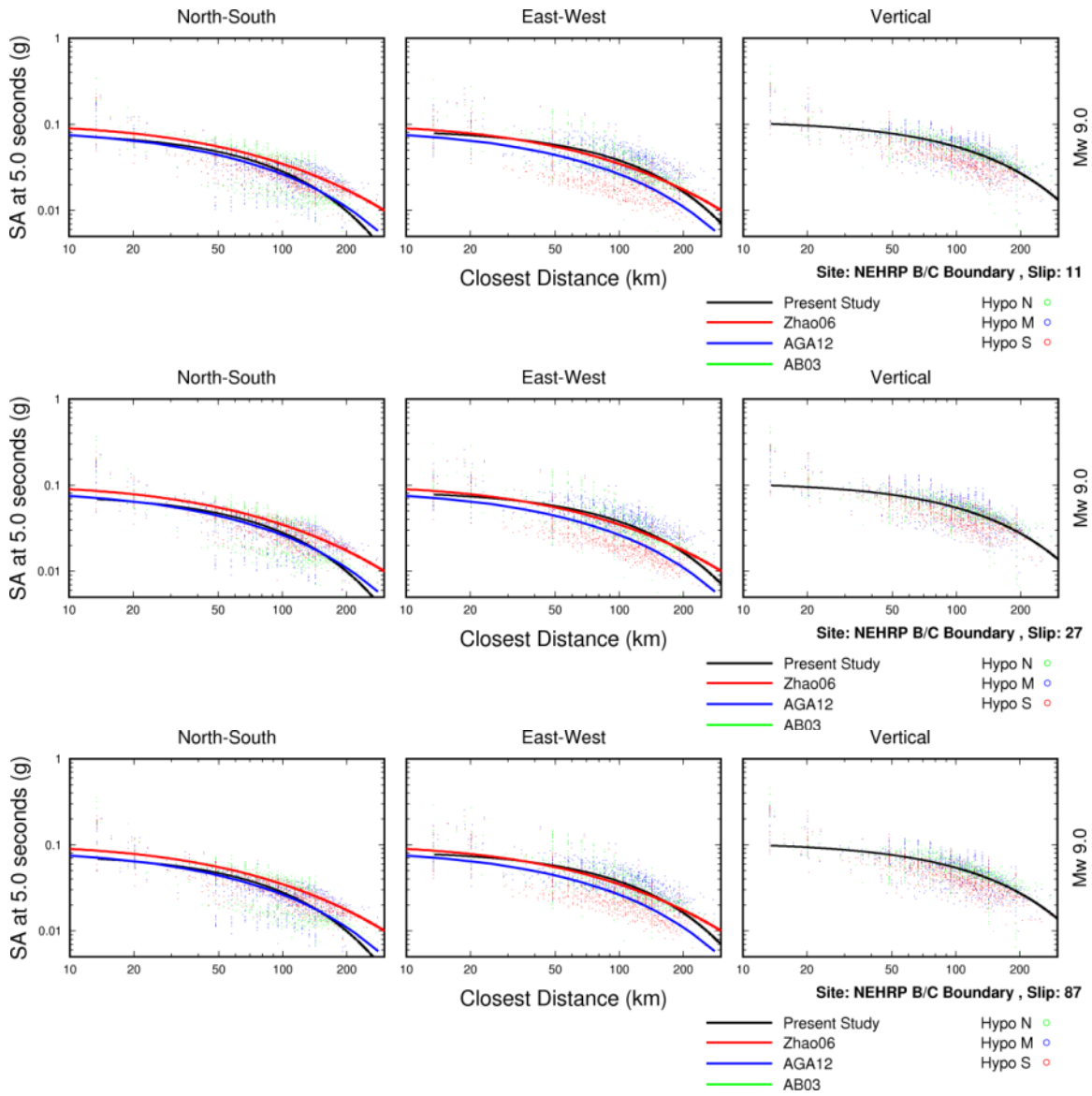

Figure 27. Comparison of simulated 5 sec spectral accelerations (points and black line), for various slip models for Mw 9.0 Cascadia earthquake with ground motion models for the NEHRP B/C site categories boundary.

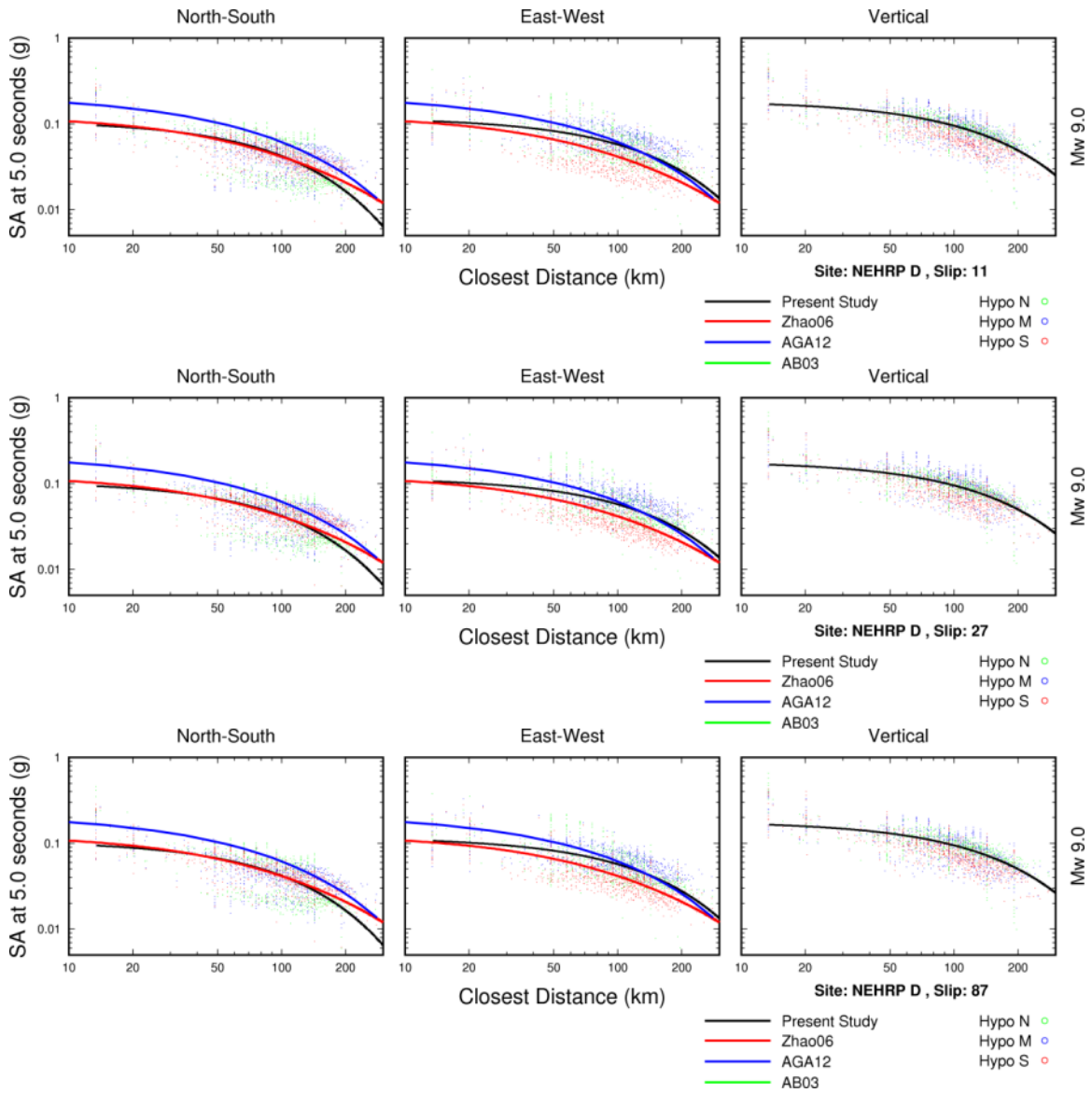

Figure 28. Comparison of simulated 5 sec spectral accelerations (points and black line), for various slip models for Mw 9.0 Cascadia earthquake with ground motion models for NEHRP D site category.

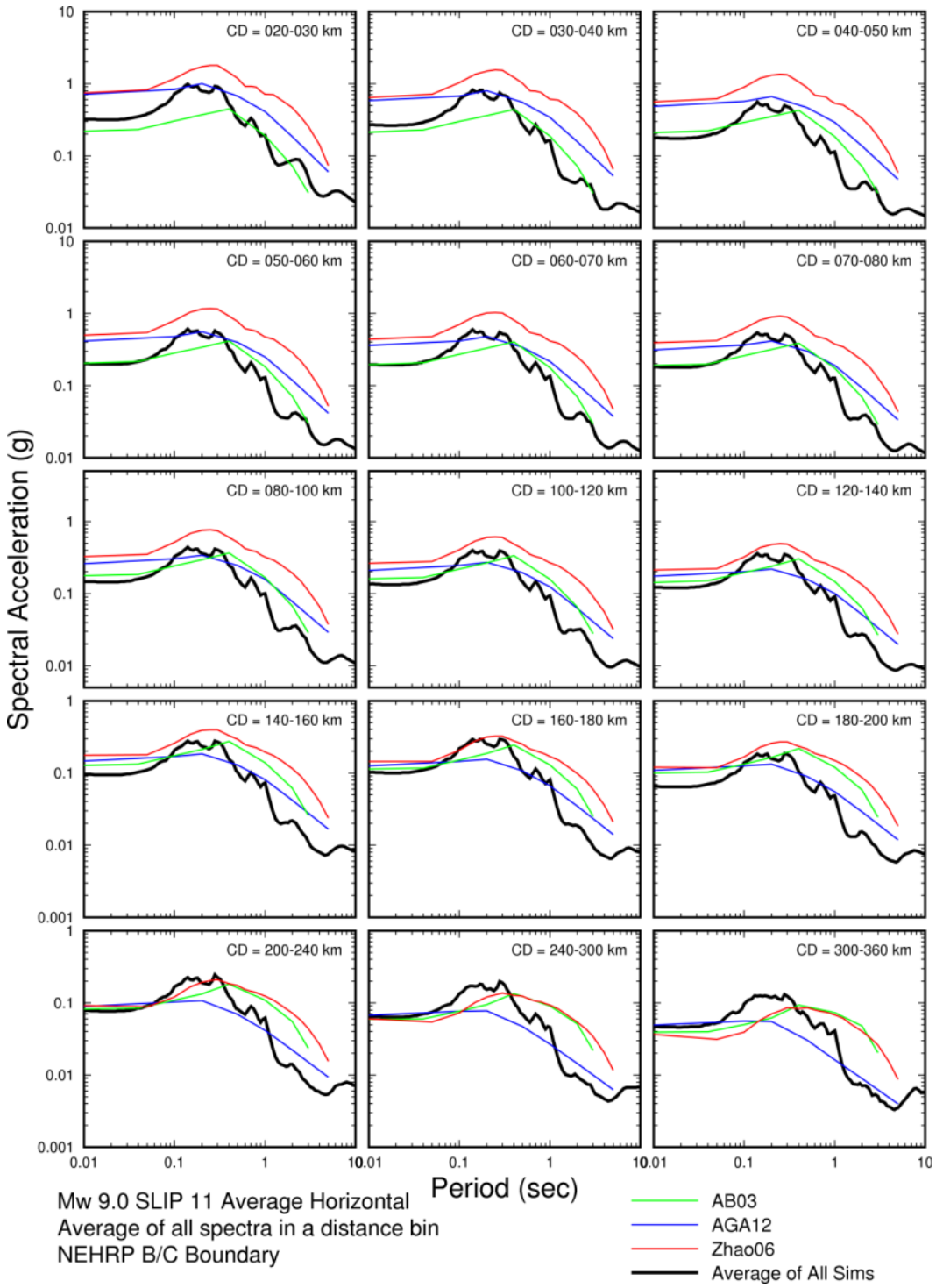

Figure 29. Comparison of simulated response spectra for a suite of distance ranges for Mw 9.0 Cascadia earthquake for NEHRP B/C site categories boundary with three ground motion models, and a ground motion model representing the simulations, for slip model 11.

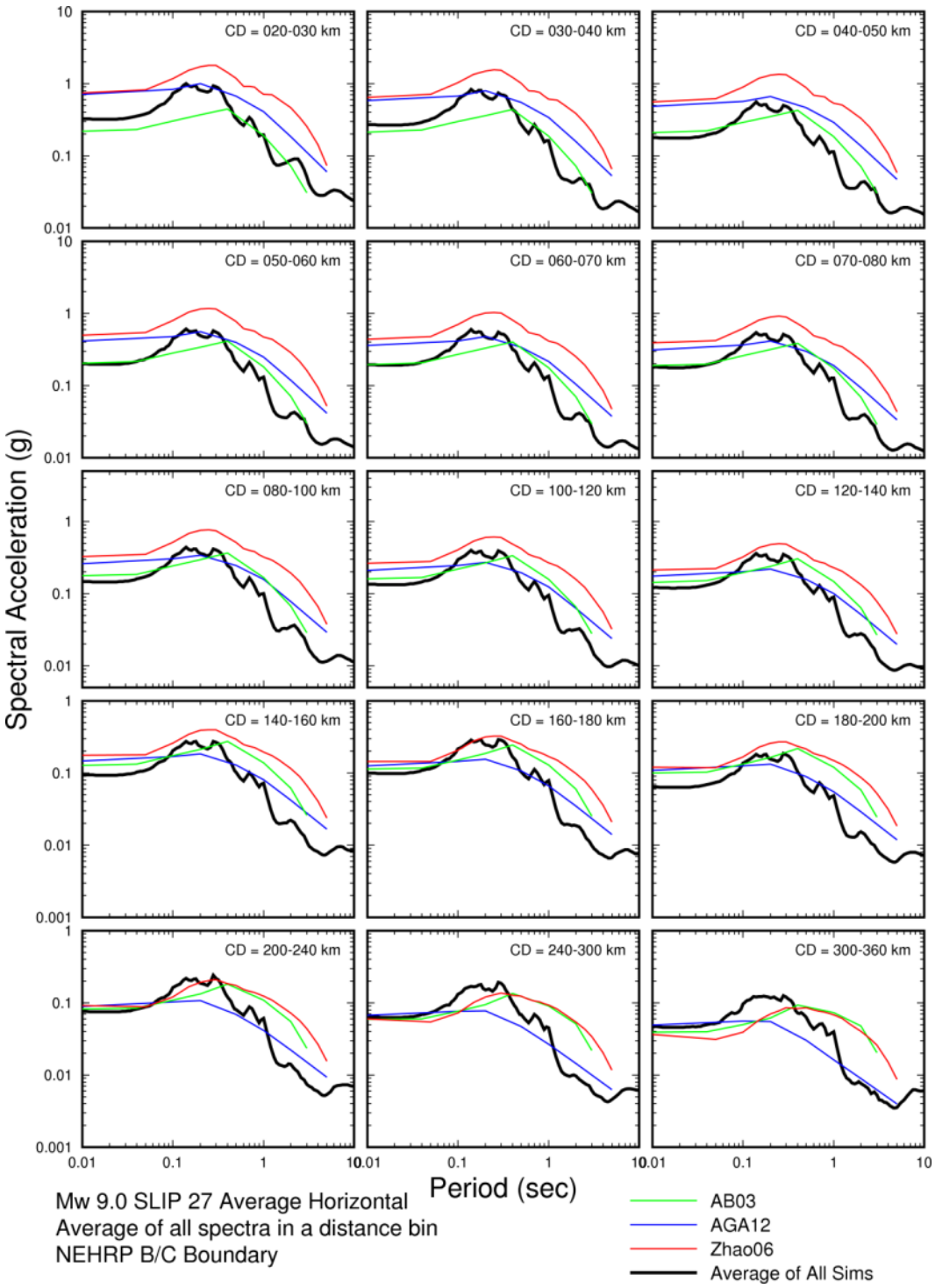

Figure 30. Comparison of simulated response spectra for a suite of distance ranges for Mw 9.0 Cascadia earthquake for NEHRP B/C site categories boundary with three ground motion models, and a ground motion model representing the simulations, for slip model 27.

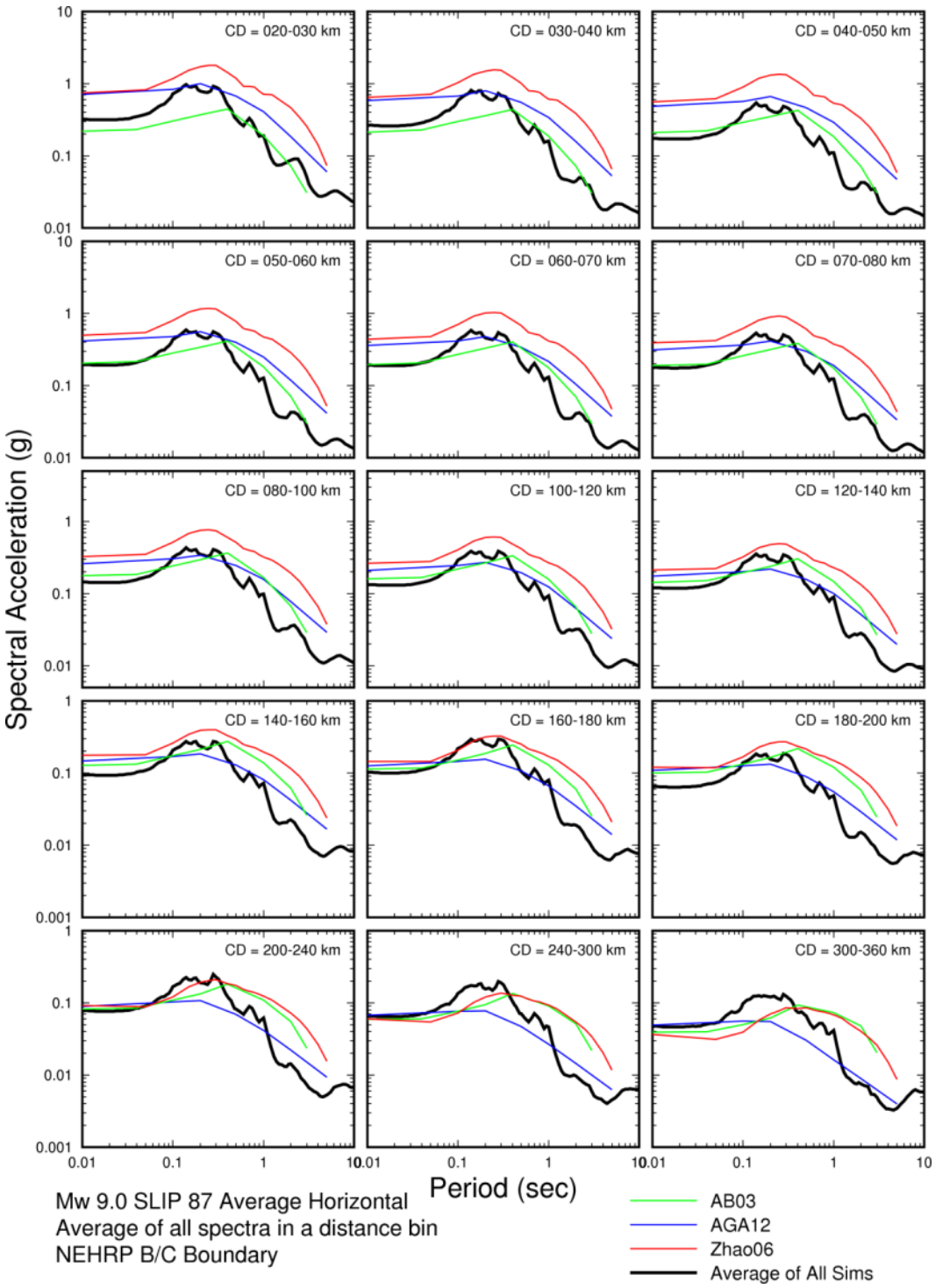

Figure 31. Comparison of simulated response spectra for a suite of distance ranges for Mw 9.0 Cascadia earthquake for NEHRP B/C site categories boundary with three ground motion models, and a ground motion model representing the simulations, for slip model 87.

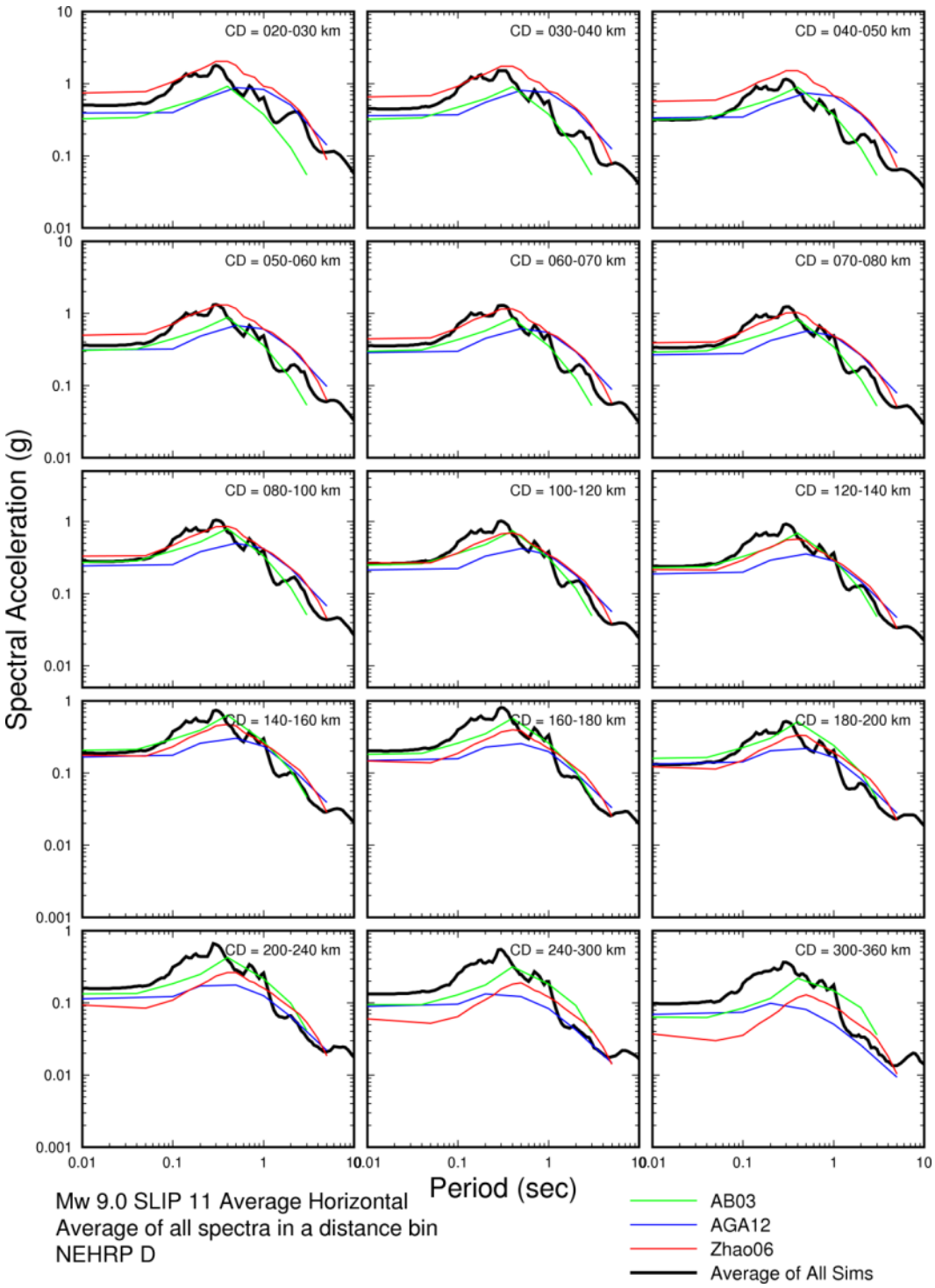

Figure 32. Comparison of simulated response spectra for a suite of distance ranges for Mw 9.0 Cascadia earthquake for NEHRP D site category with three ground motion models, and a ground motion model representing the simulations, for slip model 11.

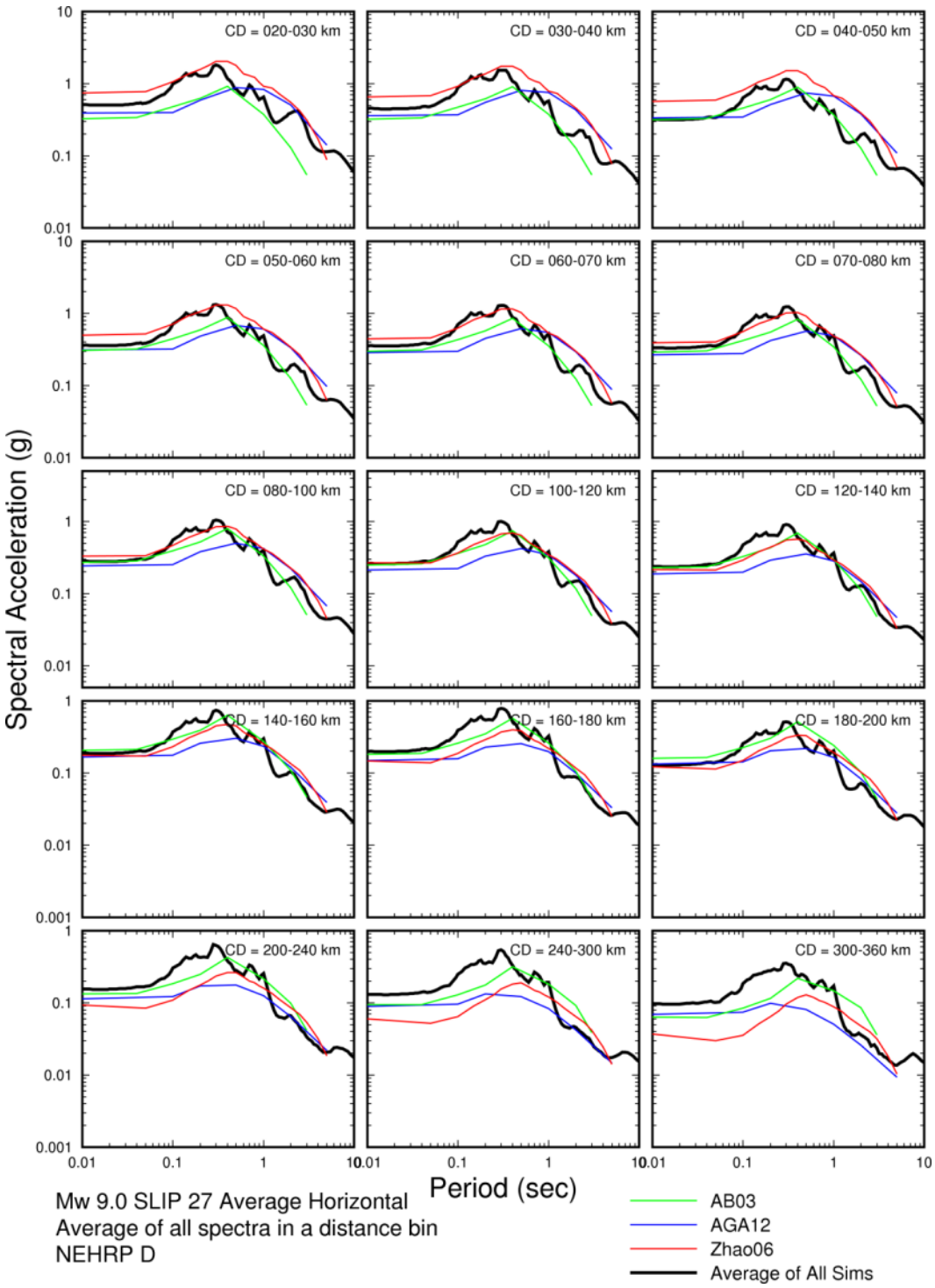

Figure 33. Comparison of simulated response spectra for a suite of distance ranges for M 9.0 Cascadia earthquake for NEHRP D site category with three ground motion models, and a ground motion model representing the simulations, for slip model 27.

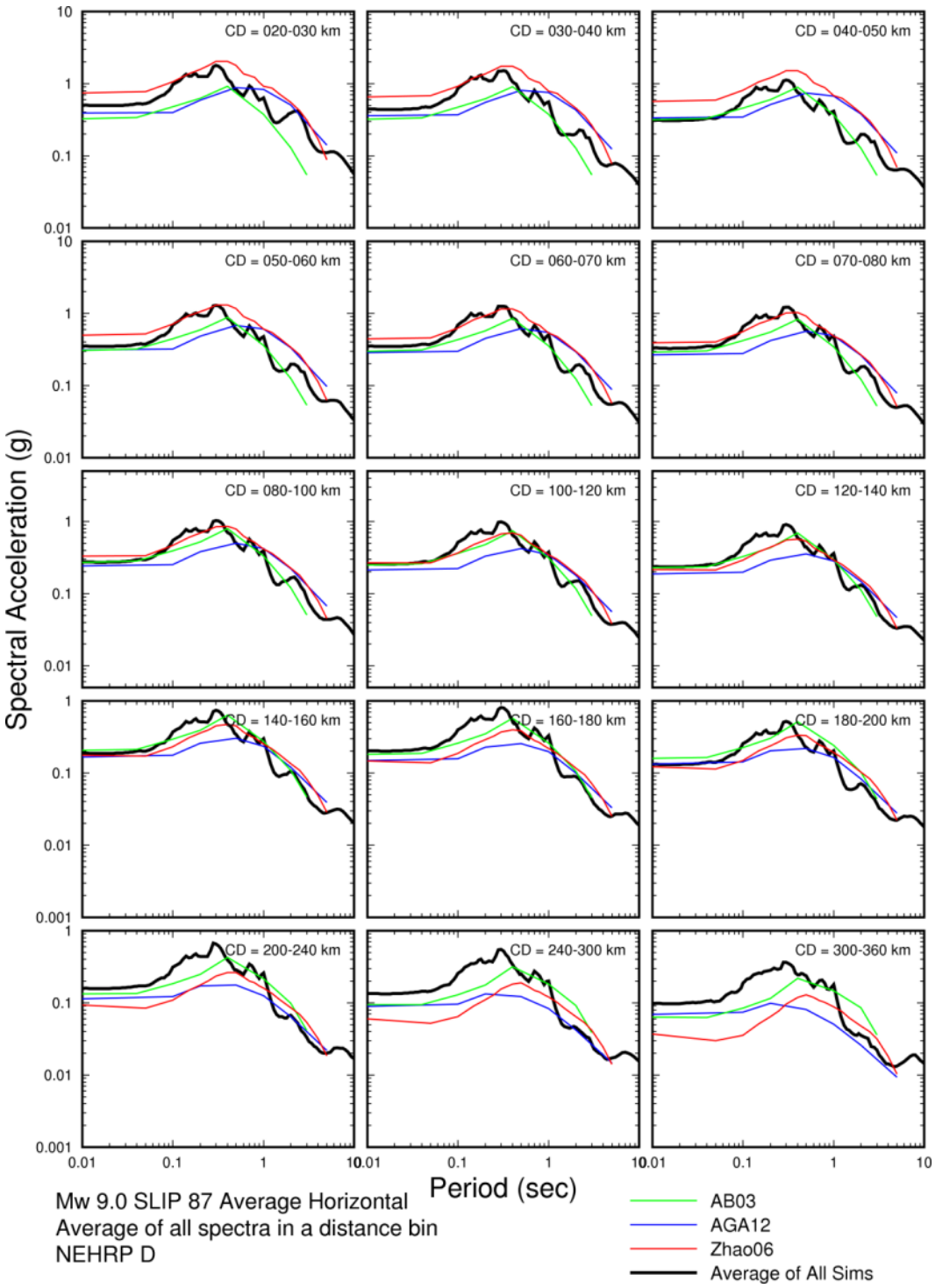

Figure 34. Comparison of simulated response spectra for a suite of distance ranges for M 9.0 Cascadia earthquake for NEHRP D site category with three ground motion models, and a ground motion model representing the simulations, for slip model 87.

We averaged the simulations over the three hypocenter locations and the two horizontal components for the different slip models, to obtain simple ground motion models for Mw 9.0 earthquakes. The ground motion model coefficients for the 3 slip models used are given in Tables 6 and 7. We consider that these ground motion models are appropriate for estimating the response spectra of ground motions of earthquakes that rupture the entire Cascadia Plate Interface.

Table 6. Ground motion model for Mw 9.0 earthquakes rupturing the entire Cascadia Plate Interface, for NEHRP B/C site categories boundary.

	Slip model 11		*Slip model 27*		*Slip model 87*	
Period (s)	C_1	C_2	C_1	C_2	C_1	C_2
0.01	-0.6075	-0.0073	-0.5987	-0.0074	-0.6344	-0.0071
0.10	0.1534	-0.0074	0.1620	-0.0076	0.1237	-0.0073
0.20	0.3169	-0.0072	0.3276	-0.0073	0.2908	-0.0071
0.50	-0.2874	-0.0071	-0.2770	-0.0072	-0.3127	-0.0070
1.00	-0.6519	-0.0058	-0.6416	-0.0059	-0.6771	-0.0057
2.00	-1.5027	-0.0081	-1.5052	-0.0081	-1.4857	-0.0082
5.00	-2.7036	-0.0078	-2.6631	-0.0080	-2.6835	-0.0080
10.00	-3.1680	-0.0052	-3.0863	-0.0057	-3.1404	-0.0054
20.00	-4.2122	-0.0049	-4.1156	-0.0055	-4.2050	-0.0052

The simulations are fit to the simple ground motion model: $\mathrm{Ln(Sa)} = C_1 + C_2 * R_{cld}$

Table 7. Ground motion model for Mw 9.0 earthquakes rupturing the entire Cascadia Plate Interface, for NEHRP D site category.

	Slip model 11		*Slip model 27*		*Slip model 87*	
Period (s)	C_1	C_2	C_1	C_2	C_1	C_2
0.01	-0.5039	-0.0059	-0.4963	-0.0060	-0.5250	-0.0058
0.10	0.2570	-0.0061	0.2643	-0.0062	0.2331	-0.0060
0.20	0.4206	-0.0058	0.4300	-0.0060	0.4002	-0.0058
0.50	-0.1073	-0.0058	-0.0984	-0.0059	-0.1272	-0.0058
1.00	-0.3263	-0.0046	-0.3177	-0.0047	-0.3465	-0.0045
2.00	-1.1772	-0.0070	-1.1813	-0.0069	-1.1550	-0.0070
5.00	-2.3780	-0.0066	-2.3392	-0.0068	-2.3528	-0.0069
10.00	-2.8424	-0.0040	-2.7624	-0.0045	-2.8098	-0.0043
20.00	-3.8866	-0.0037	-3.7917	-0.0043	-3.8743	-0.0040

The simulations are fit to the simple ground motion model: $\mathrm{Ln(Sa)} = C_1 + C_2 * R_{cld}$

Ground Motion Maps

We performed ground motion simulations at the stations shown by the grid in Figure 13. We then generated ground motion maps for each of the three rupture scenarios. The maps, shown in Figures 35 through 46, are for peak acceleration and response spectral acceleration at 0.2, 0.5, 1.0, 2.0, and 5.0 seconds for three different slip models and for two site conditions; NEHRP B/C boundary and NEHRP C, respectively.

The highest values are observed for periods of 0.2s and 0.5s and cover a broad area of the Olympic Peninsula, independent of the hypocentral location of the scenario earthquake. However, for the longer periods of ground motion (T>1s) the maximum values of ground motion can be identified in a well-defined coastal zone which extends from Washington to the northern parts of California.

In Figure 46 the spatial distribution of the PGA/PGV ratios computed for each slip model used in the simulations is presented together with the corresponding histograms of the ratio values. The PGA/PGV ratios are used as a measure of the variability of the spectral content of ground motions. Lay et al. (2012) have shown that for megathrust earthquakes, such as the one simulated for Cascadia, the spectral content of the recorded ground motions has depth varying characteristics, with the deeper ones producing ground motions richer in shorter periods and the shallower ones in longer periods, respectively. With the three different slip models that we have selected we have tried to replicate this pattern and identify these properties in our simulations. As can be seen from the results of Figure 46, we cannot identify any significant differences in the simulated ground motions. Modifications in the method used for producing the stochastic slip models would be needed in order to take into account these features, but such work is beyond the scope of this project.

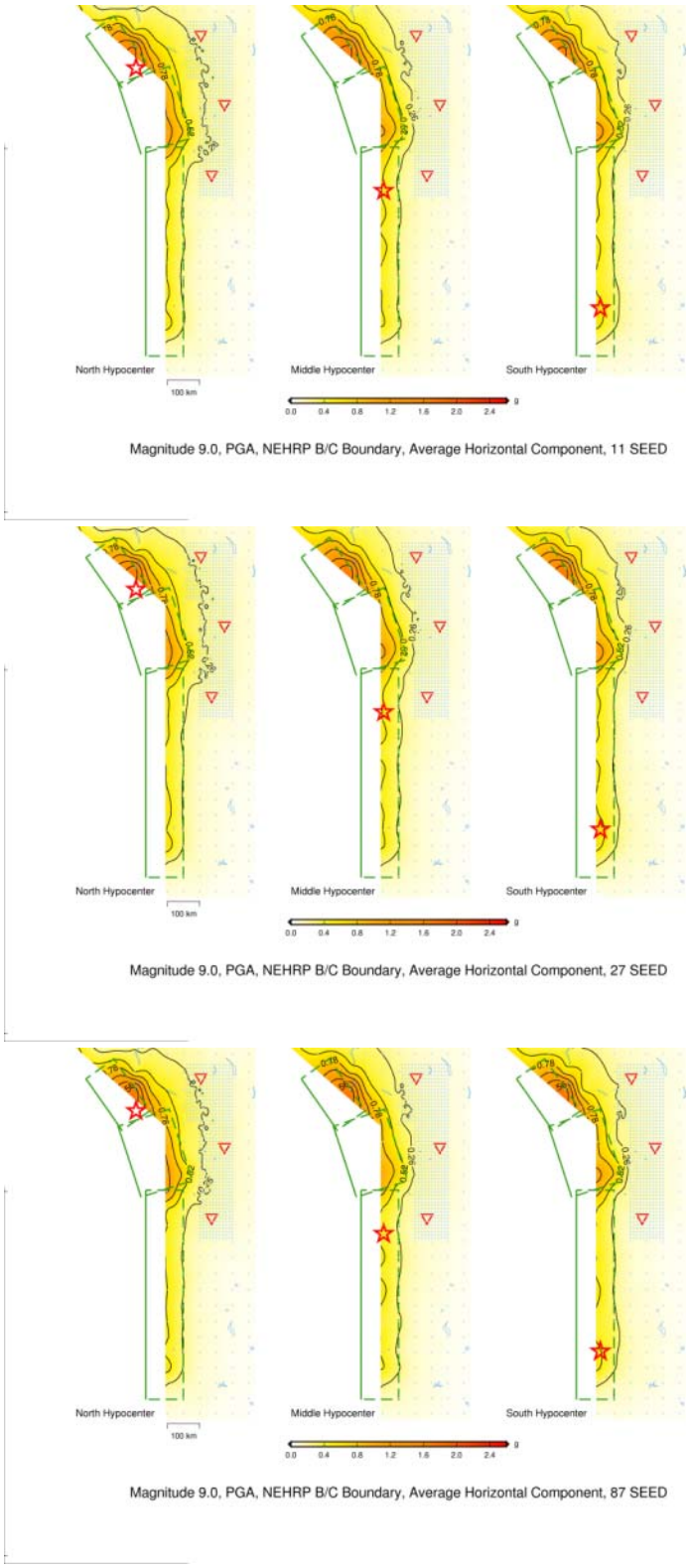

Figure 35. Ground motion maps for peak acceleration for an Mw 9.0 Cascadia earthquake for three hypocenter locations and various slip models, for NEHRP B/C boundary site conditions.

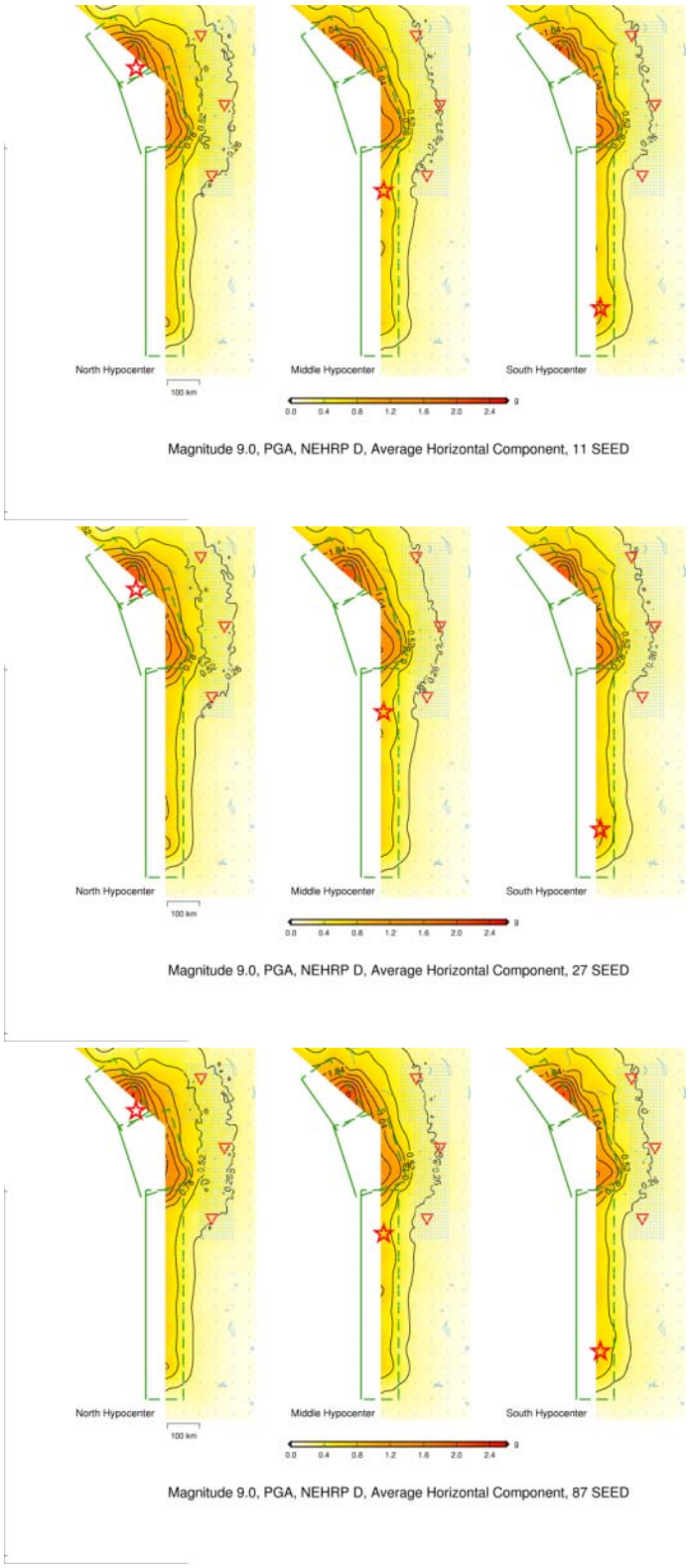

Figure 36. Ground motion maps for peak acceleration for an Mw 9.0 Cascadia earthquake for three hypocenter locations and various slip models, for NEHRP D site conditions.

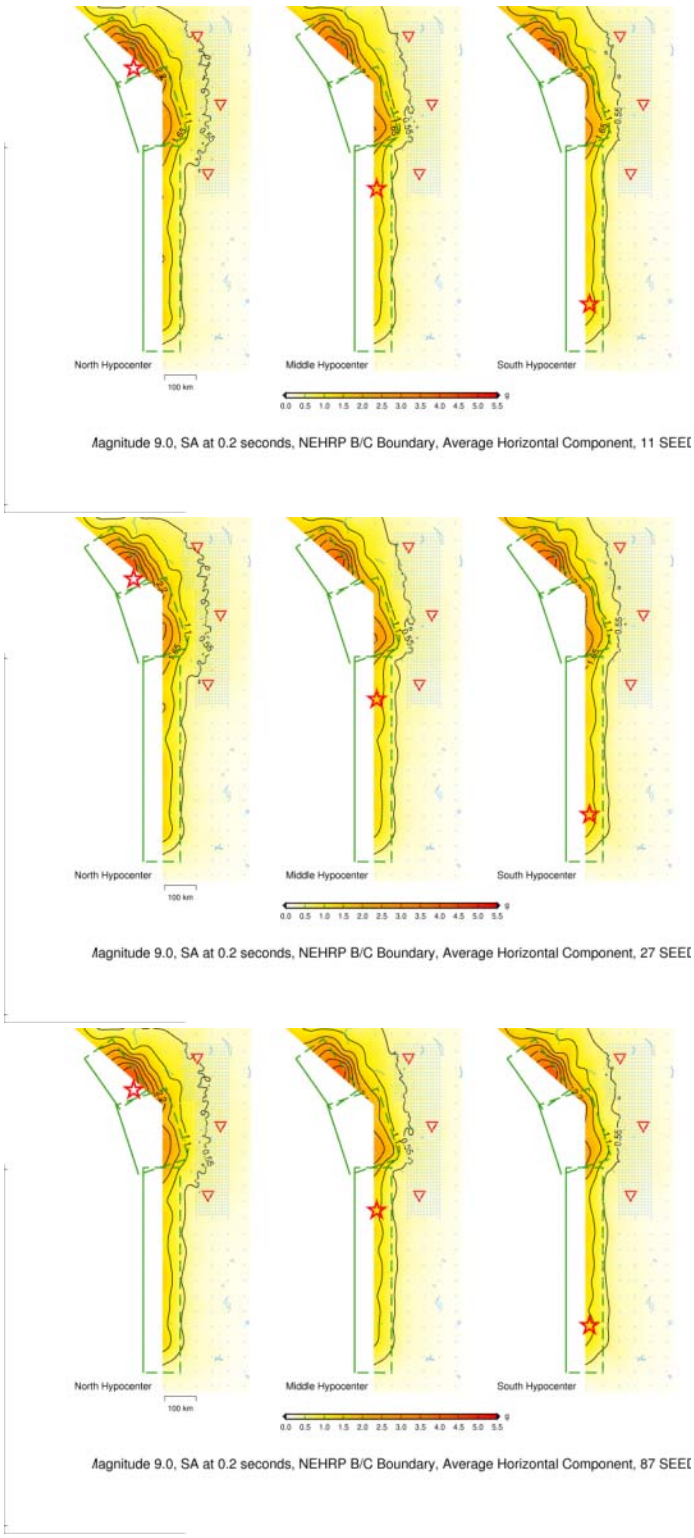

Figure 37. Ground motion maps for 0.2 s spectral acceleration for an Mw 9.0 Cascadia earthquake for three hypocenter locations and various slip models, for NEHRP B/C boundary site conditions.

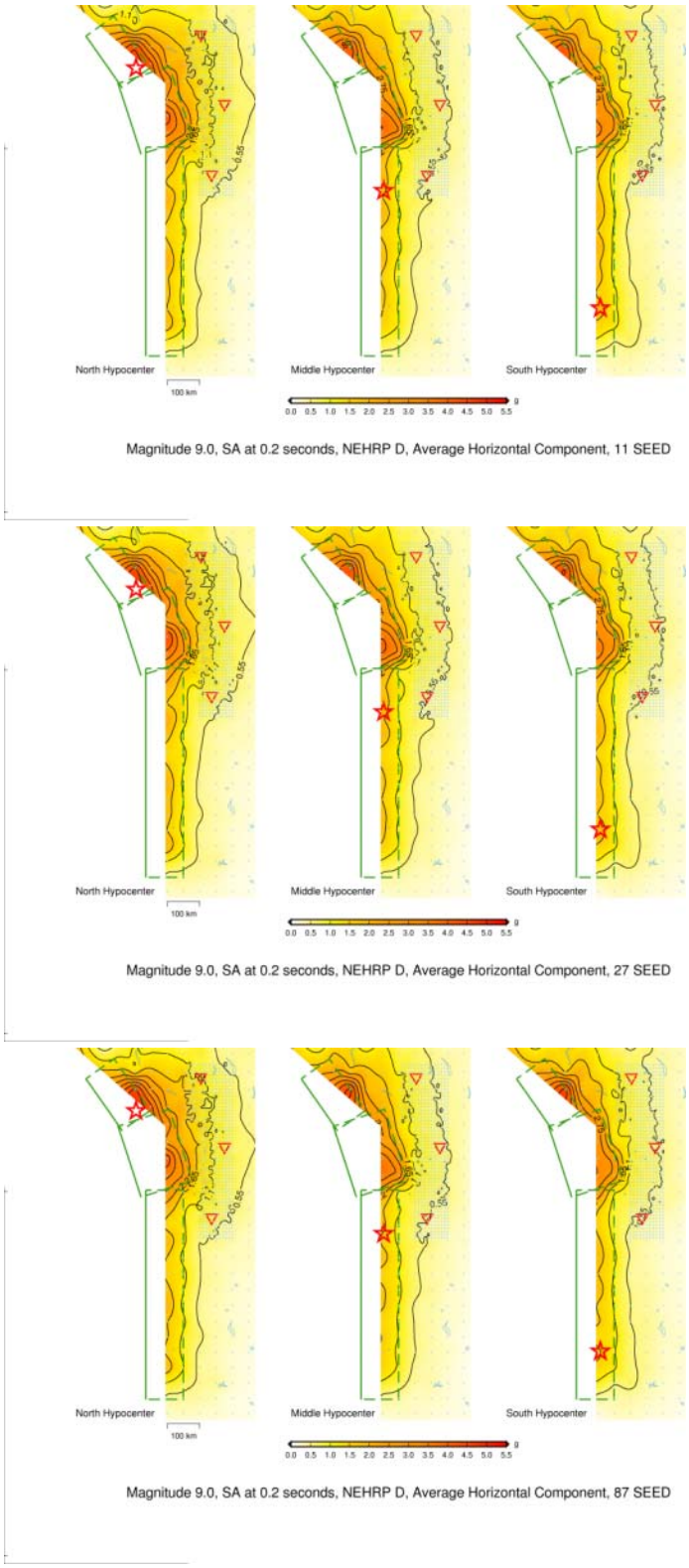

Figure 38. Ground motion maps for 0.2s spectral acceleration for an Mw 9.0 Cascadia earthquake for three hypocenter locations and various slip models, for NEHRP D site conditions.

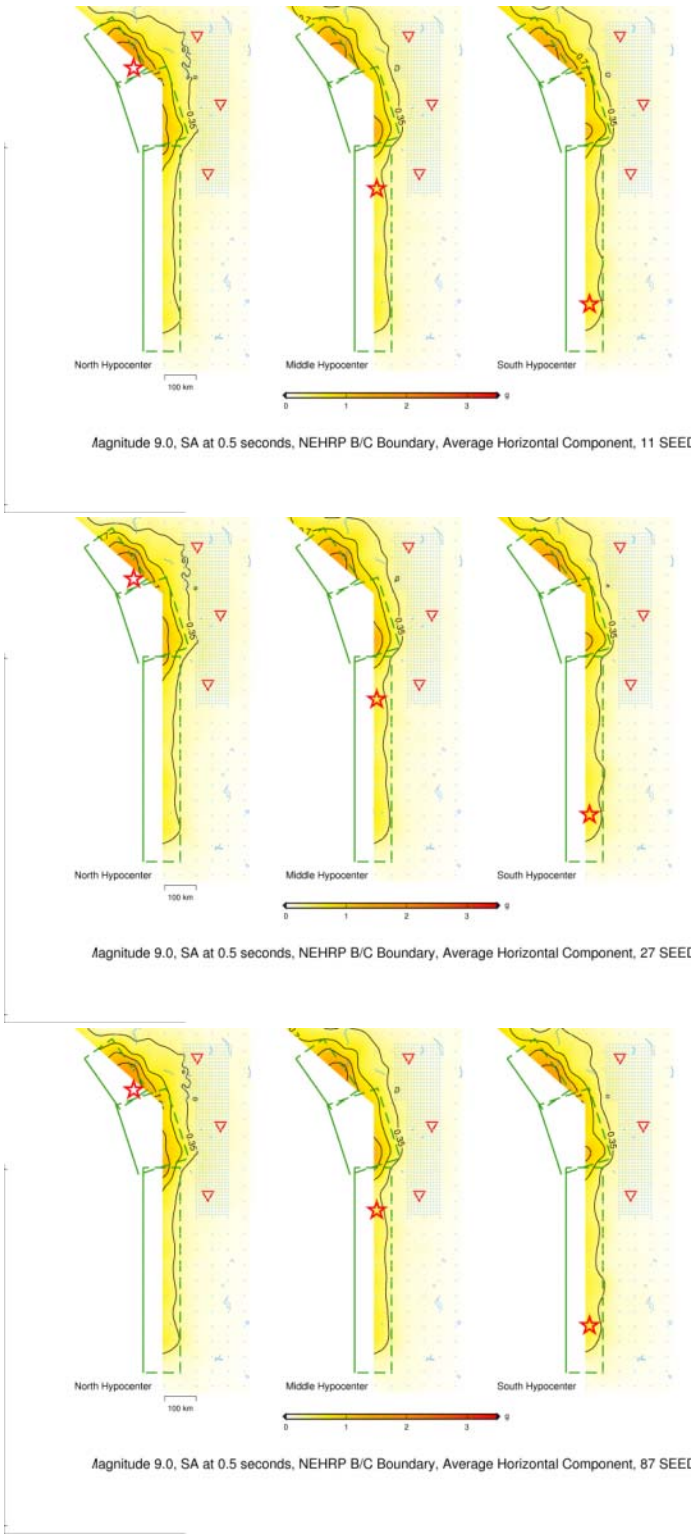

Figure 39. Ground motion maps for 0.5s spectral acceleration for an Mw 9.0 Cascadia earthquake for three hypocenter locations and various slip models, for NEHRP B/C boundary site conditions.

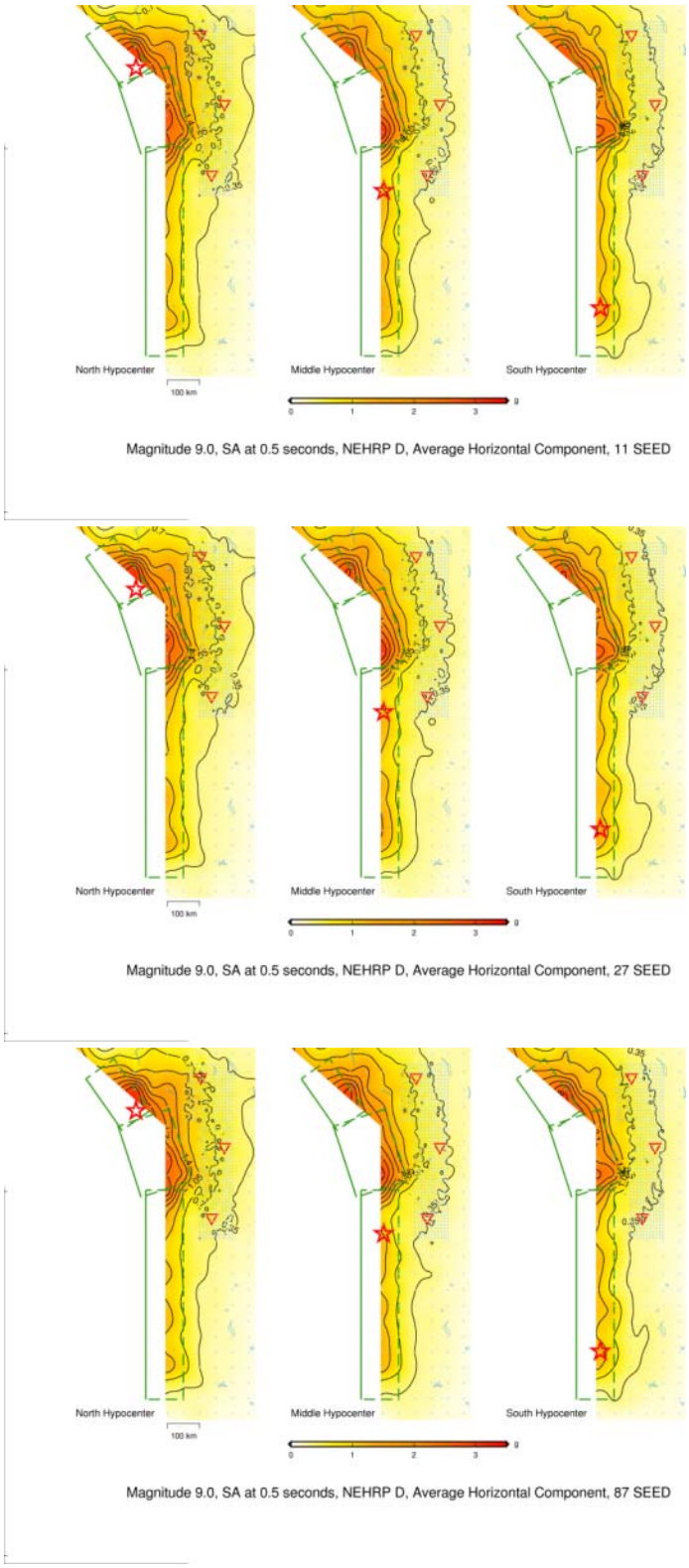

Figure 40. Ground motion maps for 0.5s spectral acceleration for an Mw 9.0 Cascadia earthquake for three hypocenter locations and various slip models, for NEHRP D site conditions.

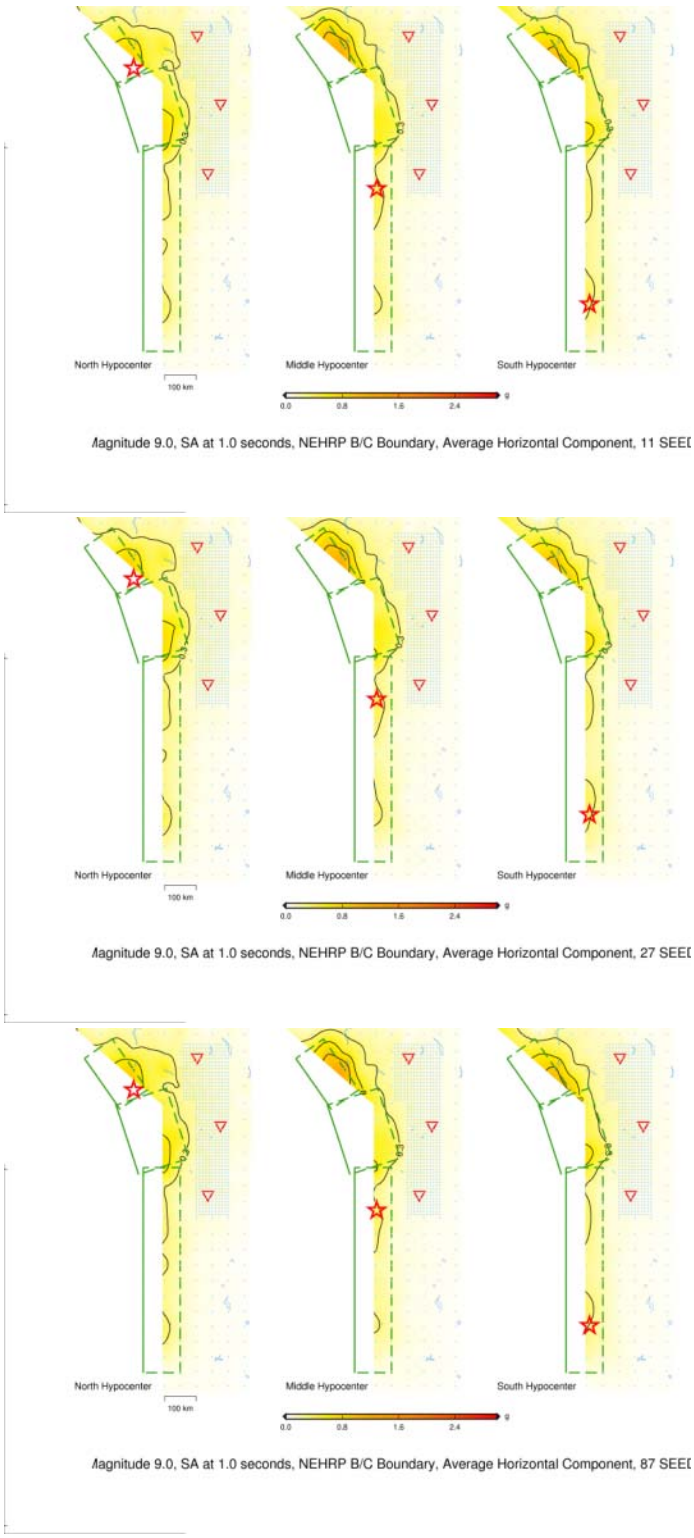

Figure 41. Ground motion maps for 1s spectral acceleration for an Mw 9.0 Cascadia earthquake for three hypocenter locations and various slip models, for NEHRP B/C boundary site conditions.

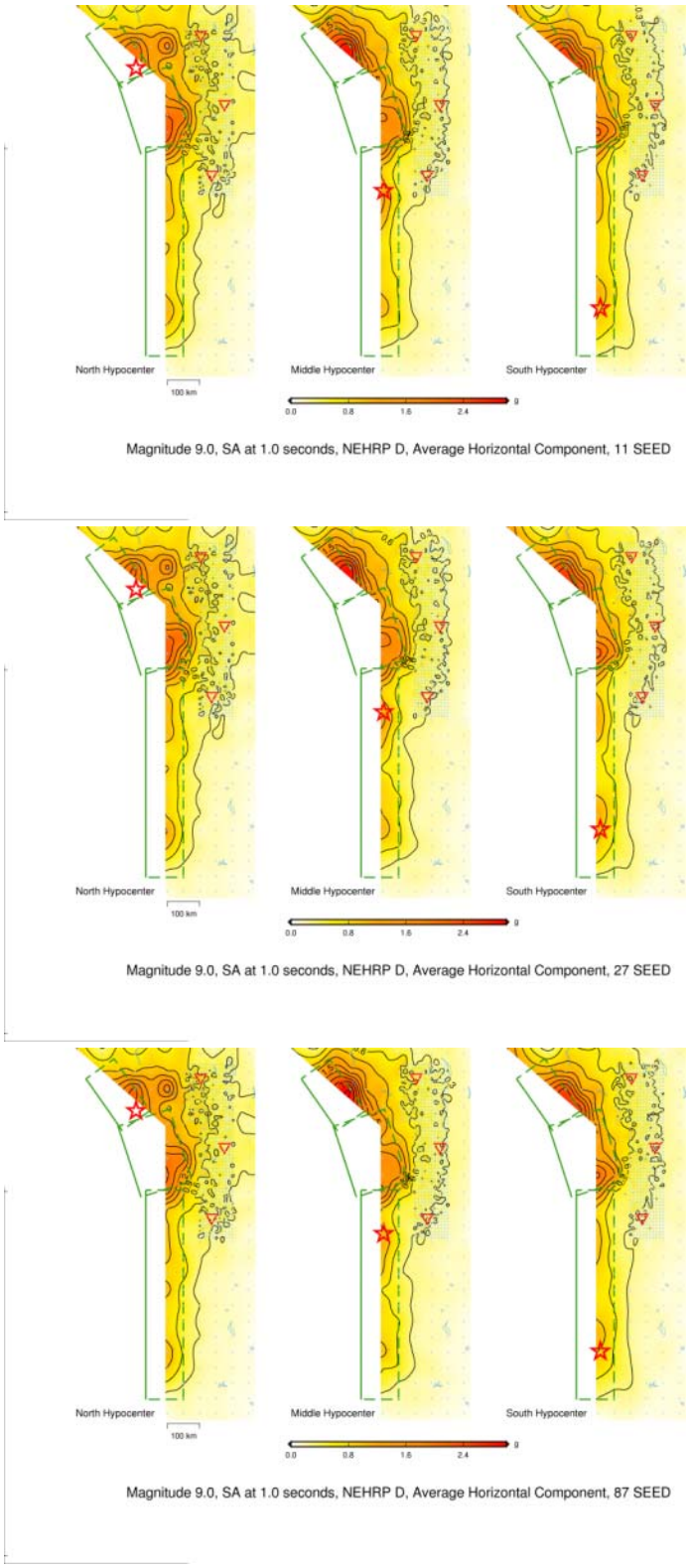

Figure 42. Ground motion maps for 1s spectral acceleration for an Mw 9.0 Cascadia earthquake for three hypocenter locations and various slip models, for NEHRP D site conditions.

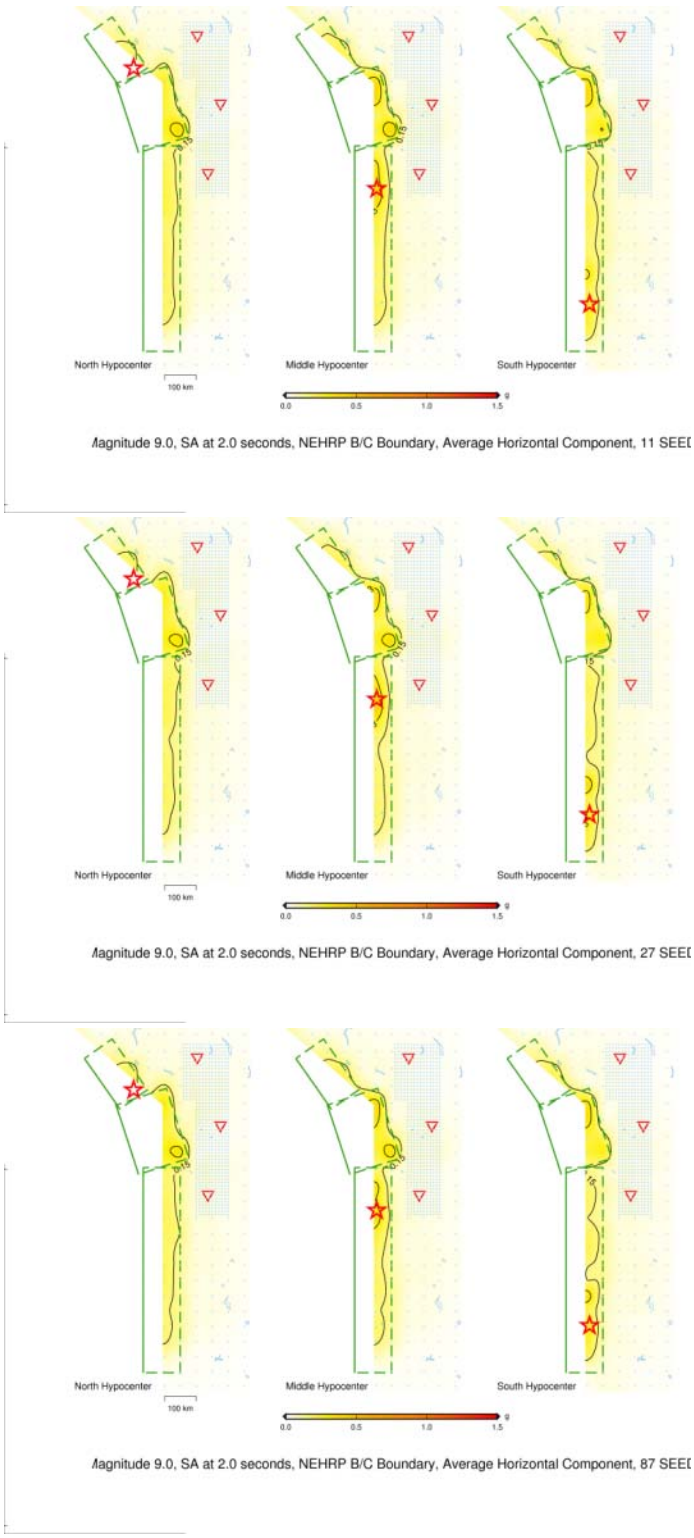

Figure 43. Ground motion maps for 2s spectral acceleration for an Mw 9.0 Cascadia earthquake for three hypocenter locations and various slip models, for NEHRP B/C boundary site conditions.

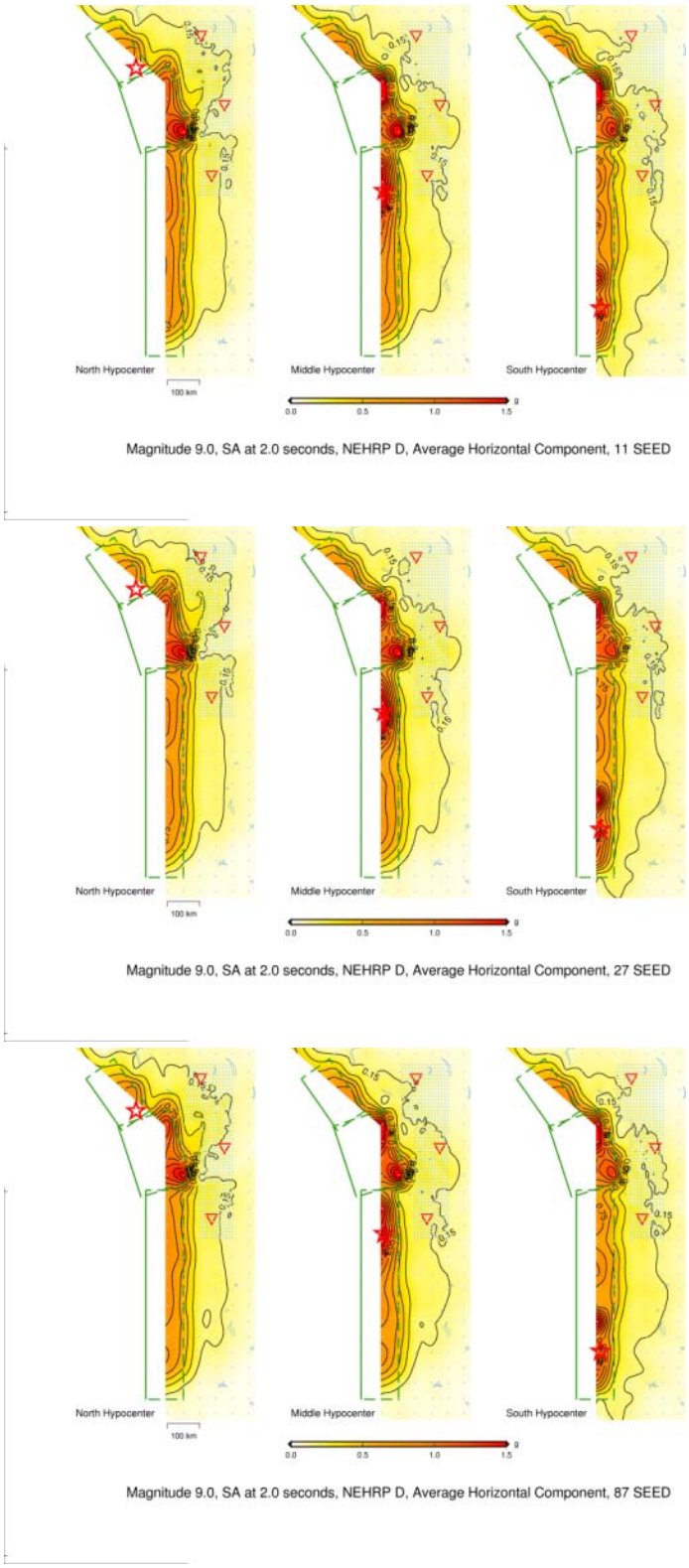

Figure 44. Ground motion maps for 2s spectral acceleration for an Mw 9.0 Cascadia earthquake for three hypocenter locations and various slip models, for NEHRP D site conditions.

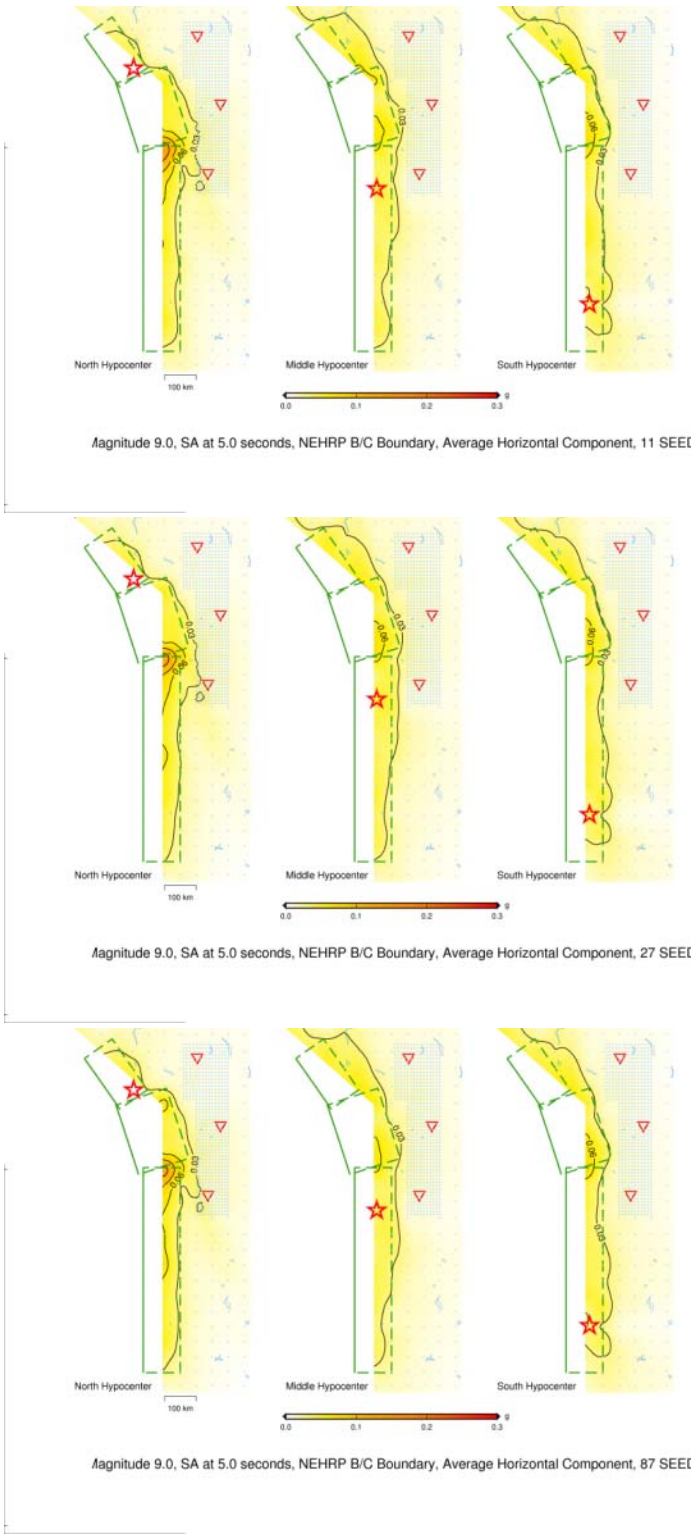

Figure 45. Ground motion maps for 5s spectral acceleration for an Mw 9.0 Cascadia earthquake for three hypocenter locations and various slip models, for NEHRP B/C boundary site conditions.

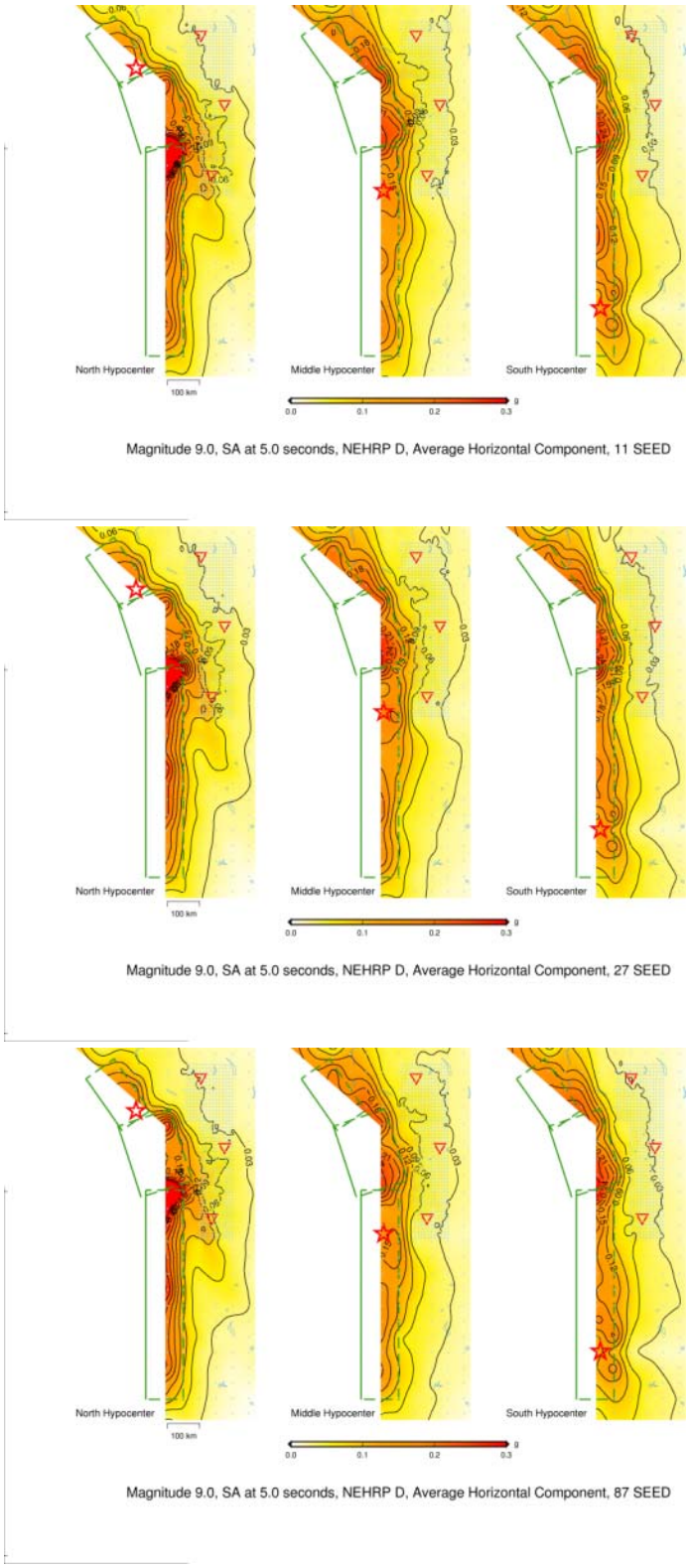

Figure 46. Ground motion maps for 5s spectral acceleration for an Mw 9.0 Cascadia earthquake for three hypocenter locations and various slip models, for NEHRP D site conditions.

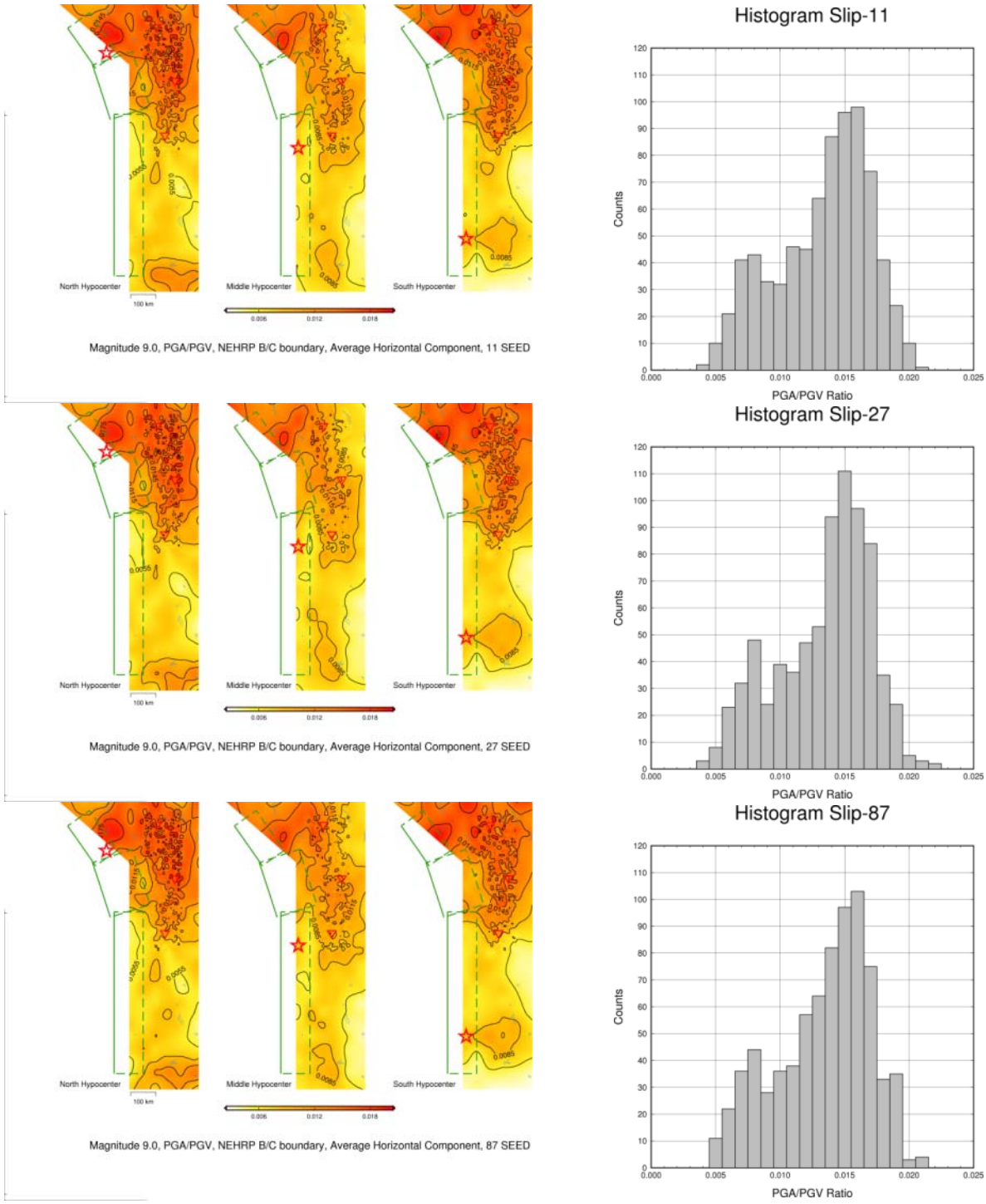

Figure 47. (Left) Spatial distribution of PGA/PGV ratios for the three slip models used in the simulations and for NEHRP B/C boundary site conditions. (Right) Histograms of the PGA/PGV ratio values for each slip model.

Propagation and Inundation Modeling of the 11 March 2011 Tohoku Tsunami

The tsunami triggered by the 11 March 2011 Mw 9.0 Tohoku earthquake was one of the most destructive tsunamis in human history. More than 2,000 km of coastline in East Japan was severely affected by the 2011 tsunami. Tsunami flooding occurred in most of the coastal region between latitudes 35°N and 41°N. The effect of the tsunami varied substantially from place to place depending on local terrain and coastal settings (Wei et al., 2012). Tsunami impact in the near field is more dependent on the source geometry than in the far field (Okal and Synolakis, 2004). The GeoClaw tsunami model is used in this study to predict the 11 March 2011 Japan tsunami transoceanic propagation and subsequent inundation of the northern Japanese coast.

GeoClaw is a branch of the open source software package, CLAWPACK (Conservation LAWs PACKage) which was first released by LeVeque in 1994 (http://www.clawpack.org). GeoClaw was originally named TsunamiClaw; the code has been further developed and improved for tsunami modeling over the years. GeoClaw was approved in 2012 by the US National Tsunami Hazard Mitigation Program (NHTMP) for use in modeling work.

The GeoClaw model solves the two-dimensional depth-averaged nonlinear shallow water equations using high-resolution finite volume methods:

$$h_t + (hu)_x + (hv)_y = 0$$

$$(hu)_t + \left(hu^2 + \frac{1}{2}gh^2\right)_x + (huv)_y = -ghB_x - Du$$

$$(hv)_t + (huv)_x + \left(hv^2 + \frac{1}{2}gh^2\right)_y = -ghB_y - Dv$$

where h is the water depth, u and v are the depth-averaged velocities in the horizontal directions, B is the bathymetry or topography, and D (h, u, v) is the drag coefficient. Values of h, hu and hv in each grid cell represent cell averages of the water depth and momentum components. The methods are exactly conservative for both mass and momentum with flat bathymetry; and conserve mass for arbitrary bathymetry when used on a fixed grid (González et al, 2011). This system of equations is widely used in modeling of tsunami propagation and inundation.

The high-resolution Godunov-type methods implemented in GeoClaw solve Riemann problems at each grid interface. Block structured adaptive mesh refinement (AMR) is used to employ much finer grid resolution in regions of particular interest. The empirical Manning formulation is used to model bottom friction; generally for generic tsunami modeling, the constant value of the Manning coefficient n = 0.025 is used. Also Coriolis terms can be turned on in the GeoClaw tsunami model.

Accurate high-resolution bathymetric and topographic data are crucial for evaluating tsunami wave dynamics in the coastal environment (Mofjeld et al., 2001). We have adopted the M7000 digital contoured bathymetric data (www.jha.or.jp) near the Japan coastal area. Figure 48 shows the M7000 digital bathymetric chart. The horizontal geodetic datum is the Word Geodetic System 84 (WGS-84) and the vertical datum is sea level. In this study we only focus on two sub-zones M7004 and M7005 delineated as black boxes in Figure 48. The original M7000 contoured data are converted to gridded data with a resolution of 1 arcsec to be used in the GeoClaw model. The GSI 10-m digital elevation models (DEMs) from http://www.gsi.go.jp/ provide us with high resolution topographic data, which are applied at the specific Japan coastal areas where we are interested in investigating tsunami inundation.

The horizontal geodetic datum is the Japanese Geodetic Datum 2000 (JGD2000) which has little difference from WGS84, and the vertical datum is sea level. The global bathymetric/topographic DEMs used over the Ocean are ETOPO1 with a resolution of 1 arcmin (~ 2 km); the horizontal datum is WGS84 and the vertical datum is sea level. The dataset is available online at the NOAA/NGDC website.

A bathymetric and topographic dataset compiled by combining ETOPO1 1 arcmin bathymetry, M7000 series, and the GSI 10-m DEMs is used to develop all the model grids implemented in the GeoClaw tsunami model with datasets referenced to mean sea level. Since the vertical resolution of the GSI topographic data is about 1 m and the tidal variation along the east coast of Japan is less than 0.5 m, the tidal level is set at sea level.

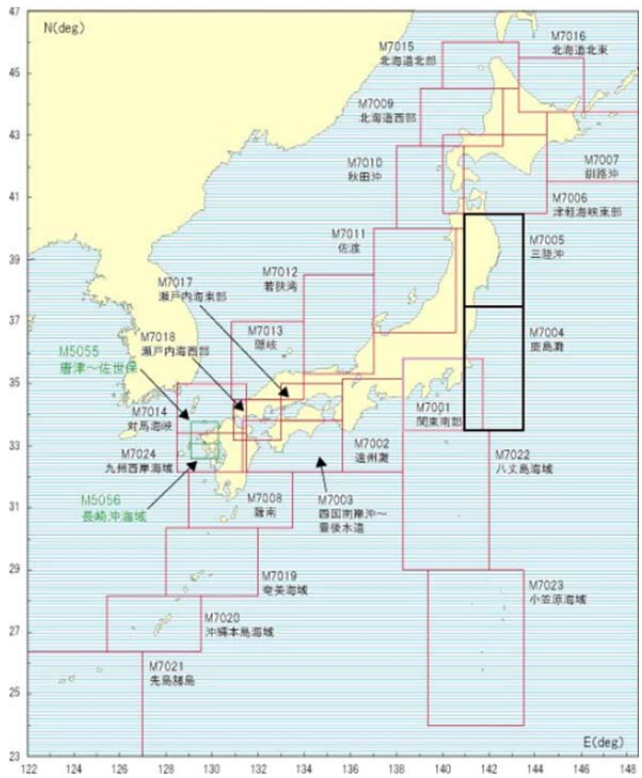

Figure 48. The M7000 digital bathymetric chart: the black boxes delineate M7004 and M7005.

The local topography data are 10m-DEM from http://www.gsi.go.jp/. This data is applied to the coastal area where tsunami inundation needed to be investigated. The horizontal datum used in this dataset is JGD2000, which has very little difference from WGS84 in Japan, so there is no need for horizontal coordinate correction when used together with M7000 Digital Bathymetric Chart. The vertical datum is sea level.

The tsunami source models used in this study are based on the slip distributions from Yokota et al. (2011). The slip distributions were derived from the results of separate inversions of the strong motion, teleseismic, geodetic, and tsunami datasets, respectively. In order to overcome the limited resolution of the separate inversions and the differences in the results of these inversions, Yokota et al carried out a quadruple joint inversion of these four datasets by using the same method as that for the separate

inversions. Here we selected three kinds of tsunami source models derived from the separate inversions of the geodetic and tsunami datasets, and the joint inversion. As the initial condition for tsunami, static deformation of the seafloor is calculated from elasticity theory for a rectangular fault model (Okada, 1985). The Okada model is often used to translate slip along one small fault plane into the seafloor motion; the final displacement is achieved by combining the seafloor motions caused by the 96 small sub-faults.

We applied the GeoClaw Tsunami model to simulate the tsunami propagation and inundation along the east coast of Japan using the instantaneous tsunami sources. Figure 49 shows the vertical seafloor deformation of the 11 March 2011 Japan tsunami sources inferred from the results of the separate inversions of geodetic and tsunami datasets and the joint inversion. In this near-field study, the target site of interest covers part of the coastline in the two prefecture areas of Miyagi and Iwate, as well as Fukushima I /II Nuclear Power Plants (see Figure 50-right).

The computational domain of this GeoClaw tsunami model is (135°E, 155°E) in longitude and (25°N, 49°N) in latitude (see Figure 50-left). The zero-order extrapolation from grid cells along the boundaries to ghost cells in every time step is used to implement non-reflecting boundary conditions at the four edges of the computational domain. The total computational time is 5 hours. The Manning coefficient *n* = 0.025 is used in the friction term and the Coriolis terms are turned on in the calculations. The grid refinement levels used in the GeoClaw model are 4 arcmin, 1 arcmin, 15 arcsec, 5 arcsec and 1 arcsec (4 arcmin, 1 arcmin, 12 arcsec, 4 arcsec and 0.4 arcsec for the two Fukushima Nuclear Power Plants). All model zones share common grids over the continental shelf of East Japan at the resolution of 4 arcmin (~ 7.2 km) and 1 arcmin (~ 1.8 km); intermediate grids are used at regional scales; inner grids of 1 or 0.4 arcsec (~ 30 m or 12 m) are used for computing tsunami inundation at specific coastlines. The tsunami source is calculated within the region of (140°E, 145°E) (35°N, 41°N) with a resolution of 1 arcmin.

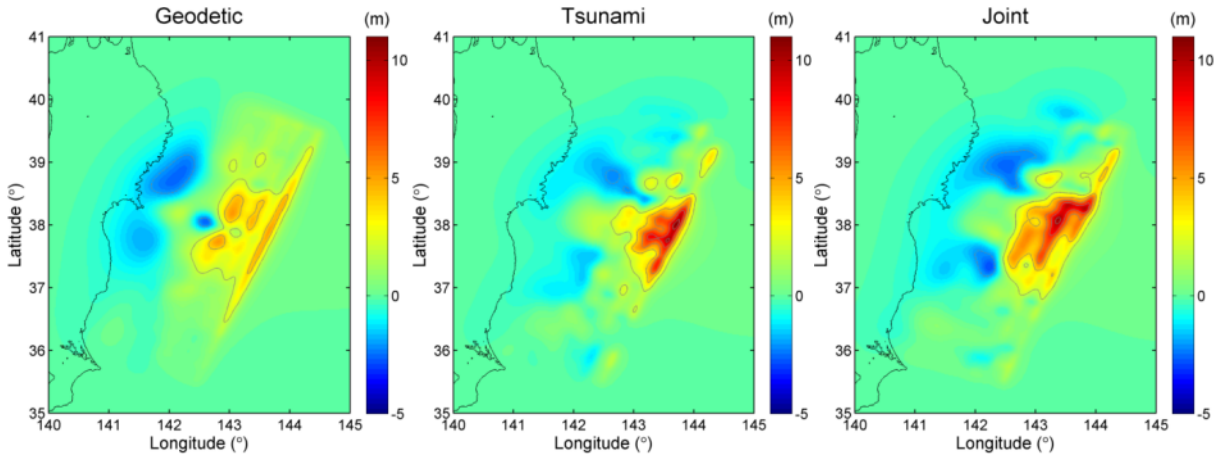

Figure 49. Static seafloor deformation for the three different tsunami source models (slip distributions) determined by the results of two separate inversions of geodetic and tsunami datasets and the joint inversion. The colors indicate the magnitude of the seafloor displacement.

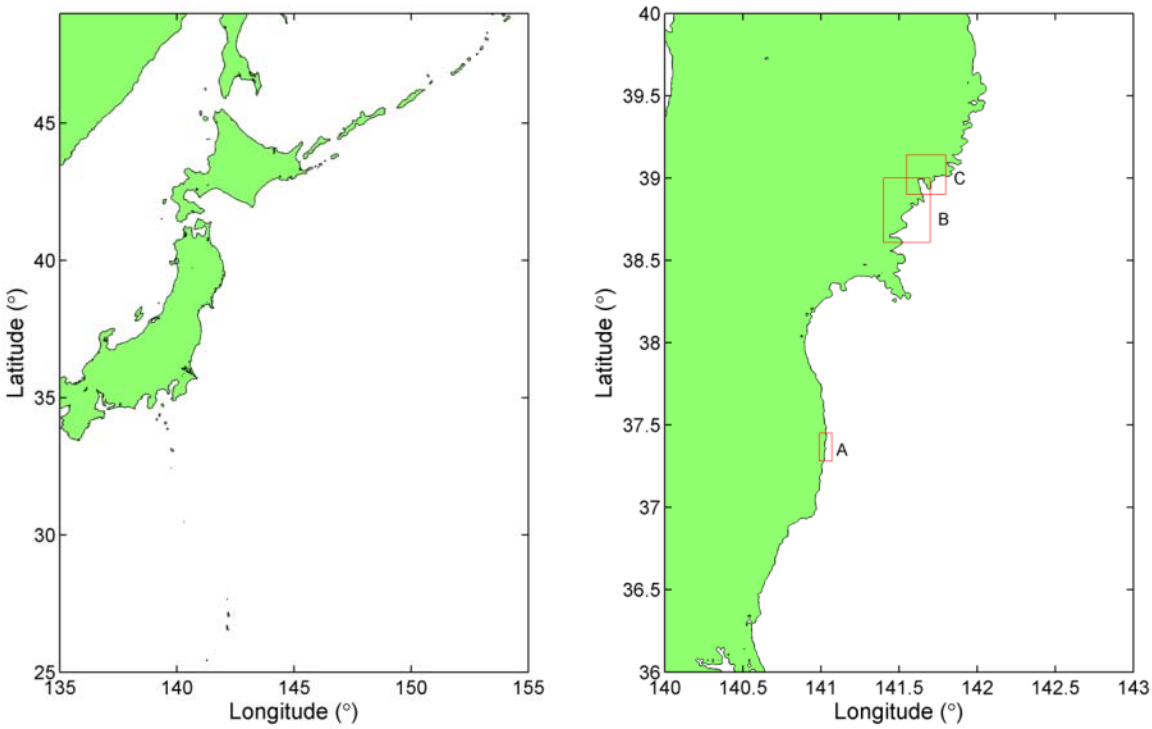

Figure 50. Left: computational domain of the GeoClaw tsunami inundation model; right: layout of the target areas of interest A, B and C (red boxes).

The GeoClaw-computed tsunami inundation maps at the areas of interest are presented in Figures 51 – 53. The magenta solid line indicates the observed extent of tsunami inundation (http://www.jsgi-map.org/tsunami/). There are no surveyed extents of inundation at the area around the two Fukushima nuclear power plants. Here the tsunami inundation depth ζ represents the maximum value over the full time period of a tsunami of either the flow depth at points on land or the sea surface elevation relative to sea level for points offshore. The tidal level is set at sea level. The maximum value of tsunami inundation depth ζ_{max} at each target area from each source model is marked on each inundation map.

Figures 52 and 53 show that the model predicted results are in good agreement with the surveyed extents of tsunami inundation at those areas of interest, and the results using the tsunami source model derived from the joint inversion give the best agreement. Furthermore, the computed inundation maps in Figures 52 – 53 demonstrate that the tsunami source scenario derived from the joint inversion gives the maximum inundation height compared to the other two source scenarios from the separate inversions of geodetic and tsunami datasets.

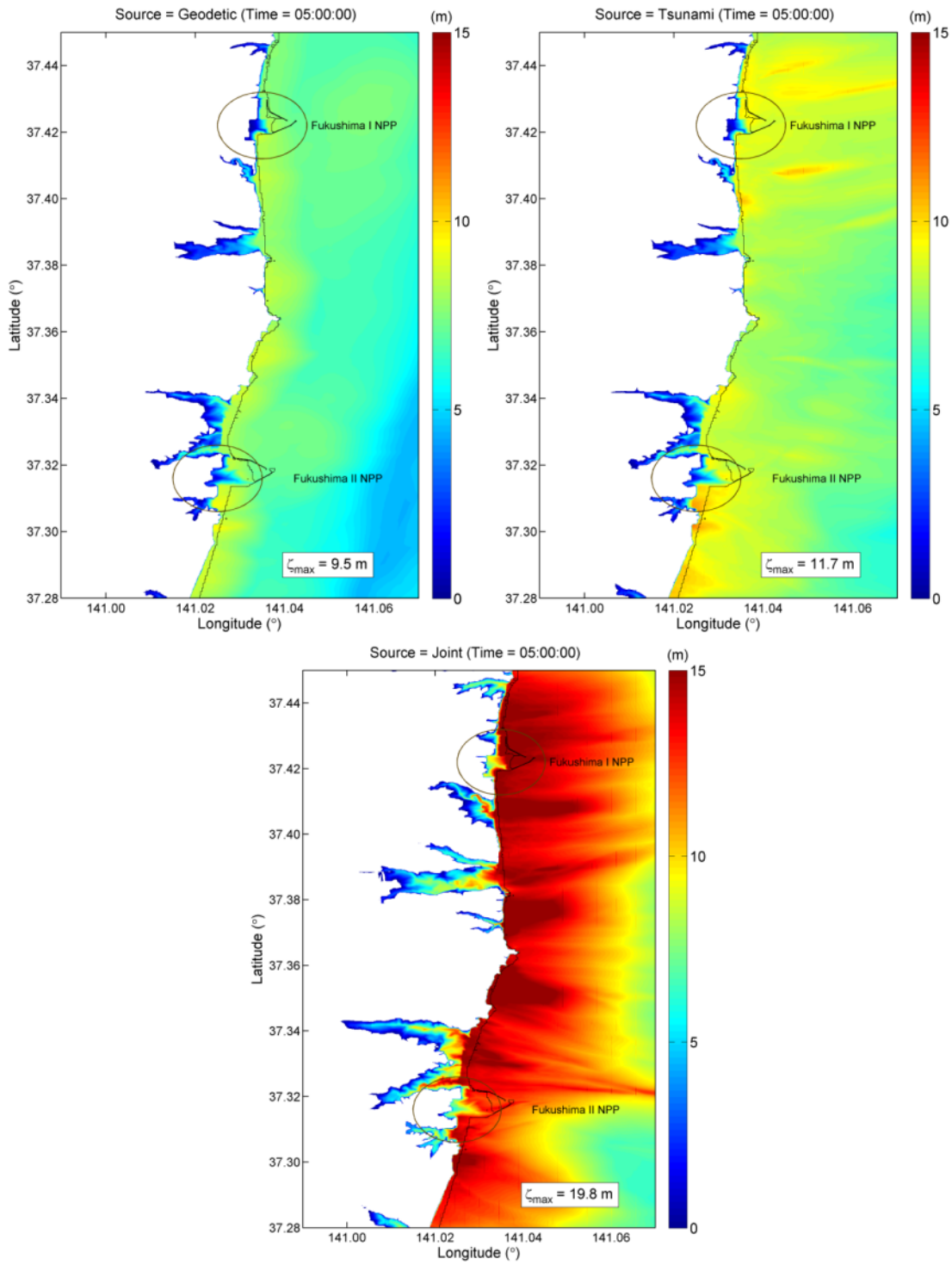

Figure 51. GeoClaw-computed tsunami inundation maps at the areas of Fukushima I/II nuclear power plants (A) with three different source models derived from the separate inversions of geodetic and tsunami datasets and the joint inversion, respectively. The color represents the computed inundation depth ζ, and the black solid line represents the shoreline.

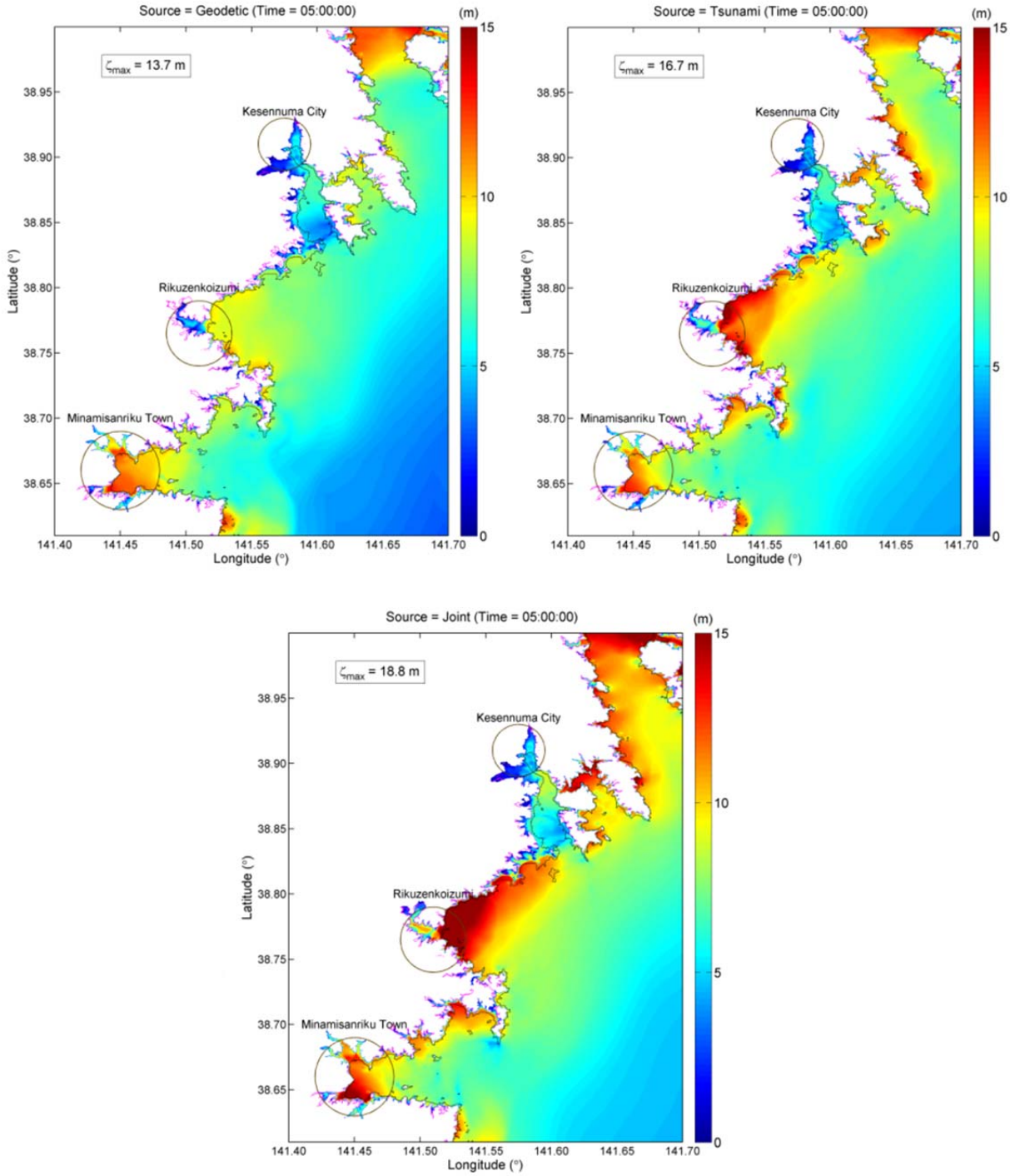

Figure 52. Observed and GeoClaw-computed tsunami inundation in the areas of Minamisanriku Town, Rikuzenkoizumi and Kessennuma City (B) with three different source models derived from the separate inversions of geodetic and tsunami datasets and the joint inversion, respectively. The magenta line indicates the observed extent of tsunami inundation; the color represents the computed inundation depth ζ; the black solid line represents the shoreline.

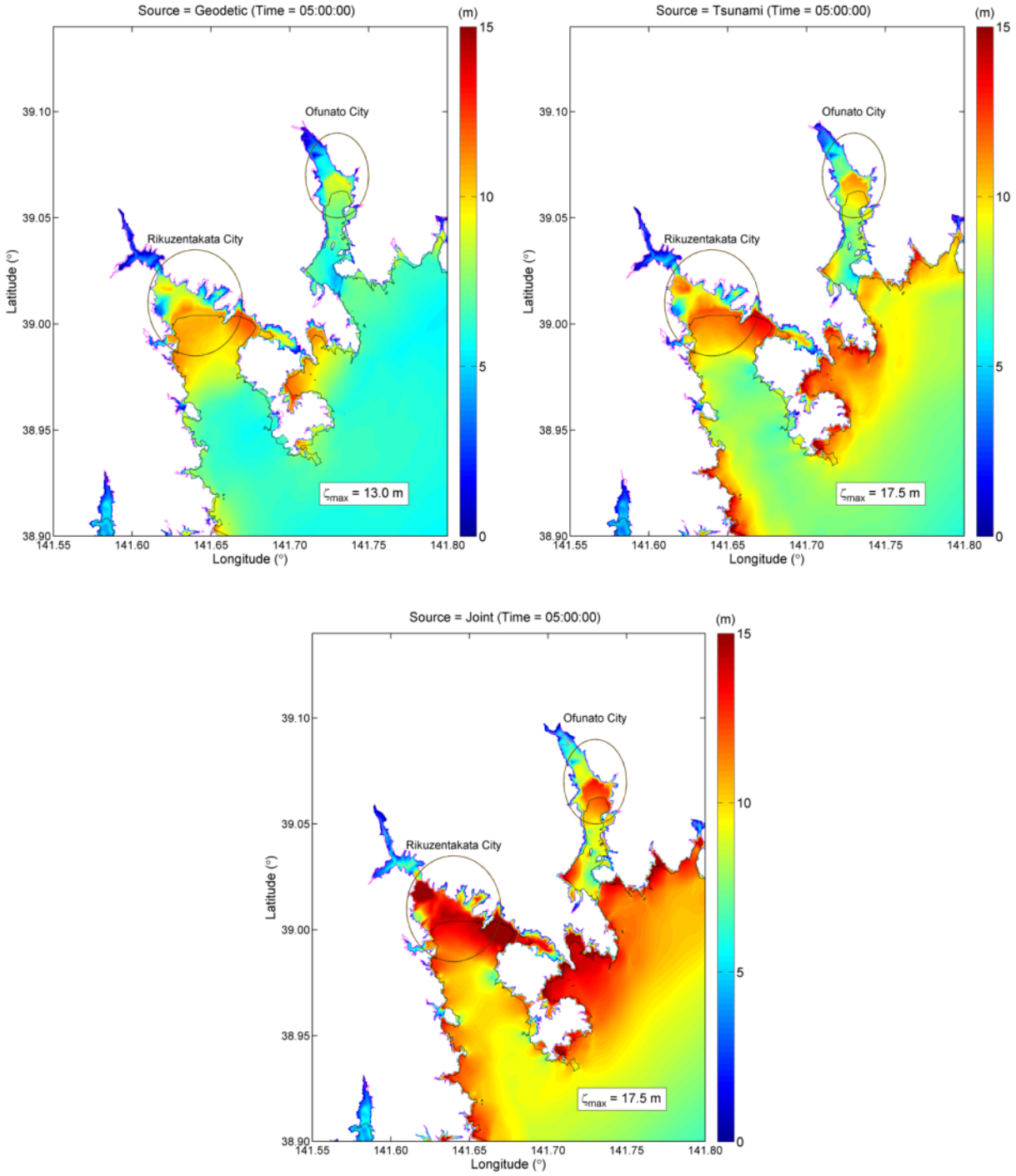

Figure 53. Observed and GeoClaw-computed tsunami inundation in the areas of Rikuzentakata City and Ofunato City (C) with three different source models derived from the separate inversions of geodetic and tsunami datasets and the joint inversion, respectively. The magenta line indicates the observed extent of tsunami inundation; the color represents the computed inundation depth ζ; the black solid line represents the shoreline.

Tsunami Modeling of Mw 9.0 Cascadia Subduction Earthquake Scenarios

The GeoClaw model is used here to simulate tsunami propagation and inundation of several Mw 9.0 Cascadia subduction scenario earthquakes. We chose the slip models 11, 27 and 87 as the tsunami sources. The static seafloor deformation is calculated using the Okada (1985) Model within the region of (129°W, 122°W) (39°N, 51°N) with a resolution of 1 arcmin. Figure 54 shows the seafloor deformation for these three slip models. Since instantaneous tsunami sources are used in the GeoClaw model, only the final seafloor displacement matters. Thus, different earthquake hypocentral locations for the same slip model have no effect on the tsunami simulations.

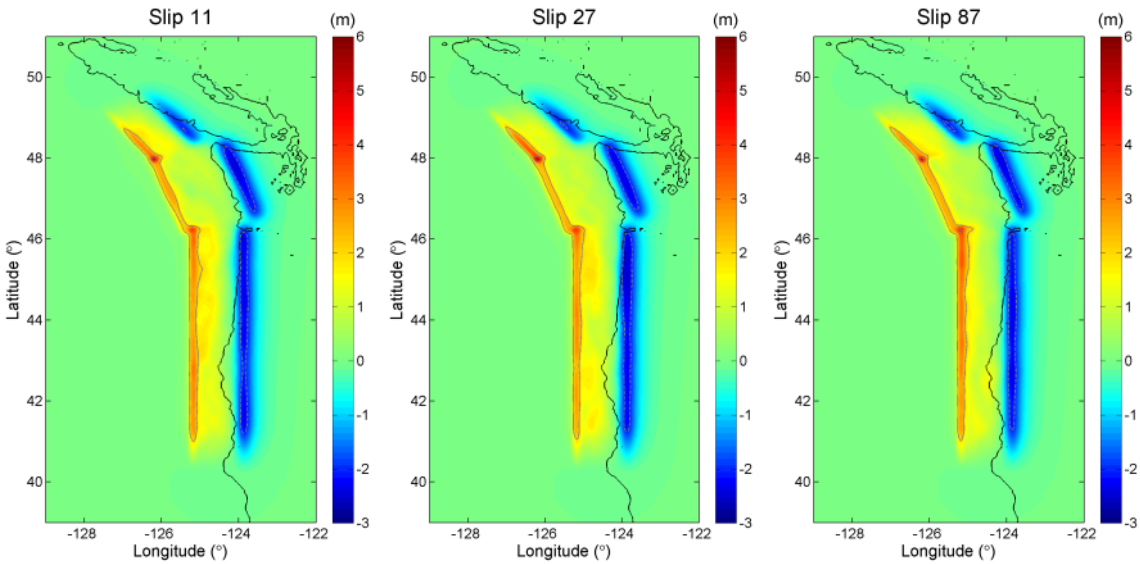

Figure 54. Static seafloor deformation for the three different Cascasdia tsunami source models (slip models 11, 27 and 87). The colors indicate the magnitude of the seafloor displacement.

The target areas of interest for this Cascadia tsunami inundation model are Crescent City, CA; Klamath River, CA; Redwood Creek, CA; Seaside, OR. The bathymetric and topographic dataset is compiled using ETOPO1 1 arcmin (~ 1.8 km) grids, 3 arcsec (~ 90 m) DEMs and 1/3 arcsec (~ 10 m) DEMs referenced to Mean High Water (MHW), which are all available at the NOAA/NGDC website.

The Computational domain of this GeoClaw tsunami model is (150°W, 115°W) in longitude and (30°N, 55°N) in latitude. The total computational time is 4 hours. The Manning coefficient n = 0.025 is used in the friction term and the Coriolis terms are turned on in the model. The grid refinement levels used in this tsunami propagation and inundation model are 4 arcmin, 1 arcmin, 15 arcsec, 3 arcsec and 1 arcsec (~ 30 m).

Figures 55 – 58 present the GeoClaw-predicted tsunami inundation around the four target areas using the selected slip models 11, 27 and 87. The inundation depth ζ is defined the same as in the last section. The maximum value of tsunami inundation depth ζ_{max} in each target area from every slip model is marked on each inundation map. The tidal level is set at MHW. The results demonstrate that the model-computed tsunami inundations from the three slip models have similar characteristics, and the slip model 27 generates the lowest inundation depth ζ in the four target areas. Generally, the target

area around Seaside, OR has relatively larger tsunami inundation since it is closer to the center of the Cascadia tsunami source; and the area around Redwood Creek, CA has relatively lower inundation depth because it is near the southern end of the tsunami source. These scenario results are very similar top those that we generated using source models based on the 2010 Maule, Chile earthquake (Somerville et al., 2013).

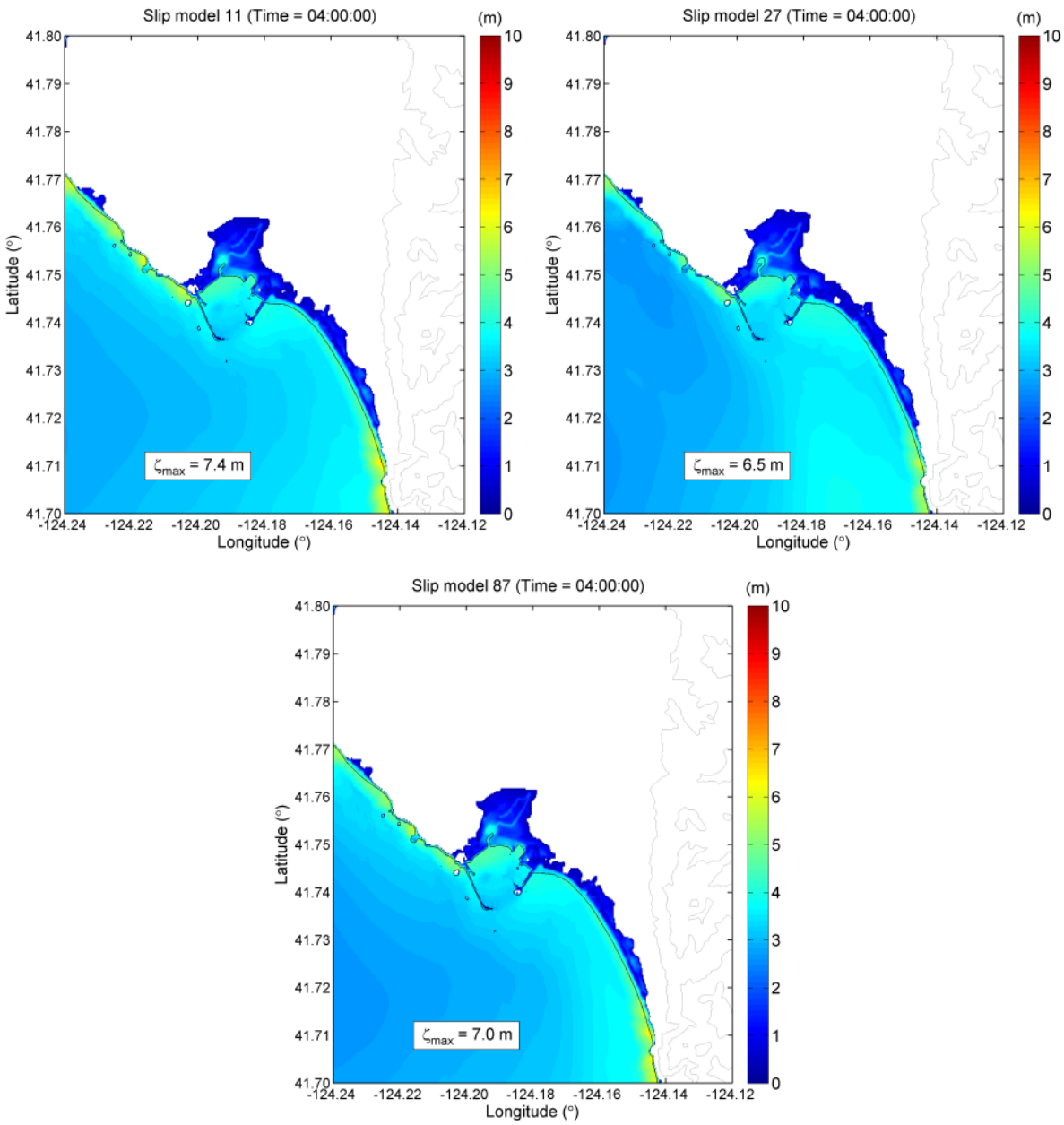

Figure 55. GeoClaw-computed tsunami inundation around Crescent City, CA from the Mw 9.0 Cascadia slip models 11, 27 and 87. The color represents the computed inundation depth ζ; the black line represents the shoreline. The grey lines denote the topographic contours every 100 m.

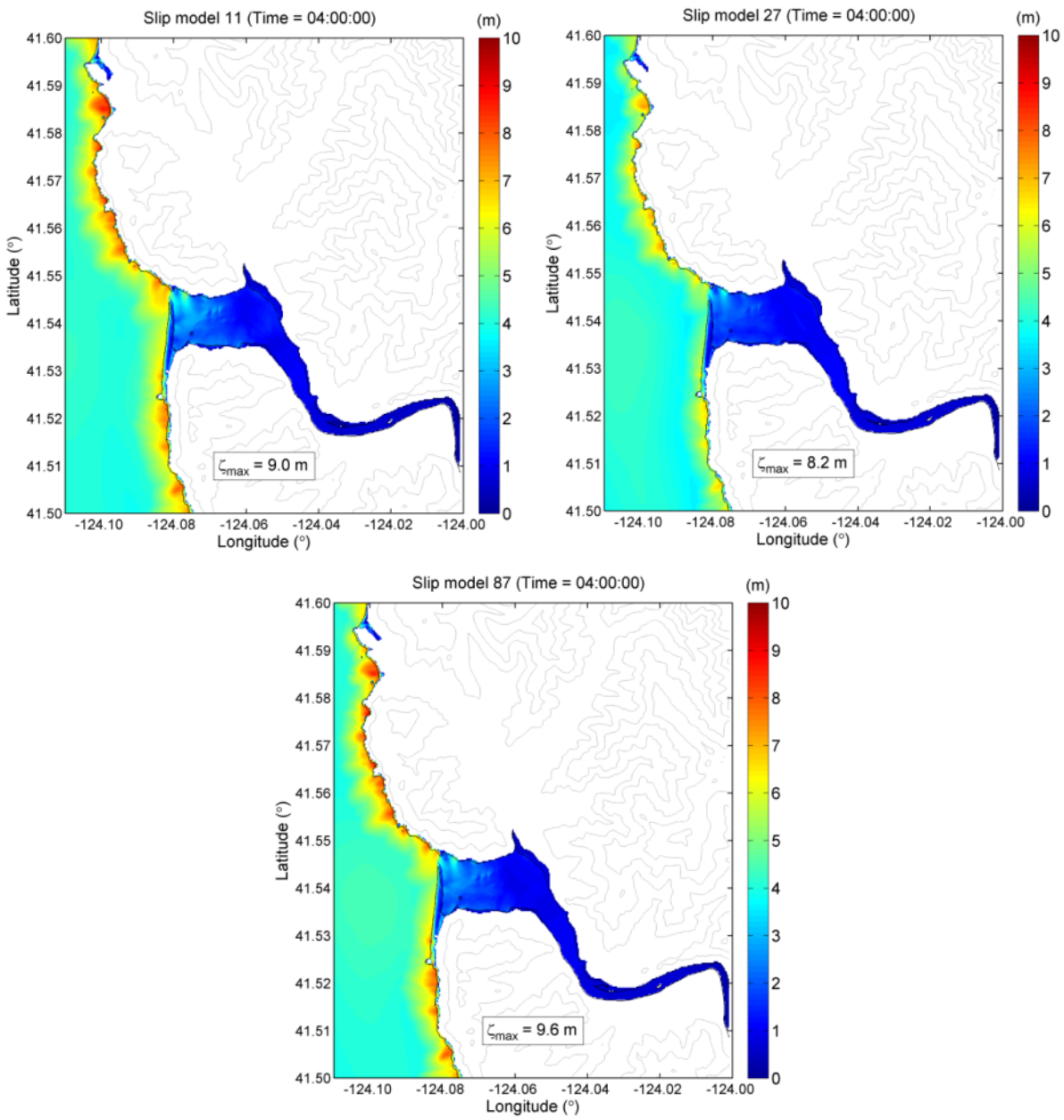

Figure 56. GeoClaw-computed tsunami inundation around Klamath River, CA from the Mw 9.0 Cascadia slip models 11, 27 and 87. The color represents the computed inundation depth ζ; the black line represents the shoreline. The grey lines denote the topographic contours every 100 m.

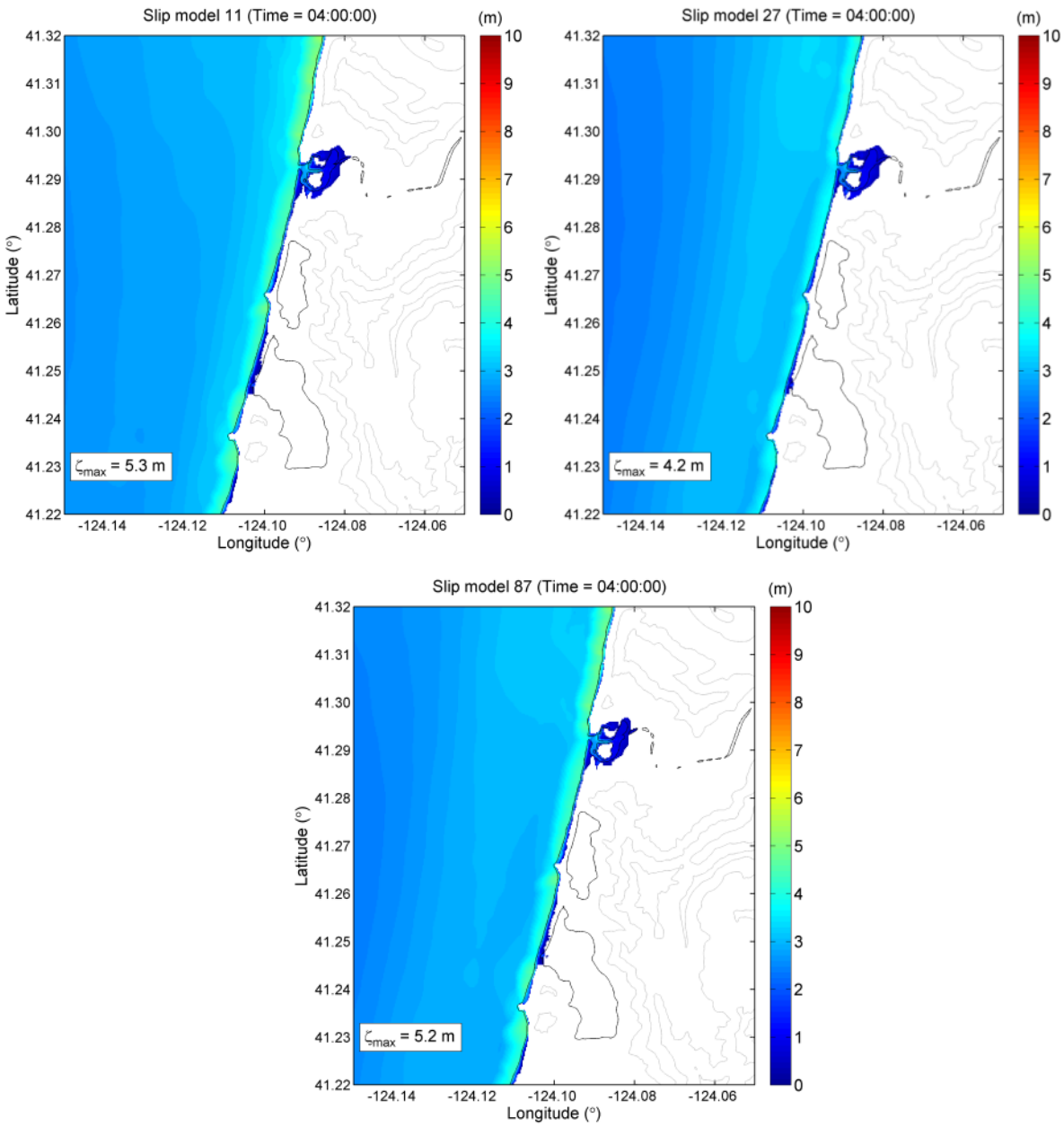

Figure 57. GeoClaw-computed tsunami inundation around Redwood Creek, CA from the Mw9.0 Cascadia slip models 11, 27 and 87. The color represents the computed inundation depth ζ; the black line represents the shoreline. The grey lines denote the topographic contours every 100 m.

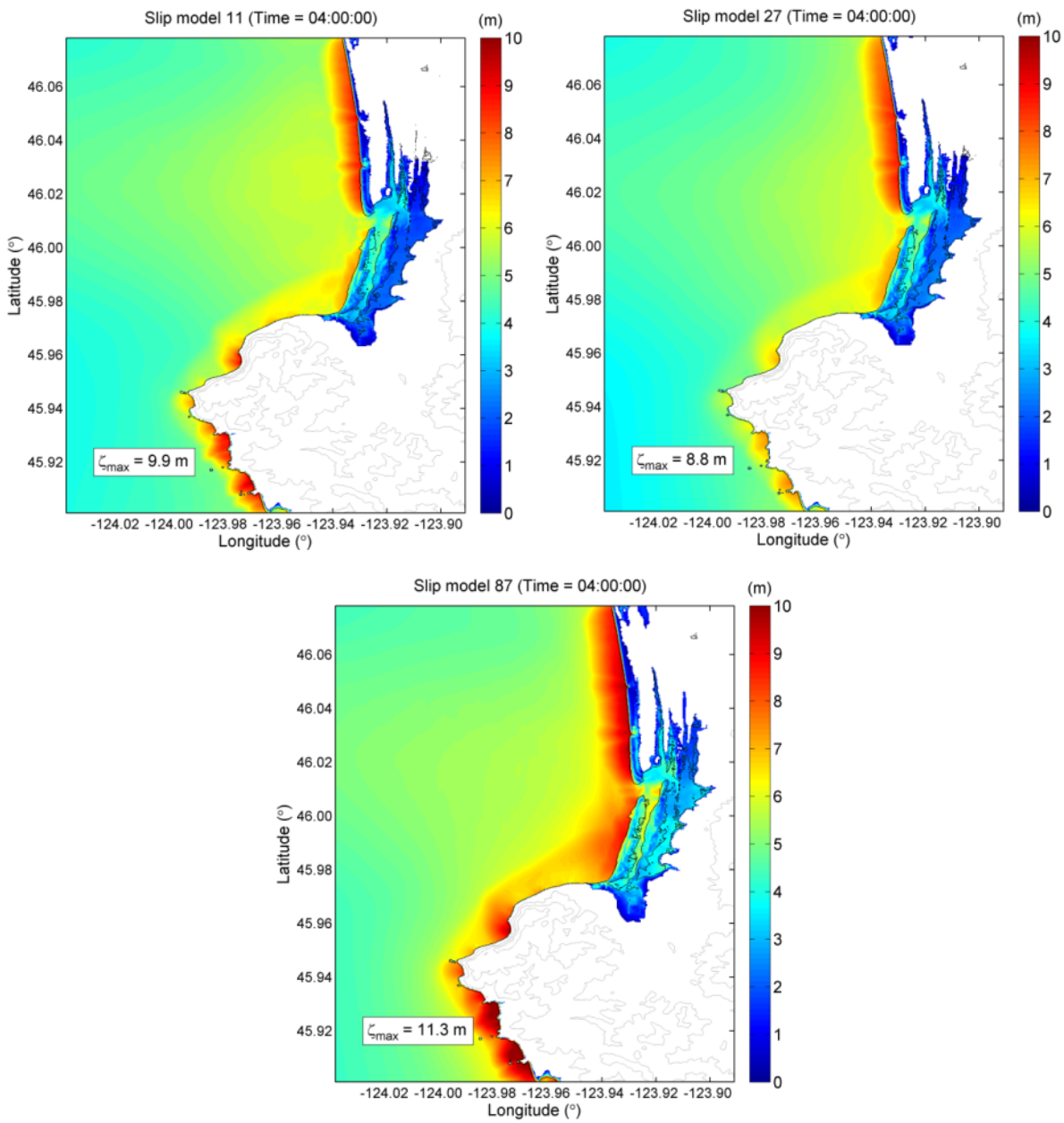

Figure 58. GeoClaw-computed tsunami inundation around Seaside, OR from the Mw 9.0 Cascadia slip models 11, 27 and 87. The color represents the computed inundation depth ζ; the black line represents the shoreline. The grey lines denote the topographic contours every 100 m.

References

Abrahamson, N., N. Gregor and K. Addo (2012). BC Hydro Ground Motion Prediction Equations for Subduction Earthquakes. *Earthquake Spectra, submitted*.

Abrahamson, N.A., P.G. Somerville, and C. Allin Cornell (1990). Uncertainty in numerical strong motion predictions, *Proc. 4th U.S. National Conference on Earthquake Engineering,* **1**, 407- 416.

Atkinson, G.M. and D.M. Boore (2003). Empirical ground motion relations for subduction zone earthquakes and their application to Cascadia and other regions, *Bull. Seism. Soc. Am*. **93**, 1703-1729.

Boore D.M., J.P. Stewart, E. Seyhan, and G.M. Atkinson (2013). NGA-West2 Equations for Predicting Response Spectral Accelerations for Shallow Crustal Earthquakes, PEER Report, May 2013, 135pp.

Brocher, T.M., T. Parsons, A. Trehu, C.M. Snelson, and M.A. Fisher (2003). Seismic evidence for widespread serpentinized forearc upper mantle along the Cascadia margin. *Geology* 31, 267-270.

Clowes, R.M., M.T. Brandon, A.G. Green, C.J. Yorath, A.S. Brown, E.R. Kanasewich, and C. Spencer (1987). LITHOPROBE – southern Vancouver Island: Cenozoic subduction complex imaged by deep seismic reflections. *Can. J. Earth Sci.* 24, 31-51.

Cohee, B.P., P.G. Somerville and N.A. Abrahamson (1991). Ground motions from hypothesized Mw = 8 subduction earthquakes in the Pacific Northwest, *Bull. Seism. Soc. Am.,* 81, 28-56.

Fujii Y., K. Satake, S. Sakai, M. Shinohara, and T. Kanazawa (2011). Tsunami source of the 2011 off the Pacific coast of Tohoku Earthquake, *Earth Planets Space* 63, 815–820.

González F. I., R. J. LeVeque, P. Chamberlain, B. Hirai, J. Varkovitzky and D. L. George (2011). Validation of the GeoClaw model, NTHMP MMS Tsunami Inundation Model Validation Workshop.

Graves, R.W. (2005). Broadband simulation for a Mw 6.7 earthquake on the Puente Hills Fault. *SRL* 76, p. 242.

Graves, R.W. and A. Pitarka (2004). Broadband time history simulation using a hybrid approach. Proceedings of the 13th World Conference on Earthquake Engineering, Vancouver, Canada, August 1-6, 2004, Paper No. 1098.

Guatteri, M., Mai, P.M., Beroza, G., and Boatwright, J. (2003). Strong ground motion prediction from stochastic-dynamic source models. *Bull. Seism. Soc. Am.* 93, 301-313.

Hartzell S. (1978). Earthquake aftershocks as Green's functions. *Geophys. Res. Lett.* 5: 1-4.

Hartzell S., and T. Heaton (1983). Inversion of strong ground motion and teleseismic waveform data for the fault rupture history of the 1979 Imperial Valley, California earthquake. *Bull. Seism. Soc. Am.* 1983; 1553-1583.

Hayashi, Y., H. Tsushima, K. Hirata, K. Kimura, and K. Maeda (2011). Tsunami source area of the 2011 off the Pacific coast of Tohoku Earthquake determined from tsunami arrival times at offshore observation stations, Earth Planets Space 63, 809–813.

Hisada, Y. (2001). A theoretical omega-squared model considering spatial variation in slip and rupture velocity. Part 2. Case for a two-dimensional source model. *Bull. Seism. Soc. Am.* 91, 651-666.

Ichinose, G. A., H. K. Thio, P. G. Somerville, T. Sato, and T. Ishii (2003). Rupture model for the 1944 Tonankai earthquake from the inversion of teleseismic and regional seismograms*, J. Geophys. Res.* 108, 10, 2497.

Ichinose, G., H.K. Thio and P. Somerville (2003b). Source characteristics of modern and historical in-slab Cascadia earthquakes applicable to strong motion prediction. USGS Final Report, Award 02HQGR0018.

Irikura K. (1978). Semi-empirical estimation of strong ground motions during large earthquakes. Bull. Disast. Prev. Res. Inst., Kyoto Univ. 33: 63-104.

Ishii, T. T. Sato and P.G. Somerville (2000). Identification of main rupture areas of heterogeneous fault models for strong motion estimates. *J. Struct. Constr. Eng. AIJ* 527, 61-70.

Koketsu, K., H. Miyake, H. Fujiwara, and T. Hashimoto (2008), Progress towards a Japan integrated velocity structure model and long-period ground motion hazard map, paper S10-038 presented at 14th World Conference on Earthquake Engineering, Beijing, China.

Kagawa, T., K. Irikura and P.G. Somerville (2004). Differences in ground motion and fault rupture process between the surface and buried rupture earthquakes. *Earth Planets Space*, 56, 3-14.

Koketsu K., Y. Yokota, N. Nishimura, Y. Yagi, S. Miyazaki, K. Satake, Y. Fujii, H. Miyake, S. Sakai, Y. Yamanaka, T. Okada (2011). A unified source model for the 2011 Tohoku earthquake, *Earth and Planetary Science Letters* 310, 480–487.

Kurahashi S. and K. Irikura (2011). Source model for generating strong ground motions during the 2011 off the Pacific coast of Tohoku Earthquake, *Earth Planets Space* 63, 571–576.

Lay T., H. Kanamori, C. J. Ammon, K. D. Koper, A. R. Hutko, L. Ye, H. Yue, T. M. Rushing (2012). Depth-varying rupture properties of subduction zone megathrust faults. Journal of Geophysical Research: Solid Earth doi:10.1029/2011JB009133.

Mai, M.P. and G. Beroza. (2002). A spatial random field model to characterize complexity in earthquake slip. J. Geophys. Res. 107(B11): doi:10.1029/2001JB000588.

McNeill, A.F., M.G. Bostock, G.C. Rogers, and J.C Shragge (2004). The effect of forearc mantle serpentinization on ground motions from megathrust and intraslab events in the Cascadia subduction zone. *Bull. Seism. Soc. Am.* 94, 147-154.

Mofjeld H.O., V.V. Titov, F.I. González and J.C. Newman (2001). Tsunami scattering provinces in the Pacific Ocean, *Geophys. Res. Lett.*, 28, 335–337.

Murotani, S., Miyake, H., Koketsu, K., Scaling of characterized slip models for plate-boundary earthquakes, Earth, Planets and Space, No. 60, pp. 987-991, 2008.

Ohtsuka, H., P.G. Somerville, and T. Sato (1998). Estimation of broadband strong ground motions considering uncertainty of fault parameters, *J. Struct. Mech. Earthq. Eng.*, JSCE, No.584/I-42, 185-200.

Okada Y. (1985). Surface deformation due to shear and tensile faults in a half space, *Bull. Seismol. Soc. Am.*, 75, 1135–1154.

Okal E. A. and C.E. Synolakis (2004). Source discriminants for near-field tsunamis, *Geophys. J. Int.,* 158, 899–912.

Petersen, M.D., C.H. Cramer, and A.D. Frankel (2002). Simulations of seismic hazard for the Pacific Northwest of the United States from earthquakes associated with the Cascadia subduction zone. *Pure Appl. Geophys.* 159, 2147-2168.

Petersen, M., A. Frankel, A., S. Harmsen, C. Mueller, K. Haller, R. Wheeler, R. Wesson, Y. Zeng, O. Boyd, D. Perkins, N. Luco, E. Field, C. Wills, and K. Rukstales (2008). Documentation for the 2008 updated

of the United States National Seismic Hazard Maps. *U.S. Geological Survey Open File Report* 2008-1128.

Pitarka, A., R. Graves, P.G. Somerville (2002). Investigation of effects of the Seattle Fault Zone structural complexities on ground motions in the Seattle Basin, EOS 83.

Satake K., Y. Fujii, T. Harada, and Y. Namegaya. (2012). Tsunami source model of the 2011 Tohoku earthquake and comparison with the 1896 Sanriku and 869 Jogan earthquakes, *Geophysical Research Abstracts* 14, EGU2012-3542-1, EGU General Assembly, 2012.

Somerville, P.G., M.K. Sen and B.P. Cohee (1991). Simulation of strong ground motions recorded during the 1985 Michoacan, Mexico and Valparaiso, Chile earthquakes, *Bull. Seism. Soc. Am.* 81, 1-27.

Somerville, P.G., K. Irikura, R. Graves, S. Sawada, D. Wald, N. Abrahamson, Y. Iwasaki, T. Kagawa, N. Smith and A. Kowada (1999). Characterizing earthquake slip models for the prediction of strong ground motion. *Seism. Res. Let* 70, 59-80.

Somerville, P.G., T. Sato, T. Ishii, N.F. Collins, K. Dan and H. Fujiwara (2002). Characterizing heterogeneous slip models for large subduction earthquakes for strong ground motion prediction. Proceedings of the Architectural Institute of Japan.

Somerville, P.G., H.K. Thio, G, Ichinose, N. Collins, A. Pitarka, and R.Graves (2003). Earthquake source and ground motion characteristics of the June 23, 2001 Mw 8.4 Arequipa, Peru, earthquake. *Seism. Res. Let.* 74, 223.

Somerville P., R. Graves and N. Collins (2008). Ground motions from large Cascadia subduction earthquakes. Report, U.S. Geological Survey award.

Somerville P., A. Skarlatoudis and W. Li (2013). Ground motions and tsunamis from Mw 9.0 Cascadia subduction earthquakes based on validations using the Mw 8.8 Maule, Chile earthquake of 2010. Final Report, U.S. Geological Survey Award G11AP20041.

Skarlatoudis A.A. and C.B. Papazachos, (2012). Preliminary study of Ground Motions of Tohoku, Japan Earthquake of March 11, 2011, *Seis. Res. Lett.*, 83, 119-129.

Stewart, JP, S Midorikawa, RW Graves, K Khodaverdi, H Miura, Y Bozorgnia, and KW Campbell (2013). Implications of Mw 9.0 Tohoku-oki Japan earthquake for ground motion scaling with source, path, and site parameters, *Earthquake Spectra*, 29 (S1), S1-21.

Wald, D.J. and P.G. Somerville (1995). Variable slip rupture model of the great 1923 Kanto, Japan earthquake: geodetic and body-waveform analysis. *Bull. Seism. Soc. Am.* 85, 159-177.

Wei Y., C. Chamberlin, V.V. Titov, L. Tang and E.N. Bernard (2012). Modeling of the 2011 Japan Tsunami: Lessons for Near-Field Forecast, *Pure and Applied Geophysics,* 170, 1309-1331.

Yokota Y., K. Koketsu, Y. Fujii, K. Satake, S. Sakai, M. Shinohara, and T. Kanazawa (2011). Joint inversion of strong motion, teleseismic, geodetic, and tsunami datasets for the rupture process of the 2011 Tohoku earthquake, *GRL* 38, doi:10.1029/2011GL050098.

Yoshida K., K. Miyakoshi, and K. Irikura (2011). Source process of the 2011 off the Pacific coast of Tohoku Earthquake inferred from waveform inversion with long-period strong-motion records, *Earth Planets Space* **63**, 577–582.

Yue H. and T. Lay, (2011). Inversion of high-rate (1 sps) GPS data for rupture process of the 11 March 2011 Tohoku earthquake (Mw 9.1), *GRL* 38, doi:10.1029/2011GL048700, 2011.

Zhao, J.X., J. Zhang, A. Asano, Y. Ohno, T. Oouchi, T. Takahashi, H. Ogawa, K. Irikura, H.K. Thio, P. Somerville, Y. Fukushima, and Y. Fukushima (2006). Attenuation Relations of Strong Motion in Japan using Site Classification based on Predominant Period. *Bull. Seism. Soc. Am.* 96, 898-913.